The Dissertation Committee for William Andrew Burnett
certifies that this is the approved version of the following dissertation:

Multiazimuth Velocity Analysis Using Velocity-Independent Seismic Imaging

Committee:

Sergey Fomel, Supervisor

Paul Stoffa, Co-Supervisor

Peter Eichhubl

Mrinal Sen

Carlos Torres-Verdín

Multiazimuth Velocity Analysis Using Velocity-Independent Seismic Imaging

by

William Andrew Burnett, B.S., M.S.Geo.Sci.

DISSERTATION

Presented to the Faculty of the Graduate School of

The University of Texas at Austin

in Partial Fulfillment

of the Requirements

for the Degree of

DOCTOR OF PHILOSOPHY

THE UNIVERSITY OF TEXAS AT AUSTIN

May 2011

Dedicated to Ruth Reynolds.

Acknowledgments

If I have seen further it is only by standing on the shoulders of giants.

Isaac Newton, 1676

I might not say I have seen further than anyone, but I have certainly made it further than I could have expected at the end of high school. I remember my senior year at Douglas County High School in Castle Rock, Colorado, when I was certain I would join the military upon graduation. Every student had a councilor who helped each of us figure out what to do after graduation, and fortunately for me, I was assigned to Miss Tricarico. She found it absurd that I hadn't even considered going to college. Upon her suggestion (insistence), I applied to the Colorado School of Mines (CSM). I was accepted and decided to go for a degree in chemical engineering. Upon arrival at CSM, I found out about geophysics, and immediately changed my mind—I haven't given a thought to chemical engineering since.

A similar experience happened at the end of my undergraduate work at CSM. I was walking down the hallway of the Green Center during my senior year, when I was cornered by Alex Kaufman. He suggested (insisted) I join the CWP or some similar graduate program in geophysics, which I took as a huge compliment. Compliments did not come lightly from Dr. Kaufman, so I knew I should take his advice seriously. Thanks to a last-minute suggestion from my undergraduate adviser, Ken Larner, I applied to The University of Texas (UT), and the following year, found myself in Austin beginning a Master's degree under Robert Ferguson.

Once again, graduation came up in 2007, and for the third time, a counselor of sorts asked

me about my plans afterward. This time, it was Sergey Fomel, who became my supervisor for the work in this dissertation. The people I've mentioned so far have had serendipitous influence at key moments in my studies, but they have done so much more, and they are certainly not alone. My only regret in my graduate studies at UT was that at the end of my Master's program, I didn't take the time to really acknowledge everyone who helped me get to where I am. So, I will try to give a little credit here to everyone who has helped or influenced me along the way.

Most recently and obviously, I would like to thank my adviser Sergey Fomel. It's hard for me to believe that I will be his first graduating student, not only because I feel so fortunate, but also because it seems like Sergey has been advising students his whole life. Whenever challenges or opportunities have arisen, Sergey has always provided just the right advice, suggestions, or ideas. He has been not only a great supervisor, but also a true adviser, counselor, guide, colleague, and friend. Not to mention that in his spare time, he finds our group funding, promotes our work, writes most of our software, teaches some of the most rewarding courses, and during my time here alone, has supervised four post-docs and seven other students. Despite all this, I've never had to hesitate to stop by his office with any minutiae or major concerns.

During my work at UT, several other professors have provided guidance as well. I would like to first thank Dr. Paul Stoffa, who as my co-supervisor, has helped me find context for my work both at UT and within the history and the field of geophysics. Next, I would like to thank Dr. Mrinal Sen, who served on both my Master's and Doctorate committees. Mrinal has been a role-model of balance through his excellence in teaching as well as research in both global and exploration geophysics. Taking his course on inverse theory has truly been one of the most useful for my own research as well as being able to understand the work of others. In the Department of Geological Sciences, I would also like to thank Bob Tatham, Steve Grand, Clark Wilson, Kyle

Spikes, Paul Sava, and Philip Guerrero. At the Bureau of Economic Geology, I would like to thank Peter Eichhubl, Steve Laubach, Bob Hardage, Paul Murray, Dallas Dunlap, Reuben Reyes, Douglas McCowan, Diana Sava, Jennifer Logan, Lana Dieterich, and Karl Schleicher. I would like to thank Mead Alison in the Institute for Geophysics and Carlos Torres Verdín and Jon Olson in the Department of Petroleum Engineering. I would also like to add a special thanks to Rob Ferguson, my Master's adviser, who was willing to let a generalist geophysics student like me get a start in seismic imaging.

I have learned just as much from my peers at UT as I have from professors, and they have also provided moral support amongst all of the work. Within our group (now the Texas Consortium for Computational Seismology—TCCS), I would like to give a special thanks to Vladimir Bashkardin and Jules Browaeys who have been two of my best friends and colleagues. I would also like to thank Yang Liu, Hesam Kazemeini, Roman Kazinnik, Xiaolei Song, Siwei Li, Yihua Cai, Parvaneh Karimi, Simin Huang, and Salah Alhadab. Outside of our group, I would also like to thank Russell Young, Long Jin, and Yi Tao at the Institute for Geophysics, and Joost van der Neut at Delft University. I found some of the best moral support in the geology students at UT, among whom I would like to thank Ryan Coppersmith, Ephraim Taylor, Keith Trasko, Andy Dewhurst, Matt Carter, Adam Lambert, Julie Jackson, Eric Kelly, Jaime Levine, Stephanie Moore, Lindsay Szramek, Karin Claeson, Jen Olori, John Hooker, Theresa Diehl, Chad Weisenburger, Peggy Vermeesch, Ethan Perry, Brandon Johnson, Laura DeMott, Bobby Reese, Pete Hargrove, Ethan Lake, and my roommate Daniel Pinkston.

Outside of UT, I would like to thank Alex Calvert, Jim Simmons, Robert Jefferson, and Tariq Alkahlifah. I would like to thank ExxonMobil, GXT/ION Geophysical, Bill Barrett Corporation, and Antero Resources for providing funding or data. I have also been fortunate enough to complete nine internships during my studies, each of which has provided practical experience and opportunities to

work with some of the best geophysicists in industry. I would like to thank each of these companies for providing internship opportunities, and give a special thanks to co-workers and mentors along the way: Gerry Deveaux and Carl LeClaire at WesternGeco; Al Jacobsen at Veritas DGC; Joel Starr, Dale Hargar, Jenny Sambola, Reuben Martinez, and Jason Jonas at PGS; Jan Faulkner, Henrik Roende, and Vincent DuRussel at CGG; Richard Clarke, Ganyuan Xia, Ray Abma, Joe Dellinger, Sneha Chanchani, Patrice Mahob, John Howie, and Pramod Singh at bp; Alex Martinez, Rishi Bansal, Mike Matheney, Andrew Shatilo, Ares Ouzonis, Susan Balon, Tim Farrington, Clarke Trantham, Alison Drain, and Jad Hixon at ExxonMobil; and Betsy Torres, Chuck Coughey, Herb Swan, Phil Anno, Simon Shaw, Anisa Perez, Jack Howell, Stephen Chiu, Samik Sil, Sanjay Sood, and Chunlei Chu at ConocoPhillips.

I would also like to thank a long list of professors and friends from CSM who had tremendous influence on my start in geophysics. Ken Larner, Terry Young, Gary Olhoeft, Mike Batzle, Yaguo Li, Steve Hill, Roel Sneider, John Scales, and Alex Kaufman all helped make geophysics appealing enough for me to make a career out of it. Undergraduate life at Mines has many trials, so the moral support of my peers at Mines was perhaps even more important to my progress than it was at UT. So, I would like to thank John Chakalis, Andy Kass, Brian Grade, Liz LeBarre, Sarah Thompson, Emily Roland, Jason Fletcher, Amy Hinkle, Hunter Yarbrough, Salman Bubshait, Firdaus Fuad, Matt Gardine, Paul Schwering, Kris Davis, Tashi Tshering, Jared Peacock, Brandon Cleveland, Forrest Lundstrum, Mitesh Pradhan, Ivan Vasconcelos, Jyoti Behura, and Rich Krahenbuhl. I want to add a special thanks to my roommates in Golden: Saxon Paiz, John Desens, Tom Huseaus, Stu Adams, and Paul Christopher. Paul introduced me to the world of computer science, and has been a peer role-model and an invaluable source of information and inspiration.

Even before Mines, I was fortunate enough to be surrounded by positive influences. At

Douglas County High School, I would like to thank Matt Wigdahl and Joe Johnson for inspiring my initial attraction to writing and science. I would also like to thank some of my best friends from Castle Rock, including Brandon Baldridge and Kristin Teague—who gathered their extra parts and gave me my first computer at Mines—Debbie and Missy Larsen, Gaven Memmen, Matt and Sarah Hansen, Drew and Aaron Bahr, Ben Bush, Cole Frock, Joseph Buckwalter, Daniel Lewis, Jesse Alsup, and my "extra" families, the Buckwalters, the Lewises, and the Frocks. I especially want to thank Debbie Larsen for being a constant friend and support for as long as I've known her.

Finally, and most importantly, I cannot thank my family enough. I want to thank my Uncle John and my Aunt Barbara who unknowingly inspired an interest in technology in me when I was very young. My father, James Andrew Burnett, is the source of my earliest interests in mathematics and science, so I owe him everything. Making the decision to pursue a doctorate was difficult for me, but my father was so encouraging that he convinced me to go for it. My grandmother Ruth Reynolds passed away during the final year of this work, but I know she would be proud of it. She used to read me, my sister, and my cousins stories before bed time—and although this tome may not be as interesting as the adventures of Raggedy Anne and Andy, I have dedicated it to her. And last, the most important people in making everything I do possible are still my mother Susan and my sister Heather. I cannot say how much I appreciate the sacrifices of time, work, and general stress that my "extended stay" in school has required of them. I want to thank them for constant encouragement and for trusting in my decision to stay in Austin for a Ph.D. All I can say is that I will never forget it, and that I will always be looking for ways to return their help.

The quote in the epigraph was written in a letter to Robert Hooke. Newton and Hooke were to some extent rivals in their time, but their separate works would later come together in ways even they could never imagine. Today in geophysics, we use their combined works in the now

fundamental derivation of the wave equation, without which, this dissertation would not exist. Many of my family members, professors, friends, colleagues, and mentors, also could never have guessed, but their independent contributions would eventually conspire to add a small part to the field of geophysics. Without them, this dissertation would not exist, and I am very grateful for all of their giant shoulders on which I stand.

WILLIAM ANDREW BURNETT

The University of Texas at Austin

May 2011

Multiazimuth Velocity Analysis Using Velocity-Independent Seismic Imaging

Publication No. _____

William Andrew Burnett, Ph.D.

The University of Texas at Austin, 2011

Supervisors: Sergey Fomel
Paul Stoffa

Multiazimuth seismic data contains information about how the Earth's seismic response changes with azimuthal direction. Directional-dependence of the seismic response can be caused by anisotropy or heterogeneity, associated with subsurface features such as fractures, stresses, or structure. Characterizing azimuthal variations is done through velocity analysis, which provides a link between an acquired data set and its image, as well as between the image and subsurface geology. At the stage which conventional velocity analysis is applied, it is difficult to distinguish the geologic cause of observed azimuthal velocity variations. The inability to distinguish the similar effects of anisotropy and heterogeneity leads to positioning errors in the final image and velocity estimates. Regardless of the cause, azimuthally variable velocities require at least three parameters to characterize, as opposed to the conventional single-parameter isotropic velocity. The semblance scan is the conventional tool for seismic velocity analysis, but it was designed for the isotropic case. For multiple parameters, the semblance scan becomes computationally impractical. In order to help address the

issues of geologic ambiguity and computational efficiency, I develop three methods for multiazimuth seismic velocity analysis based on "velocity-independent" imaging techniques. I call this approach, velocity analysis by velocity-independent imaging, where I reverse the conventional order of velocity estimation followed by image estimation. All three methods measure time-domain effective-velocity parameters. The first method, 3D azimuthally anisotropic velocity-independent NMO, replaces the explicit measurement of velocity with local slope detection. The second method, time-warping, uses local slope information to predict traveltime surfaces without any moveout assumption beforehand, and then fit them with a multiparameter velocity model. The third method, azimuthal velocity continuation, uses diffraction image focusing as a velocity analysis criterion, thereby performing imaging and velocity analysis simultaneously. The first two methods are superior to the semblance scan in terms of computational efficiency and their ability to handle multi-parameter models. The third method is similar to a single multi-parameter semblance scan in computational cost, but it helps handle the ambiguity between structural heterogeneity and anisotropy, which leads to better positioned images and velocity estimates.

Table of Contents

List of Tables

List of Figures

Chapter 1

Introduction

Seismic Imaging

Seismic imaging plays an important role in geosciences, particularly in problems of characterizing the earth's subsurface. The general seismic experiment consists of a seismic source (natural or artificial) and seismic receivers (geophones, hydrophones, seismometers, etc.) on or within the earth. Seismic waves propagate from the source, through the earth, to the receivers, and the objective is to use wave physics to explain the observed waveforms (Aki and Richards, 2009; Stein and Wysession, 2003). In exploration seismology, which is the main context of this work, the source is artificial with known timing, and both the source and receivers have known positions (Yilmaz, 2001). With this information controlled and known, explaining observed waveforms is a matter of characterizing the subsurface with parameters that affect wave propagation. Under the commonly assumed linear elastic model, propagation is only affected by the distribution of 21 independent elastic parameters (scaled by density) within the subsurface (Green, 1839).

The primary product of seismic imaging is an image of the subsurface geologic structure. Waveforms have both amplitude and traveltime information, but for structural imaging, accounting for the observed traveltimes is far more important. So to further simplify the problem, wave propagation can be mathematically separated into two equations: one describing amplitudes (transport equation) and one describing traveltimes (eikonal equation) (Červený, 2001). Despite (or perhaps because of) their high sensitivity to the elastic parameters, amplitudes are often neglected aside

from geologically simple cases with nearly regular acquisition. Recorded amplitudes are related to particle displacements, which in turn relate to local strains caused by an incident wavefield. Under linear elastic theory, wavefield stresses determine strains via the constitutive relation (Hooke, 1678), and since both stresses and strains are directional, amplitudes should be treated as vectors. Properly treating amplitudes using both magnitude and polarization leads to the Christoffel equation, which reveals the existence of wave modes, such as P-waves and fast and slow S-waves (Stokes, 1845; Christoffel, 1877). Still, in the cases where they are used in practice, amplitudes are commonly approximated as having magnitude alone (pressure) which simplifies the problem further to the single-mode acoustic approximation.

However, this "simplified" problem, is often still not simple enough. Because the distribution of elastic parameters in the earth is highly heterogeneous and unknown, modeling and predicting traveltimes alone is difficult. Hence, in addition to the acoustic approximation, fully elastic wave propagation is simplified by assuming increasing orders of anisotropic symmetries. In order of increasing symmetry, fewer and fewer parameters are needed: triclinic (21 parameters), monoclinic (13 parameters), orthorhombic (9 parameters), transverse isotropic (5 parameters), and isotropic (2 parameters) (Tsvankin, 2005). For the acoustic isotropic case, wave propagation can be described by one parameter: the seismic velocity. This single-parameter approximation of a vastly more complicated process is the conventional choice in industry to approximate how seismic waves propagate through the earth's subsurface, and has been so since the first seismic exploration surveys of the early 1900's.

In the context of inverse theory, the seismic velocity estimation problem can be generally written as,

$$\mathbf{d} = \mathbf{G}[\mathbf{m}]. \tag{1.1}$$

By using the eikonal equation and geometrical approximations of wave physics ($\mathbf{G}$) to explain observed waveforms ($\mathbf{d}$), it is possible to estimate the distribution of elastic parameters ($\mathbf{m}$) in the subsurface as an inverse problem:

$$\mathbf{m} = \mathbf{G}^{-1}[\mathbf{d}]. \tag{1.2}$$

Because the fully elastic parameter distribution of the subsurface is often reduced to a single-parameter velocity distribution, the model vector in equation 1.2 is often just referred to as the estimated velocity. The additional parameters needed for anisotropic models describe how velocity changes with direction, so I will continue to refer to these parameters as the velocity estimate throughout this dissertation, even in multi-parameter cases.

Velocity estimation is the most important step in seismic imaging, as an accurate velocity estimate yields better positioning of reflection events and better focusing of diffraction events in the final image (Claerbout, 1999). Estimating the subsurface velocity from seismic data is conventionally done by relating observed traveltime event geometries to assumed moveout models. In exploration seismology, special attention is given to the moveout geometry of reflections. The relation between reflection traveltime event geometries and velocities was originally documented by Rieber (1936) and Slotnick (1936) in the first volume of the journal *Geophysics*. To this day, most practical velocity analysis methods depend on similar velocity-geometry relations. The term, "moveout", refers to following a particular wave event as source-receiver distance increases. When the arrival time, $t(\mathbf{x})$, of a pure-mode reflection event is plotted as a function of source-receiver distance, $d = |\mathbf{x}|$, its

geometry is usually assumed to be hyperbolic, and is said to have hyperbolic, or normal, moveout (commonly abbreviated as NMO). In this notation, $\mathbf{x}$ is the source-receiver offset vector,

$$\mathbf{x} = \begin{pmatrix} x_1 \\ x_2 \end{pmatrix}, \tag{1.3}$$

where x_1 and x_2 are the components of full source-receiver offset in the orthogonal surface survey coordinates. In practice, seismic data are regrouped into synthetic aperture common midpoint (CMP) gathers, in which traveltime events associated with flat reflectors often do have nearly hyperbolic geometries. The conventional velocity analysis procedure (Yilmaz, 2001) is to simply search for the best-fitting hyperbola to each reflection event, following the so-called "NMO equation",

$$t\left(\mathbf{x}, W_0\right) = \sqrt{t_0^2 + \mathbf{x}^{\mathrm{T}} W_0 \mathbf{x}}, \tag{1.4}$$

where superscript $^{\mathrm{T}}$ denotes transpose, and the scalar $W_0 = 1/v^2$, with v as the isotropic seismic velocity. Equation 1.4 describes a 3D surface that is circular-hyperbolic (hyperbolic in cross-section, and circular in map view). One can also view equation 1.4 as a truncated (two-term) Taylor series expansion for t^2.

Finally, once the velocity is estimated, the structural image is created by transforming the observed seismic data from its recorded positions to its image positions. This image transformation is called seismic migration, and has many theoretical and practical variants. Migration can be broken into a sequence of steps or it can be done all at once. When it is done all at once, migration is a transformation operator, $\mathbf{F}_{mig}$, that uses the velocity model to transform recorded data into an image. Historically, breaking migration into a sequence of steps has had intuitive and practical

benefits. The most common decomposition is to approximate migration as a series of three major steps,

$$\mathbf{F}_{mig} \approx \mathbf{F}_{NMO} + \mathbf{F}_{DMO} + \mathbf{F}_{ZOM} \tag{1.5}$$

(Forel and Gardner, 1988; Fowler, 1997). The first two steps are traveltime corrections which transform data to as if they were all acquired at zero-offset (source and receiver positions coincident). These two steps are the NMO correction F_{NMO}, which removes hyperbolic moveout from reflection events (accurate for flat reflectors), and the dip-moveout (DMO) correction F_{DMO}, which accounts for traveltime variations from dipping reflectors. The third step is zero-offset migration F_{ZOM}, which transforms the moveout-corrected data to the image by collapsing diffraction events to image points. Since data are collected at many locations on the earth's surface, most regions of the subsurface are illuminated more than once. At some point during imaging, an additional step called "stacking" is used to combine data illuminating the same image location. When migration is decomposed into the three steps in expression 1.5, stacking is usually performed after NMO and DMO, but before zero-offset migration. Hence, the decomposed approach is usually referred to as "post-stack" imaging, simply because of the order of steps. The alternative is therefore referred to as "pre-stack" imaging, which postpones summing the data until they have been completely transformed (Yilmaz, 2001).

Regardless of the variant, all conventional approaches to imaging estimate the velocity model first, and then perform migration. Even for pre-stack imaging, the velocity is first estimated by isolating the steps of migration most sensitive to velocity. As discussed above, the NMO correction is the step most commonly used, because of its sensitivity to velocities that influence events from naturally common flat geologic reflectors. The basis of reflection velocity estimation is to analyze

traveltime moveout with offset, so pre-stack migration algorithms which preserve offset information through the entire process can also be used for velocity analysis. Zero-offset migration is also sensitive to velocity, but it is not as commonly used for velocity analysis, because under the conventional imaging flow, NMO must be done first anyway. Hence, the most critical step of time-domain seismic imaging—velocity analysis—is almost always first performed by NMO-based reflection traveltime moveout analysis.

NMO is a velocity analysis tool for the pre-stack migration case, and both an imaging step and a velocity analysis tool for post-stack migration flows. As an imaging step, NMO performance is judged on how well events become flattened on CMP gathers, as the result is summed over offset (stacked). If a reflection event is flat before stacking, it will constructively interfere while being stacked into the zero-offset image, whereas events with residual moveout will produce a degraded stack. Since NMO is sensitive to the velocity used to perform it, event flatness is therefore useful in choosing the optimal velocity model.

When viewing event flatness as a velocity analysis criterion, a distinction must be made between the physically meaningful near-offset hyperbolic velocity and the best "flattening" velocity. For near-offset data and a vertically-heterogeneous medium, the hyperbolic velocity, v from equation 1.4, is related to a time-weighted average velocity between the earth's surface and the reflection, referred to as the root-mean-square (RMS) velocity (Yilmaz, 2001). The RMS velocity can be used to solve for geologically meaningful interval velocities using the Dix inversion method (Dix, 1955). However, in field-data CMP gathers, reflections often deviate from hyperbolic moveout as offsets increase. As farther offsets are included, fitting a nonhyperbolic event with a hyperbolic surface will change the estimated velocity. It then becomes advantageous to view the traveltime (squared) surface as a polynomial function of offset, which is approximately second-order (hyperbolic) at near offsets,

and influenced by quartic and higher-order terms at farther offsets (Taner and Koehler, 1969). In the near offsets, the second-order "NMO velocity" (v_{NMO}) is accurate, and can be physically related to the RMS velocity, which in turn, physically relates to interval velocities. Among all single-parameter models, applying the best-fit hyperbolic moveout correction over all offsets will by definition always produce the flattest event and the best stack, but the velocity parameter will lose physical meaning as offsets increase. For this reason, the best flattening hyperbolic velocity v is often called the "stacking velocity", as it is usually close to, but slightly higher than, the near-offset v_{NMO} for common geologic scenarios (Dobrin and Savit, 1988).

Converting stacking velocities to interval velocities by Dix inversion is the conventional approach to obtaining geologic parameters, but this can be physically inaccurate for far-offset data and nonhyperbolic events. A better approach as farther offsets are included, is to measure the higher-order moveout terms in addition to the hyperbolic term (Tsvankin and Al-Dajani, 1998; Tsvankin, 2005). One common parametrization of nonhyperbolic moveout is from Alkhalifah and Tsvankin (1994), who proposed a two-parameter velocity model (v_{NMO}, η) to effectively characterize both the near- and far-offset moveout separately. Alternative parametrizations include the shifted hyperbola of Castle (1988), the moveout-acceleration approximation of Taner et al. (2007) and the generalized approximation of Fomel and Stovas (2010). Nonhyperbolic moveout is generally a result of heterogeneity or a common type of seismic anisotropy (vertical-transverse isotropy–VTI) associated with flat, relatively thin geologic layering (Fomel and Grechka, 1996)*. Under the VTI anisotropy assumption, seismic velocity varies with the vertical propagation direction, but not with azimuth. A major improvement in velocity analysis would be to measure nonhyperbolic and azimuthally-variable moveout simultaneously, leading to an effective orthorhombic velocity model

*Stanford Exploration Project references can be found online at `http://sepwww.stanford.edu/oldreports`

(Vasconcelos and Tsvankin, 2006). However, as I show in the next section, the case of azimuthal anisotropy alone remains challenging for practical parameter estimation.

Azimuthal Anisotropy

Although anisotropic wave propagation has been well understood for much longer, attempts to use lower symmetries of anisotropy have only made practical progress since the 1980's, with the key works of Muir and Dellinger (1985), Thomsen (1986), and later Alkhalifah and Tsvankin (1994). The paradigm shift from works like these was to begin deriving simplified parametrizations for anisotropic wave propagation, rather than attempt to directly measure the elastic parameters themselves. These simplified parametrizations are theoretically not as accurate as the full 21-parameter elastic description, but they are far easier to measure from seismic observations, and perhaps more importantly, their use has definitively improved seismic images. Whether through deriving ever simpler anisotropy parametrizations, improving survey designs, or advancing computational algorithms, increasing the ability to actually measure anisotropic velocity models has continued to be a fruitful research direction within seismic imaging (Tsvankin, 2005).

Many of the most useful advancements in seismic imaging have come from trying to handle difficult geological situations. For example, the anisotropy approximations introduced by Thomsen (1986) and Alkhalifah and Tsvankin (1994) took the effects of common geologic layering on seismic wave propagation into special consideration, which has led to dramatic improvements in imaging deep reservoirs, where these effects are magnified. Often in addition to being deeper, modern hydrocarbon exploration targets are in increasingly subtle and complicated geology—instead of broad structural traps containing reservoirs where porosity contains hydrocarbons, modern targets are often stratigraphic traps, with fractures or micro-porosity controlling fluid flow. Fracturing is among the

many common geological occurrences that can lead to seismic azimuthal anisotropy, in which case the seismic velocity is, or appears to be, azimuthally-dependent (Grechka and Tsvankin, 1998). Failure to account for azimuthal velocity variations in the seismic velocity often leads to improper time-to-depth conversion, inaccurate amplitude analysis, and overall poorer image results (Williams and Jenner, 2002). The fastest and slowest directions of observed azimuthal anisotropy are often related to the preferred orientation of vertical fractures (Crampin, 1984), but may also correspond to other geologically meaningful factors, such as the strike and dip directions of a reflector (Levin, 1985), or the regional stress directions (Sicking et al., 2007b). Therefore, measuring azimuthal anisotropy and identifying its cause not only improves the seismic image, but also provides valuable geologic information. Despite its relatively high costs, multiazimuth acquisition—both onshore and offshore—has gained popularity recently, partially because of its ability to capture this valuable azimuthal information (Etgen and Regone, 1998; Manning et al., 2007).

In the case of azimuthal variations alone, at least three parameters are needed at each subsurface location to parametrize the velocity model. The NMO equation can be derived to allow elliptical variation of velocity with azimuth using a truncated 2D Taylor series expansion (Grechka and Tsvankin, 1998). As a result, the multiazimuth NMO equation can be written as:

$$t\left(\mathbf{x}, \mathbf{W}\right) = \sqrt{t_0^2 + \mathbf{x}^T \mathbf{W} \mathbf{x}}, \tag{1.6}$$

where, $\mathbf{W}$ is the slowness matrix,

$$\mathbf{W} = \begin{pmatrix} W_{11} & W_{12} \\ W_{12} & W_{22} \end{pmatrix}. \tag{1.7}$$

The three independent parameters of **W** have units of slowness-squared. In most common geologic situations, the eigenvalues of **W** are positive (Tsvankin, 2005), and equation 1.6 describes an elliptical-hyperbolic traveltime surface in 3D—hyperbolic in cross-section view and elliptical in map-view—so is often referred to as the equation of the "NMO ellipse". W_{11} and W_{22} are the squared moveout slownesses along the respective survey coordinates, x_1 and x_2. The third parameter, W_{12}, arises from observing the ellipse in the x_1-x_2 survey coordinates, which are generally rotated relative to its major and minor axes (Figure 1.1).

If the ellipse happens to be aligned with the survey coordinates, $W_{12} = 0$. The semi-major and semi-minor axes of the ellipse correspond to the slowest and fastest moveout velocities, respectively, as well as their orientations. Physically, these directions indicate the symmetry axes of the effective anisotropic medium. Therefore, finding the rotation angle which properly diagonalizes **W** allows one to predict the orientation of the symmetry axes. This amounts to an eigenvalue problem, where the fast and slow velocities can be found as the eigenvalues and eigenvectors of **W**. The eigenvalues, W_{fast} and W_{slow}, of the slowness matrix can be found following Grechka and Tsvankin (1998),

$$W_{slow,fast} = \frac{1}{2}\left[W_{11} + W_{22} \pm \sqrt{(W_{11} - W_{22})^2 + 4W_{12}^2}\right]. \tag{1.8}$$

Since the eigenvalues have units of slowness squared, the smaller eigenvalue is $W_{fast} = 1/v_{fast}^2$. One can solve for the angle β between the acquisition coordinates and the symmetry axes by using geometric arguments and well-known relations between the formulas for a rotated ellipse and its unrotated equivalent as,

$$\beta = \frac{1}{2}\tan^{-1}\left(\frac{2W_{12}}{W_{11}-W_{22}}\right) - c, \tag{1.9}$$

where $c = \pi/2$ when $W_{11} < W_{22}$ and $c = 0$ when $W_{11} \geq W_{22}$ (Weisstein, 2009) . If W_{11} is equal to W_{22}, then the arc-tangent argument goes to infinity, corresponding to $\beta = \pi/4$. In equation (1.9), β is the angle from a survey axis measured counter-clockwise[†] toward the slow symmetry axis. Equation (1.9) is equivalent to that found by Grechka and Tsvankin (1998), who define the same angle as,

$$\beta = \tan^{-1}\left[\frac{W_{22}-W_{11}+\sqrt{(W_{22}-W_{11})^2+4W_{12}^2}}{2W_{12}}\right]. \tag{1.10}$$

Finally, the eigenvalues can be used together with β to solve for the NMO slowness $S = 1/v$ as a function of source-receiver azimuth (counter-clockwise from x_1) θ:

$$S^2(\theta) = W_{slow}\cos^2(\theta-\beta) + W_{fast}\sin^2(\theta-\beta). \tag{1.11}$$

Equations 1.8-1.11 allow one to convert the mathematically convenient parameters of **W** to more intuitive parameters, such as the fastest and slowest propagation velocities (v_{fast},v_{slow}), the fast azimuth ($\alpha = \beta + \pi/2$), and the percent anisotropy ($\phi = 100 \times (1 - v_{slow}/v_{fast})$). Alternatively, **W** can be converted into other parametrizations such as the Thomsen (1986) parameters, or even into estimates of the physical elastic parameters following Grechka and Tsvankin (1998). For example, Grechka and Tsvankin (1998) show that once the effective parameters **W** have been converted to

[†]The rotation angle β is counter-clockwise from the x_1 axis to the x_1' axis, assuming the mapview layout shown in Figure 1.1. If one, and only one, of either the x_1 or x_2 axes reverses direction, β represents a clockwise rotation from x_1 to x_1'.

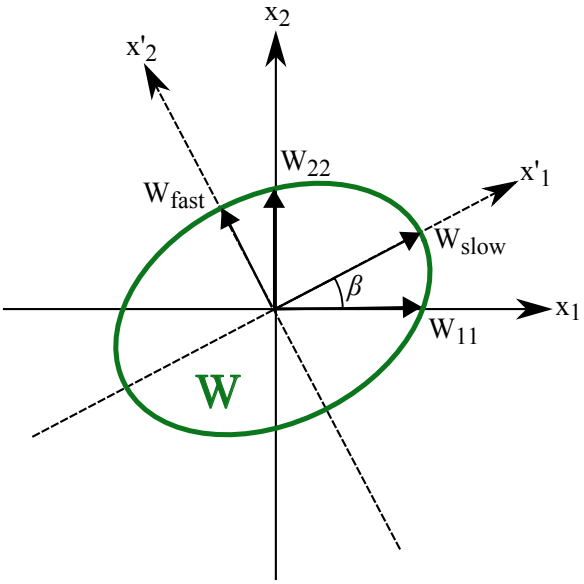

Figure 1.1: Sketch of slowness ellipse, **W**. The acquisition coordinates, x_1-x_2, are generally not aligned with the symmetry axes, x_1'-x_2'. The rotation angle β is measured counter-clockwise from x_1 to x_1' (The value of β shown in the figure is positive). chapter-introduction/. W-ellipse

slowness as a function of azimuth by equation 1.11, they can be expressed in terms of horizontal transverse isotropy parameters as,

$$S^2(\theta) = \frac{1}{V_{P0}^2} \frac{1 + 2\delta^{(v)} \sin^2(\theta)}{1 + 2\delta^{(v)}}, \tag{1.12}$$

where $\delta^{(v)}$ is the Thomsen-style parameter introduced by Tsvankin (1997), and V_{P0} is the vertical P-wave velocity. Like the final seismic image, the more intuitive parameters are themselves a valuable product of seismic imaging and analysis because they are easily understood across disciplines. After interpretation in the context of geologic and engineering data, they can provide valuable information about subsurface structures, fractures, or stresses. However, while a single velocity parameter is easily estimated from seismic data, measuring a three-parameter velocity model is both computa-

tionally and operationally unreasonable using the conventional approach and modern resources. A short review of conventional seismic velocity analysis methods reveals the basis for this claim.

The Semblance Scan

Conventional velocity analysis is assisted computationally through a variety of tools that help the processing geophysicist select the best velocity for each reflection event. The semblance scan (Taner and Koehler, 1969; Neidell and Taner, 1971) is a manual grid-search method for finding velocity parameters, and is the most common tool. Semblance scans have maintained their popularity for decades because they are intuitive, interactive, and robust. Even in the presence of strong noise, semblance scans can detect hyperbolic events and indicate their velocities. The output of a semblance scan is a 2D panel which can be interactively displayed on a computer screen. This allows geophysicists to interpret the results and include physical insight (or bias) into the final chosen velocity model.

The semblance panel is a time versus velocity plot displaying values of semblance, $\sigma(t_0, v)$, for a range of test t_0 and v. For the isotropic case, the semblance for each test t_0-v point is computed using the formula,

$$\sigma(t_0, v) = \frac{\left[\sum_{i=1}^{N} d_i(t_0, W_0)\right]^2}{\frac{1}{N}\sum_{i=1}^{N} d_i^2(t_0, W_0)}, \tag{1.13}$$

where $d_i(t_0, W_0)$ are data from all N-points in an input CMP gather which satisfy equation (1.4) parametrized by t_0 and $W_0 = 1/v^2$. The highest semblance values indicate likely velocities, as a high semblance value means that the data closely resemble a hyperbola with the t_0-coordinate as its intercept, and the v-coordinate as its velocity. The processing geophysicist then selects maxima on

the semblance panel from $t_0 = 0$ down to the bottom of the gather. The result is typically a single velocity profile, $v(t_0)$, which characterizes the moveout velocity for the given CMP location.

Commonly, semblance maxima are picked by hand, which involves careful manual inspection of the seismic data along with the semblance panels, and because of the typically large size of seismic data sets, velocities can only be picked at relatively sparse locations. This manual process is time-consuming and, to some extent, subjective. The manual part of velocity analysis may take weeks or months to characterize a modern 3D seismic data set, even when velocities are picked on just a small subset of the CMP gathers, and for the simple isotropic case. However, semblance-based velocity analysis can be semi-automated by instead allowing a computer program to select the most likely velocities. Besides the maximum values on the semblance map, additional constraints can be included to make the automatic selection more realistic (Fomel, 2009). Automating the semblance scan and velocity picking has made dense isotropic velocity model estimation possible, even for large 3D data sets (Siliqi et al., 2003). Assuming a perfectly automated semblance-based velocity analysis, we can ignore the time it takes for manual picking, and express the computational complexity of a single parameter scan as $\mathcal{O}(N_{\mathbf{x}} \times N_{t_0} \times N_v)$. This cost estimate comes from observing that a semblance scan must sum over $N_{\mathbf{x}}$ data points to compute each of $N_{t_0} \times N_v$ values. Overall, we can see that the semblance scan cost is proportional to the size of the data set multiplied by the number of tested velocity models. For the isotropic case, only one velocity parameter must be scanned, and typically the number of test velocities (N_v) is on the order of 10^2. This makes the automated semblance scan reasonably efficient, for the single-parameter isotropic case.

In the 3D anisotropic case, the semblance between reflection events and a range of hyperboloid or hyperboloid-like surfaces can yield velocity models for anisotropic and heterogeneous media (Dewangen and Tsvankin, 2006; Wang and Tsvankin, 2008). However, semblance scans become com-

putationally expensive, as the scan must be performed over several parameters. The computational complexity becomes $\mathcal{O}(N_{\mathbf{x}} \times N_{t_0} \times N_v^{N_p})$, where N_v now represents the number of test parameter increments, and N_p is the number of velocity model parameters. This complexity assumes that N_v is roughly the same for each velocity model parameter, around 10^2. In the isotropic case, there is only one parameter, so $N_p = 1$, and the complexity reduces to the previous cost expression. However, in the multi-parameter case, the total number of tested velocity models increases dramatically with the number of model parameters. In the azimuthally anisotropic case, for example, $N_p = 3$, so for a reasonable $N_v = 100$, the overall cost increases by four orders of magnitude. Assuming one has the computational power to complete a multi-parameter semblance scan for a full seismic data set, the memory required to store the semblance volumes would be unreasonable. Unlike the isotropic case, where the computed semblance values take up $N_{t_0} \times N_v$ space in memory (roughly the same size as the input data set), the multi-parameter semblance volumes would occupy $N_{t_0} \times N_v^{N_p}$ space in memory—roughly 10^4 times the size of the input data set for a three-parameter model. With a typical modern 3D seismic data set being on the order of a terabyte in size, this is clearly not yet feasible. Furthermore, assuming sufficient computational resources to both compute and store a multi-parameter scan, it would still be challenging to interpret or pick the optimal velocity model as a function of time. Instead of selecting maxima from a 2D panel, the user, or automating program, would have to select a smooth, geologically reasonable profile out of a four-dimensional hypercube, at every CMP analysis location.

There are shortcuts for multi-parameter semblance scans which can make the problem tractable. For example, using external information, such as borehole measurements, can help constrain the range of the scan. Or in the azimuthally anisotropic case, performing a 2D azimuthally-sectored scan in three or more different directions can provide an estimate of anisotropy. Shortcuts

like these are the conventional approach to multi-parameter measurements in industry, but they do not guarantee the correct velocity model will be found. Al-Dajani and Alkhalifah (2000) and Lynn (2007) have suggested that using more or all available azimuths leads to more accurate parameter estimates than sectored analysis.

Velocity-independent Imaging

From the discussion above, it is clear that even using oversimplified physical assumptions, velocity analysis is an important yet time-consuming step in seismic imaging. It is also clear that the connection between the measurable seismic velocities and the physical properties that we care about, can be misleading in many common geologic cases. Recognizing these challenges along with the need for improved images and subsurface information, geophysicists have generally taken two different approaches to advancing the field of seismic imaging: a physics-driven approach and a data-driven approach. An example of a physics-driven method, full-waveform inversion, has recently become popular in research, because it is theoretically almost ideal for treating seismic data. Full-waveform inversion could potentially yield valuable physical properties of the subsurface as well as a nearly ideal image. The strategy behind full-waveform inversion is to include as many physical aspects of wave propagation as possible to directly predict recorded data. There are many issues to handle, however, before full-waveform inversion by strict definition becomes practical. Aside from computational cost, many of these issues are fundamental and well-known to exploration seismology, such as incomplete source and receiver distributions and limited bandwidth of recorded data.

Full-waveform inversion represents the goal of a physics-driven approach to seismic imaging, yet the realities of field acquisition severely limit its application. These realities have historically forced the more pragmatic data-driven approach to seismic imaging (described in the previous sec-

tions), where assumptions about wave propagation and subsurface properties are relaxed to the point that the measured effective parameters are often physically ambiguous, yet they can be used produce an interpretable image. Most conventional imaging flows take the data-driven approach, where effective imaging parameters are measured and then subsequently related to useful physical properties. If the image is the main objective of exploration seismology (historically the case), data-driven imaging provides the interesting possibility of completely ignoring physical properties such as velocity, and only producing an image. Since the amount of both computational and manual work required by velocity analysis is so high, geophysicists have explored this possibility by devising several so-called "velocity-independent" imaging methods which attempt to bypass velocity analysis altogether.

Imaging techniques taking the velocity-independent name—most arising over the past thirty years or so—have many different underlying strategies. Regardless of the strategy, their most obvious potential benefit is the possibility of completely automated imaging, with no need for costly velocity estimation. In each strategy however, the term "velocity-independent" is a bit misleading, because in each case, the velocity model is still implicitly estimated. This leads to a less obvious (and almost ironic) potential benefit of velocity-independent methods: automated velocity analysis. I will examine several velocity-independent imaging strategies and their applications to velocity analysis.

The velocity-independent imaging techniques in my research embrace the pragmatic data-driven approach to seismic data analysis, which makes it possible to apply in practice. The motivation for this research, however, is aligned with the physics-driven ideal, in that I recognize the measurement of subsurface physical properties as a worthy goal. In fact, physics-driven methods often need initial estimates of the subsurface properties just to start, and data-driven imaging may be the best route to providing them. With this long-term goal in mind, I will focus on data-driven

velocity-independent methods which measure effective velocity parameters—not physical interval velocities. I will briefly mention potential options for converting these effective parameters into interval estimates along the way (such as the generalized Dix inversion above), but my main focus is on measurement.

Amongst the variety of velocity-independent strategies, I first focus on those using directional attributes. The fundamental principle behind directional attribute methods is explained by Rieber (1936), namely, the connection between seismic event slopes and seismic velocities. This approach was developed further in the Soviet Union through the Controlled Directional Reception (CDR) method (Riabinkin, 1957; Hermont, 1979; Sword, 1981). Historically, imaging methods exploiting seismic event slopes have relied on plane-wave decomposition (Ottolini, 1983a). Plane-wave decomposition assumes an entire range of slopes is present in the data, each of which is assigned a global amplitude based on a sum of contributions from throughout the input data. Plane-wave decomposition is often performed using the f-k transform (2D or 3D Fourier transform) (Yilmaz, 2001) or the τ-p transform (Stoffa et al., 1981). The plane-wave domain has several processing advantages over the time-distance (t-x) domain. Many of these advantages are based on the link between the plane-wave dip and the ray parameter (Stoffa et al., 1981), while others take advantage of convenient traveltime curve geometries or periodicities in the plane-wave domain (Liu, 1999).

A modern complement to plane-wave decomposition is available through *local* slope measurement tools such as plane-wave destruction (PWD) filters (Claerbout, 1992; Fomel, 2002). In this approach, each data point is assigned a dominant slope based only on near-by data. Local slopes are stored as volumetric attributes of the data set (Fomel, 2007b), allowing spatial, temporal, and directional flexibility in applied processes. This makes directional attribute velocity-independent imaging well suited for multiazimuth data sets. When viewed as components of 3D surface gradients, local

slopes provide a natural, directionally flexible 3D formalism for seismic imaging. Conventional velocity analysis for large multiazimuth 3D data sets does not truly take advantage of the rich azimuthal information because it is simply too time-consuming to measure directionally-dependent properties manually. By exploiting the benefits of automated velocity extraction from directional attributes, this conventional limitation may be avoided.

Aside from azimuthal flexibility, local directional attribute techniques also offer other powerful benefits (Cooke et al., 2009). Techniques involving local slopes often have analogous techniques in the well-understood τ-p and f-k processing domains. Local slopes can even be measured within the τ-p domain, where additional benefits for velocity analysis are found (Casasanta and Fomel, 2010). In fact, local slopes can be measured for a variety of unconventional velocity analysis and imaging approaches, including the "multifocusing" method (Berkovitch et al., 2008) and the common-reflection surface (CRS) method (Gelchinsky, 1988). Another benefit is the possibility of attribute-based localized processing (Sun et al., 2000). In this case, local slopes and curvatures can be used to effectively interpolate between a sparse subset of image points (Yilmaz and Taner, 1994) through the use of image basis functions such as seislets (Fomel and Liu, 2010). Rather than process each individual data point, "packets" of information can be processed to increase computational efficiency (Sherwood et al., 2008; Burnett and Fomel, 2008b).

Combining the benefits of local slope-based velocity-independent imaging may lead to significant advances in seismic imaging efficiency and quality. In this dissertation, I focus mainly on the benefit of azimuthal flexibility for multiazimuth velocity analysis in the t-x domain. I also refer to related extensions of these methods in other domains, including related work on localized, τ-p, and multifocusing imaging strategies using directional attributes.

The second type of velocity-independent method I examine is focusing-based. Instead of

measuring the velocity beforehand, this approach performs imaging with a whole range of possible velocities, and then measures which regions of each test image are best-focused (Fowler, 1984). I extend this idea to 3D using the framework of velocity continuation (Fomel, 1994, 2003b). This leads to an application of another velocity-independent imaging strategy, based on path-integral imaging (Landa et al., 2006), where the images corresponding to all velocities are summed to estimate the correct image.

Problem Statement and Outline

The value of azimuthal information from seismic data has justified the development and deployment of novel multiazimuth acquisition methods, yet this information remains difficult to extract because it must be described by a multi-parameter velocity model. I claim that the semblance scan is not suitable for multi-parameter seismic velocity analysis. Even in the still geologically oversimplified assumption of azimuthal anisotropy alone, the velocity model requires at least three parameters, which makes the semblance scan impractical. As alternatives to the semblance scan, I propose three methods for the measurement of azimuthally anisotropic velocity parameters from seismic data. These methods all use velocity-independent imaging techniques,which I have adapted to return implicit effective-medium-based velocities. Unlike the conventional imaging flow, which measures velocity first, and then performs imaging, the philosophy shared by these methods is to image first, and then determine the velocity that connects the recorded data to the image.

All of the proposed methods also use volumetric 3D local slope measurements, but each for a different purpose. The first method, azimuthally-anisotropic velocity-independent NMO, uses local slope measurement as a direct replacement for velocity estimation. Since local slopes capture the 3D geometry of reflection traveltime surfaces, they also contain complete velocity information.

The second method, time-warping, uses local slopes to predict reflection traveltime surfaces themselves. Again, knowledge of the surface geometry yields complete velocity information, even in the azimuthally anisotropic case. The third method, azimuthal velocity continuation, uses local slopes of stacked seismic data to separate diffractions from reflections. Diffractions themselves are then imaged while the azimuthally anisotropic velocity model is simultaneously estimated. Unlike the first two methods which use NMO for stacking velocity analysis, this third method exploits the velocity sensitivity of zero-offset post-stack migration.

I devote a chapter to each method, including individual introduction, theory, examples, and discussion sections. In the chapter on azimuthally-anisotropic NMO, I include a comparison with the semblance scan in terms of computational efficiency, which is also valid for time-warping. In the chapter describing time-warping, I focus on t-x domain CMP analysis. I demonstrate the unique flexibility of time-warping with examples of trace-sorting options such as "spiral-sorted" CMP gathers. In the chapter on velocity continuation, I include a section on path-integral similarity, which also serves to illustrate the possibility of future variants of diffraction imaging. I also discuss some of the possible geologic features that may be generating diffractions in the example field data sets. I conclude with a summary of the methods and key results, along with a qualitative comparison of the three methods.

Chapter 2

3D azimuthally anisotropic velocity-independent NMO

Background*

I have shown in the introduction that the traveltimes in observed seismic waveforms contain velocity information. Extracting this information amounts to measuring reflection event geometry and relating it to a moveout model. The conventional semblance scan measures event geometry by directly searching for a moveout surface which best resembles its traveltime surface. In 3D, just a single velocity value parametrizes a circular-hyperbolic surface, which describes isotropic NMO. However, in the case of azimuthally anisotropic NMO, at least three parameters must be measured to capture the associated elliptical-hyperbolic traveltime surface geometry. Even three parameters are difficult to measure with a semblance scan, so alternative approaches to velocity analysis are needed for anisotropic cases. In this chapter, I present the first of three alternative approaches to azimuthally anisotropic velocity analysis. The basic philosophy of this first method is the same as semblance-based analysis: measure reflection event geometry, and relate it to a moveout model. However, rather than scanning for surface geometry, I measure local slopes of traveltime surfaces throughout each CMP gather. Local slopes are simply an alternative way to measure surface geometry and therefore velocity. As I demonstrate though, they have powerful advantages over the semblance scan for measuring azimuthal anisotropy. Before this, I will first review some of the practical disadvantages of the semblance scan, and then introduce the concept of local-slope-based velocity independent

*Parts of this chapter are published in Burnett and Fomel (2009).

imaging.

Conventional manual velocity analysis by semblance scanning takes up a significant part of the time needed to process seismic data. Even with semi-automated picking tools, this phase of a typical processing flow alone may take weeks or even months for modern 3D data sets. Accurate automated traveltime picking algorithms are the main tools for modern velocity analysis, and have greatly reduced the time and manual work required to hand-pick velocities (Siliqi et al., 2003). However, these tools may still require significant manual inspection and editing for quality control.

The conventional production processing flow does not include picking azimuthally-dependent velocities, but two approaches are commonly used to handle and characterize azimuthal variations in velocity. The first, and historically more popular approach, is to sort CMP gathers into azimuth sectors, and then perform isotropic velocity analysis, processing, and migration on each sector. The individual moveout parameters from all sectors are plotted together, and then fit with a sinusoid to characterize the principal (fastest and slowest) moveout directions and the percentage of anisotropy. Grechka et al. (1999) describe another approach, where NMO is first performed with a smooth global velocity model. If apparent anisotropy is detected, trace-to-trace traveltime shifts are estimated automatically, and each traveltime surface is fit with an ellipse characterized by the moveout slowness matrix $\mathbf{W}$. The second approach has become more popular in production because of its robustness. In a case-study comparing the two approaches, Lynn (2007) provides an example where the non-sectoring approach yields a more reliable azimuthal velocity model.

The concept of local slope-based velocity-independent imaging (Ottolini, 1983b) is attractive because it can be very efficient when compared with the time and manual work required to hand-pick velocities (Fomel, 2007b). The underlying strategy of velocity-independent imaging relies on measuring traveltime slopes throughout the data set rather than hyperbolic traveltimes or velocities

themselves (Wolf et al., 2004). Fomel (2002) demonstrates that plane-wave destruction filters provide an automated and effective way to measure local slopes in a seismic volume. Measured slopes can then be used to automate any common time-domain imaging step (Fomel, 2007b). Previous work concerning automatic moveout corrections does not extend to the 3D case. In doing so here, I demonstrate that the azimuthal flexibility of automatic moveout correction in 3D is especially useful in the presence of real or apparent azimuthal anisotropy.

Rather than using a single picked velocity profile to apply the NMO correction, using the local slopes of a given 3D reflection event allows the event to be flattened regardless of azimuthal variations in stacking velocity. In practice, these slopes can be measured automatically throughout the volume, so no traveltime surfaces need to be picked. Although originally designed to bypass the velocity analysis part of seismic imaging, the velocity-independent approach can actually be used to extract moveout or interval velocities throughout the data set as data attributes (Fomel, 2007b; Burnett and Fomel, 2008a; Casasanta and Fomel, 2010). The method proposed in this chapter also suggests that, in the azimuthally anisotropic case, the orientation of the symmetry axes can automatically be estimated as an attribute in theory by measuring local curvatures throughout a multiazimuth CMP gather.

I first present theoretical expressions for azimuthally anisotropic moveout parameters as volumetric attributes. These attributes are theoretically interesting and may have applications in localized imaging strategies, but they are generally not stable at far offsets. So, I also demonstrate a novel, more robust, least-squares fitting scheme for matching the elliptical-hyperbolic moveout parameters with the local slope information. Synthetic and field examples are used to validate 3D azimuthally anisotropic velocity-independent NMO and show the variety of potential applications.

Theory

Equation 1.6 can be expanded to the form,

$$t\left(\mathbf{x},\mathbf{W}\right)=\sqrt{t_0^2+x_1^2W_{11}+2x_1x_2W_{12}+x_2^2W_{22}}. \tag{2.1}$$

Geometrically, equation 2.1 predicts an elliptical-hyperbolic traveltime surface on a CMP gather for the variety of cases where either real or apparent azimuthal anisotropy is present. The local inline and crossline slopes of traveltime events can be measured automatically by PWD filters, which can then be related to the conventional moveout slowness parameters by taking the derivative of 2.1 with respect to x_1 and x_2. Ignoring higher order terms or assuming the parameters vary slowly along x_1 and x_2, gives a first-order approximation of how the measured slopes relate to conventional moveout parameters:

$$p_1(t,\mathbf{x})=\frac{\partial t}{\partial x_1}=\frac{W_{11}x_1+W_{12}x_2}{t}, \tag{2.2}$$

$$p_2(t,\mathbf{x})=\frac{\partial t}{\partial x_2}=\frac{W_{22}x_2+W_{12}x_1}{t}. \tag{2.3}$$

By substitution back into 2.1, I arrive at the velocity-independent expression for 3D elliptical moveout in terms of local slopes:

$$t_0=\sqrt{t^2-t\left(p_1(t,\mathbf{x})x_1+p_2(t,\mathbf{x})x_2\right)}. \tag{2.4}$$

Equation 2.4 is a 3D extension for the 2D equation from Ottolini (1983b). Notice that only two parameters (p_1 and p_2) must be measured to completely predict the NMO corrected time. These

parameters can be measured automatically using a local slope estimation algorithm, such as plane-wave destruction (Fomel, 2002). Replacing a three-parameter model with two parameters may seem counter-intuitive in terms of completely describing a surface. However, one must keep in mind that the slope estimates are functions of the data coordinates—they are volumetric attributes. In other words, instead of parametrizing the entire surface with three single-valued parameters (W_{11}, W_{12}, W_{22}), I use two functions: $p_1(t, \mathbf{x})$ and $p_2(t, \mathbf{x})$. These two functions actually contain far *more* geometric information than the three-parameter model, as I demonstrate further in Chapter 3.

As equation 2.4 suggests, azimuthally anisotropic NMO can indeed be performed automatically, without ever measuring the velocity model. Automated processes allow one to save time, but it may seem that the insight and information gained during a more interactive conventional processing flow would be lost through automation. A significant part of production velocity analysis involves picking or examining the velocity model directly, which provides an early and intuitive link between the seismic data and the subsurface geology. The velocity model may also be useful in subsequent conventional imaging steps. Further, as discussed in the introduction, the velocity model and anisotropy information are themselves invaluable sources of geologic information, so an ability to extract these parameters is desirable.

Local slopes naturally measure surface geometry—regardless of actual surface type—but if the events are elliptical-hyperbolic as described by equation 2.1, then the local slope functions can be analytically related to the velocity model parameters of $\mathbf{W}$. The relation between local slopes and moveout velocity has been documented for the 2D isotropic case (Ottolini, 1983b; Wolf et al., 2004; Fomel, 2007b). In the 3D case where apparent or real azimuthal anisotropy is present, we must relate each of the three parameters of $\mathbf{W}$ to the slope functions. Simply rearranging equations

2.2 and 2.3 gives expressions for W_{11} and W_{22}:

$$W_{11} = \frac{tp_1 - W_{12}x_2}{x_1} \tag{2.5}$$

and

$$W_{22} = \frac{tp_2 - W_{12}x_1}{x_2}. \tag{2.6}$$

Both of these parameters require an estimate of W_{12}. A first-order approximation of W_{12} can be found by differentiating equation 2.2 with respect to x_2 or equation 2.3 with respect to x_1:

$$W_{12} = t\frac{\partial p_1}{\partial x_2} + p_1p_2 = t\frac{\partial p_2}{\partial x_1} + p_1p_2 = tp_{12} + p_1p_2. \tag{2.7}$$

Since local slopes are measured as a volumetric attribute, the inline and crossline local slopes comprise volumes with the same dimensions and coordinates as the input CMP gather. Applying a 1D derivative filter to these volumes allows one to obtain either mixed-derivative in equation 2.7, and solve for the apparent anisotropy angle β using equation 1.9 or 1.10. Like the other velocity model parameters, this angle can also then be expressed in terms of local slopes. Combining equations 2.5, 2.6, and 2.7 yields

$$W_{11} - W_{22} = \frac{t}{x_1x_2}[x_2p_1 - x_1p_2 + (p_{12} + (x_1^2 - x_2^2)\frac{p_1p_2}{t})]. \tag{2.8}$$

Now everything needed to express β independently of velocity is found in equations 2.7 and 2.8. Combining them with equation 1.9 gives,

$$\beta(t,\mathbf{x}) = \frac{1}{2}\tan^{-1}\left(\frac{2x_1x_2(tp_{12}+p_1p_2)}{t(x_2p_1-x_1p_2)+(tp_{12}+p_1p_2)(x_1^2-x_2^2)}\right) - c. \tag{2.9}$$

where $c = \pi/2$ when $W_{11} < W_{22}$ and $c = 0$ when $W_{11} \geq W_{22}$. Implementing equation 2.9 creates an attribute $\beta(t,\mathbf{x})$ for each input data sample describing the counter-clockwise azimuthal angle from the acquisition coordinates to the symmetry coordinates. Applying the NMO correction to this attribute volume yields $\beta(t_0,\mathbf{x})$, which should theoretically be constant at each time-slice if the moveout were exactly described by equation 2.1.

Finding local estimates of slowness and anisotropy parameters using equations 2.5-2.9 remains at this point only an interesting theoretical idea, but may find application in localized processing strategies. A more robust and practical approach to extracting velocity and anisotropy parameters is to exploit the shear number of volumetric slope measurements made to perform the velocity-independent NMO correction. For each event, the NMO correction applies a shift of time-squared,

$$\Delta(t_0,\mathbf{x}) = t^2(\mathbf{x}) - t_0^2(\mathbf{x}), \tag{2.10}$$

which can be automatically computed for every output coordinate using equation (2.4) and stored as another volume of the same dimensions. Once NMO is applied, the time axis of the CMP gather represents t_0, so the slowness matrix $\mathbf{W}$ and β should each theoretically be constant for a fixed t_0 value. Given a CMP gather with dimensions $(n_{x_1} \times n_{x_2} \times n_t)$, each time-slice from either the data or one of the attribute volumes can be viewed as an $(n_{x_1} \times n_{x_2})$ matrix, which can be re-indexed into a vector of length $(n_{x_1} \times n_{x_2})$. If the x_1 and x_2 indexes from the time-slice are i and j respectively, then the value from position (i,j) in the matrix is mapped to the $k = i + jn_{x_1}$ position in the

vector. Using this notation, a highly overdetermined problem follows from writing equation 2.1 as a matrix-vector multiplication:

$$\mathbf{\Delta} = \mathbf{X}\mathbf{w}. \tag{2.11}$$

where the k^{th} element of $\mathbf{\Delta}$ is,

$$\Delta_k = \Delta(t_0, x_{1i}, x_{2j}), \tag{2.12}$$

the k^{th} row of $\mathbf{X}$ is given by the vector,

$$\mathbf{x}_k = \begin{pmatrix} x_{1i}^2 & x_{2j}^2 & 2x_{1i}x_{2j} \end{pmatrix}, \tag{2.13}$$

and

$$\mathbf{w} = \begin{pmatrix} W_{11} \\ W_{22} \\ W_{12} \end{pmatrix}. \tag{2.14}$$

Linear system 2.11 has $(n_{x_1} \times n_{x_2})$ equations with only three unknowns. By solving 2.11 for each time-slice in the output CMP, I construct the slowness matrix $\mathbf{W}(t_0)$, and use it with equations 1.9, 1.8, and 1.11 to extract the coordinate rotation angle $\beta(t_0)$, the principal velocities, and the NMO slowness as a function of azimuth, $S(t_0, \theta)$.

Examples

I provide two examples to illustrate the performance of the 3D azimuthally anisotropic velocity-independent moveout correction and velocity analysis. In the first example, I consider a

simple 3D synthetic CMP gather with four events, labeled A-D from earliest to latest, each with a different degree of apparent azimuthal anisotropy (Figure 2.1(a)). The synthetic CMP gather in Figure 2.1(a) was created by first specifying the moveout slowness matrix, **W** for each event. Each of the four events was modeled individually by applying inverse 3D NMO to a flat reflection based on equation 1.6. The exact parameters used to model the four events are specified in Table 2.1. The four events were then added together into a single CMP gather with a small amount of random noise (10% of the signal amplitude). The result of this modeling approach differs from real cases in that the traveltime surface for each of the events is completely independent from overlying events. However, this simple modeling is sufficient to specify the exact moveout slownesses of each event for testing purposes.

Event Moveout Parameters					
Event	t_0 (s)	$W_{11}(s^2/km^2)$	$W_{22}(s^2/km^2)$	$W_{12}(s^2/km^2)$	$\beta(^\circ)$
A	0.59	0.14	0.16	-0.01	14.0
B	1.53	0.30	0.30	-0.04	-44.3
C	2.51	0.32	0.26	-0.03	-21.8
D	3.41	0.24	0.25	-0.005	26.57

Table 2.1: Moveout parameters used for events in Figure 2.1(a).

Conventional velocity semblance scans may yield multiple peaks for the same event when apparent azimuthal anisotropy is present. One must interpret the correct velocity in these areas, which can lead to inconsistent results between different processing geophysicists. The cause of multiple semblance panel peaks can also be ambiguous (multiples, noise, anisotropy, etc.), and properly resolving this ambiguity can add even more time and work to the production approach. So I first examine the effect of picking a single-parameter isotropic velocity on a 3D CMP gather where azimuthal anisotropy is present. Figure 2.1(b) shows a possible result of picking a single velocity profile which flattens certain events in either the inline or crossline view. If an intermediate

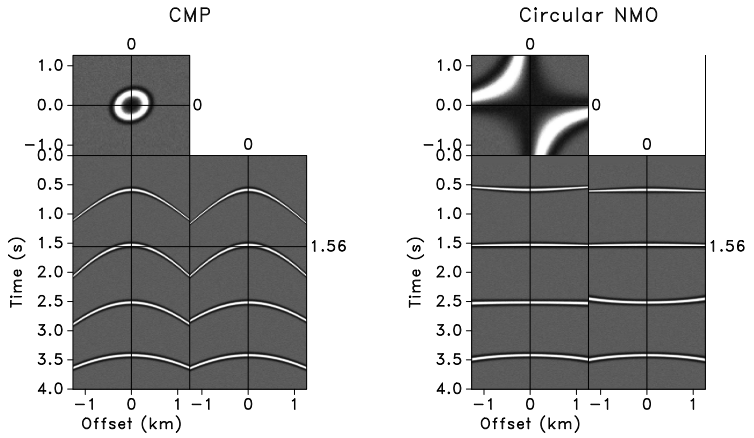

(a) (b)

Figure 2.1: (a.) A synthetic 3D CMP gather with four events of varying apparent elliptical anisotropy (Events A-D ordered from top to bottom). The three panels in the display show a time-slice view (upper square panel), a crossline view (central panel), and an inline view (right panel) of the same volume. (b.) An isotropic NMO correction using a picked velocity function appropriate for flattening certain events. At best, isotropic NMO can flatten either the inline or crossline directions well, but there is no single velocity function that will flatten both. chapter-pnmo/synthetic cmp3d,nmo063d

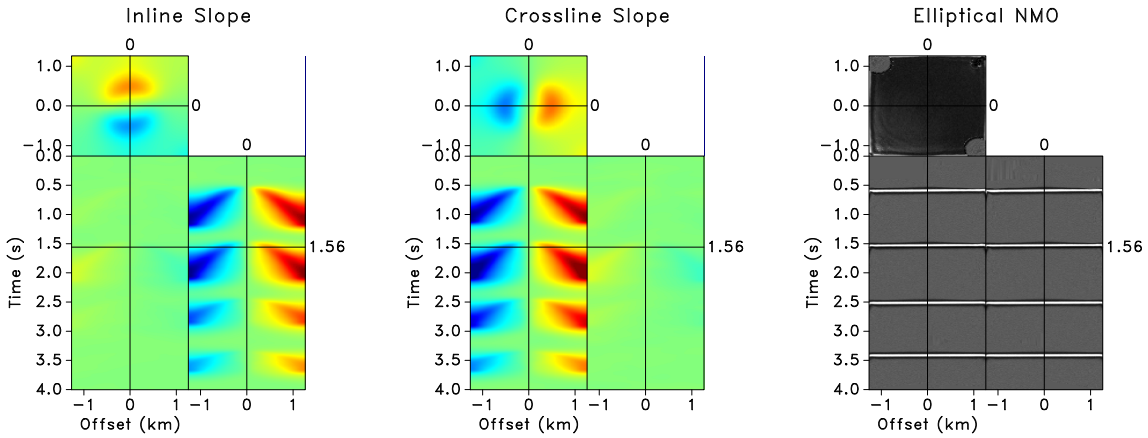

(a) (b) (c)

Figure 2.2: The (a.) inline and (b.) crossline slopes of the CMP gather from Figure 2.1(a). (c.) These slopes are used with equation 2.4 to automatically perform the proposed elliptically anisotropic moveout correction. All four events are flattened perfectly where the slopes are not aliased. chapter-pnmo/synthetic pxsmooth3d,pysmooth3d,PNMO3d

velocity value is chosen for each event, both directions are flattened poorly. Event B represents a particularly difficult case for the production approach; the symmetry axes are nearly 45° from the acquisition axes, which makes the apparent moveout velocities along the x_1 and x_2 axes practically equal. A production velocity analysis is likely to not even detect the anisotropy in this case, because viewed from the acquisition axes, event B appears isotropic. The time-slice panel of Figure 2.1(b) reveals the poor performance of the isotropic NMO correction for event B along other source-receiver azimuths.

By measuring the local slopes of an input CMP gather as volumetric attributes, the geometry of each traveltime surface is captured, even away from the x_1 and x_2 acquisition axes. Figures 2.2(a) and 2.2(b) show sections of the automatically measured inline and crossline slope volumes for the CMP from Figure 2.1(a). The time-slice views clarify that the slopes are measured in the x_1 and x_2 directions throughout the volume, not just along the x_1 and x_2 zero-offset axes. Comparison of the slope volumes with Figure 2.1(a) also shows that there are clearly non-zero slopes in areas without data. No initial slope fields were used to get these measurements, but the plane-wave destruction filter results were regularized with a smoothing constraint via shaping regularization (Fomel, 2007b,a). This constraint is enforced to help ensure that the moveout correction varies both spatially and temporally in a stable fashion. In Figure 2.2(c), the velocity-independent elliptically anisotropic moveout correction is applied using these slopes, and all of the events are flattened well in all azimuths.

The time-slice view of Figure 2.2(c) now shows the overall superior performance of the velocity-independent correction, but also reveals its limitations. As events become steep relative to the trace spacing, local slope measurements can be aliased. Towards the corners of the example gather, the slopes become too steep to be measured reliably, and in these areas, the automatic

moveout correction performs poorly. In field data, crossline trace spacing is often much coarser than inline spacing, which may lead to similar aliasing problems. However, the effects of aliasing can often be mitigated with a few simple extra steps. By first applying a constant-velocity isotropic NMO correction to the data before measuring slopes, the events will be flatter and less likely to have aliased slopes at far offsets. An inverse NMO correction using the constant velocity can then be applied to the measured slopes. The constant velocity can then be converted to p_1 and p_2 components and added to the slope measurements to obtain the unaliased slope fields of the original input CMP gather.

A common-offset gather perspective of the same test is shown in Figures 2.3(a) and 2.3(b). The traces from the synthetic CMP gather have been binned into offset and azimuth coordinates to display the sinusoidal signature of azimuthal traveltime variations. The various squared traveltime shifts applied by the automatic NMO correction were computed during implementation using equation 2.4, and then stored as a volumetric attribute ($\Delta(t_0, \mathbf{x})$) . For each of the events, time-slices of this volume are shown in Figures 2.4(a)-2.4(d). The elliptical variation is clearly displayed for events A, B, and C, but the subtle variation for event D makes it difficult to detect the apparent anisotropy using conventional methods.

Each time-slice from the time-shift volume was re-indexed into a vector following the scheme described in the previous section, and then equation 2.11 was used to yield $\mathbf{W}(t_0)$ by least-squares fitting. The results of this inversion are displayed in Figures 2.5(a)-2.5(c). At the times of the events, all three parameters have been extracted accurately. The shaping regularization used to ensure smooth slope fields also leads to similar smoothness in the $\mathbf{W}$ estimates. Because of the random noise in the synthetic data, slope measurements away from events appear also random. The best-fit surface through these random slopes tends to be a flat plane, which is characterized on a

CMP gather by zero slowness, causing the W_{11} and W_{22} estimates to tend toward zero between events. It is important to note that the values shown in Figures 2.5(a)-2.5(d) each rely on the accuracy of the NMO shifts computed at the corresponding value of t_0. Only the sparse times of this synthetic CMP gather with data have meaningful slope estimates and therefore meaningful $\mathbf{W}$ and β estimates.

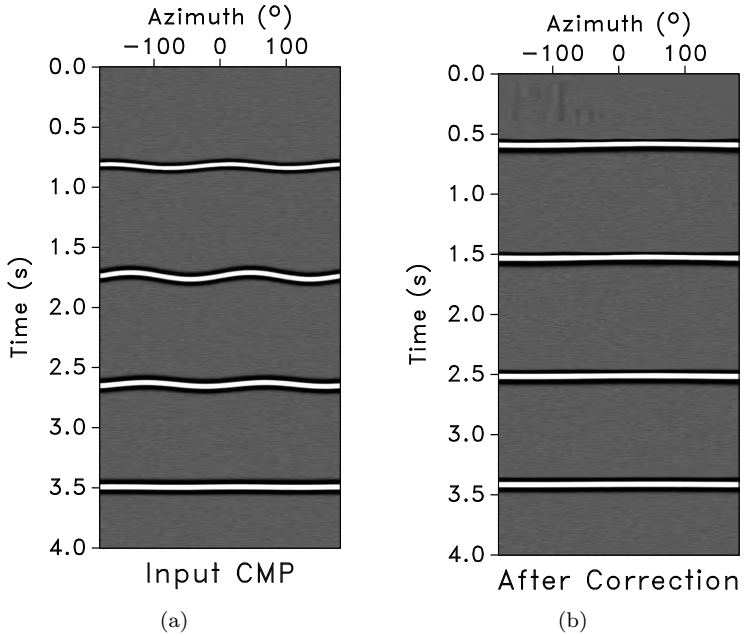

Figure 2.3: (a.) A common offset (0.75 km) display of CMP from Figure 2.1(a) with azimuth on the horizontal axis. (b.) The same traces after the automatic moveout correction. All events are shifted up to their appropriate t_0 and flattened. chapter-pnmo/synthetic oacmp,oaPNMO

The extracted moveout slowness matrices $\mathbf{W}(t_0)$ are used with equation 1.9 or 1.10 to estimate $\beta(t_0)$. The results of estimating $\beta(t_0)$ are displayed in Figure 2.5(d), and the values at the times of each event are accurate. I conclude this example by solving for NMO slowness-squared as a function of azimuth using $\beta(t_0)$ and the corresponding eigenvalues at each t_0 with equation 1.11. These results, shown in Figures 2.6(a)-2.6(d) show that for all four events, the angle of anisotropy is

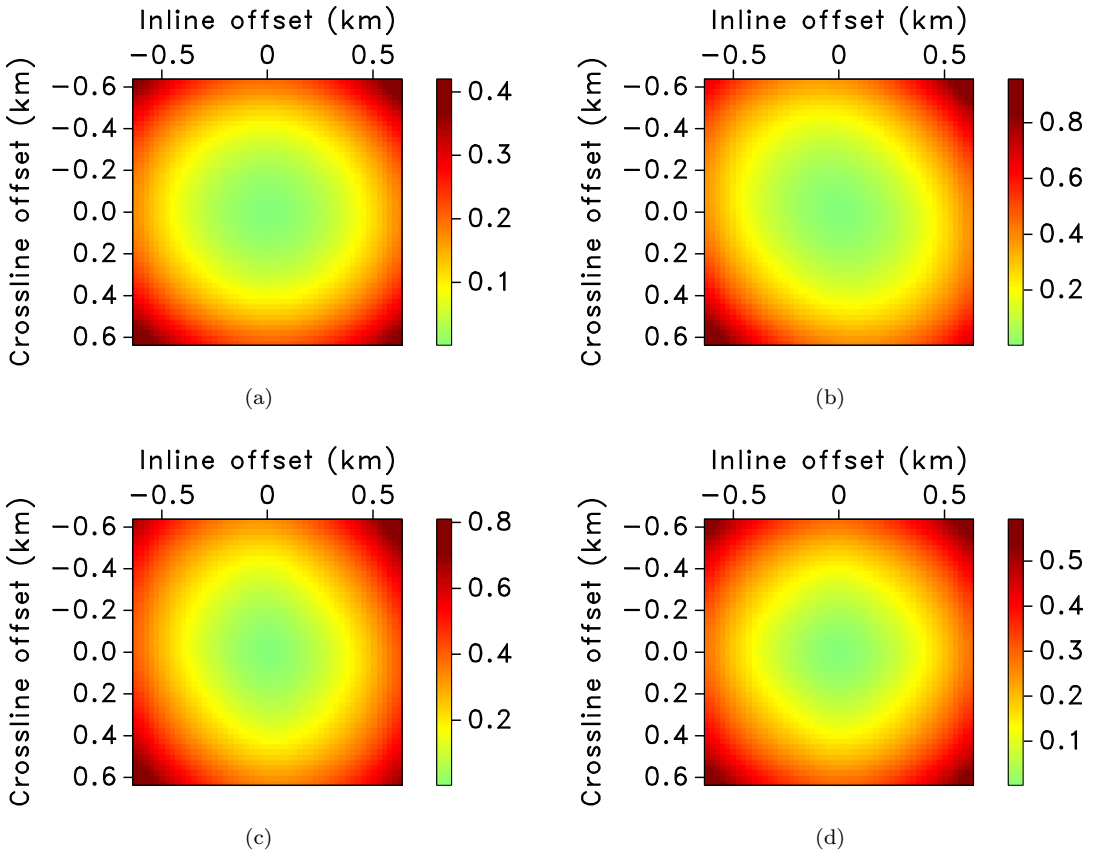

Figure 2.4: Traveltime squared shifts ($\Delta(t_0, \mathbf{x})$) for each event. (a.) Event A. (b.) Event B. (c.) Event C. (d.) Event D. chapter-pnmo/synthetic deltaTslice1,deltaTslice2,deltaTslice3,deltaTslice4

detected. From this volume, the principal moveout directions are readily determined, the fast and slow axes are resolved, and the percentage of anisotropy (ϕ) is measurable.

I next demonstrate a potential application of the automatic moveout correction on a real data example. In this case, I apply the automatic elliptically anisotropic moveout correction as a residual moveout correction. A subset of the McElroy data set from West Texas was formed into a supergather seen in Figure 2.7. Figure 2.8(a) shows a common offset (3.6-4.0 km) time-versus-azimuth display of the same data, where azimuthal anisotropy is evident for several events. In Figure 2.8(b), the magnitude of the local slope is shown for the initial data. The areas with higher slope values highlight areas that were not ideally flattened by the prior isotropic NMO correction. The region of the highest slopes along the top of the figure is due to the proximity of the prior NMO mute at about 0.8 s. Figure 2.8(c) shows the results of applying two iterations of the proposed moveout correction. Further iterations will continue to flatten later events as distortions from overlying layers are removed. The events in the results are already noticeably flatter, and will therefore produce a cleaner stack. In this example, I have applied the method to a supergather, which makes azimuthal anisotropy measurements more robust for low-fold data sets, but supergathers cover a very broad region of the subsurface. In more modern multiazimuth data sets, we can apply the method to high-fold 3D CMP gathers, which will allow better resolution of the velocity model.

Discussion

Many advancements have been made in semi-automated traveltime picking schemes which have made the velocity analysis phase of a conventional seismic data processing flow much more efficient. However, considerable time is still required to manually check the quality of the assisted picking, and this remains a time-consuming step in the conventional processing flow, especially in

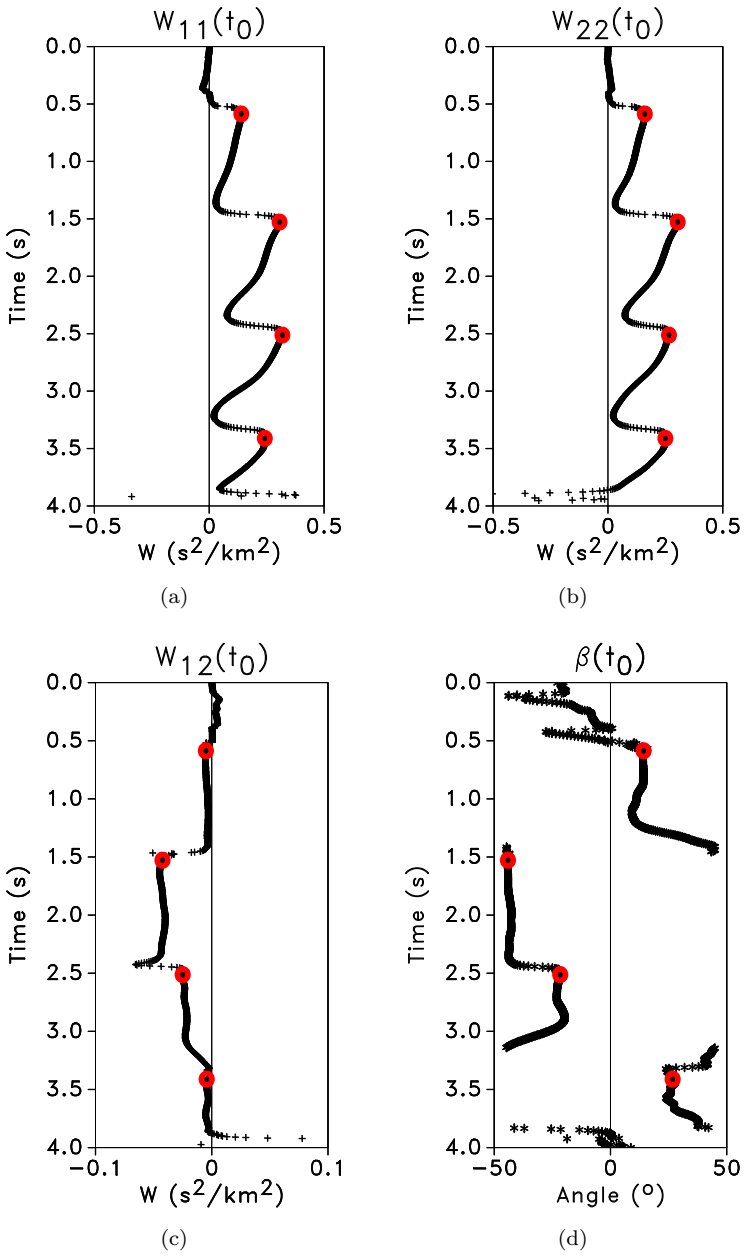

Figure 2.5: Elements of $\mathbf{W}(t_0)$ inverted from $\Delta(t_0, \mathbf{x})$ surfaces: (a.) $W_{11}(t_0)$. (b.) $W_{22}(t_0)$. (c.) $W_{12}(t_0)$. (d.) Azimuth angle $\beta(t_0)$ computed from $\mathbf{W}(t_0)$. Red circles indicate correct parameters. chapter-pnmo/synthetic W11-LSfit,W22-LSfit,W12-LSfit,Beta-LSfit

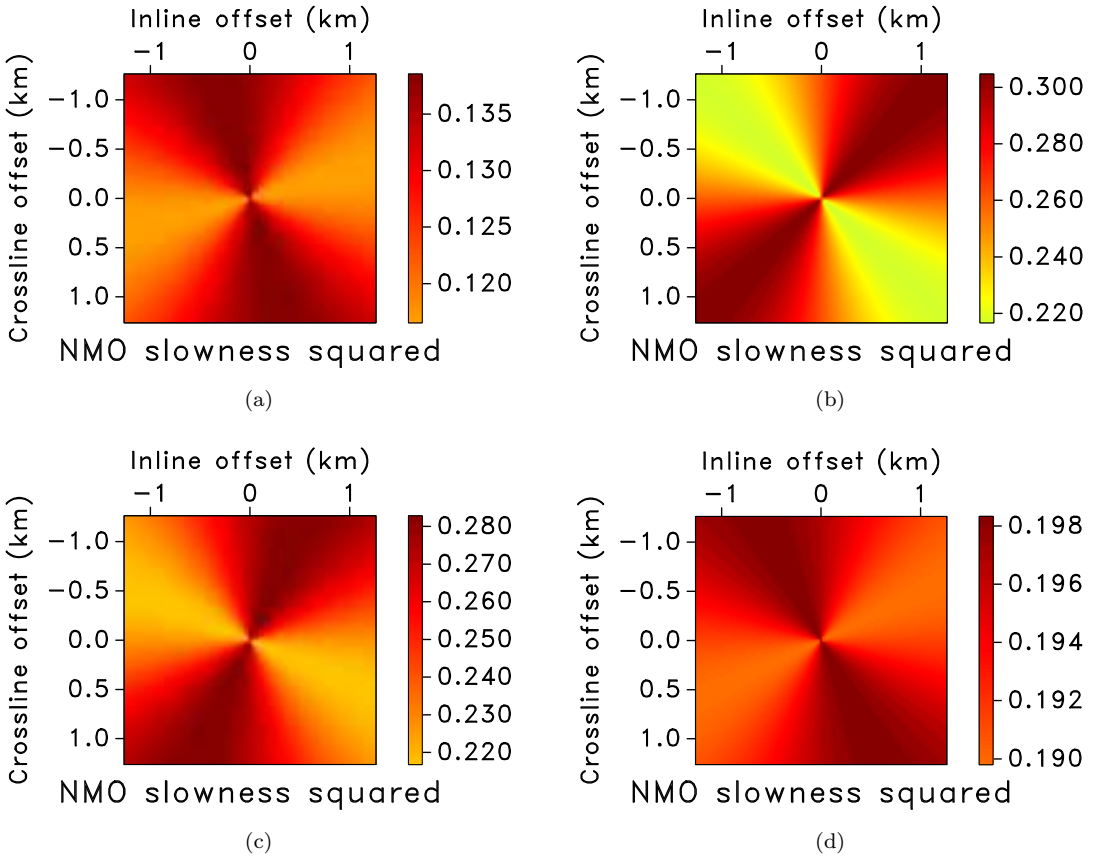

Figure 2.6: Timeslice views of NMO slowness-squared values computed for each event. (a.) Event A. (b.) Event B. (c.) Event C. (d.) Event D.

chapter-pnmo/synthetic slowsqrdslice1,slowsqrdslice2,slowsqrdslice3,slowsqrdslice4

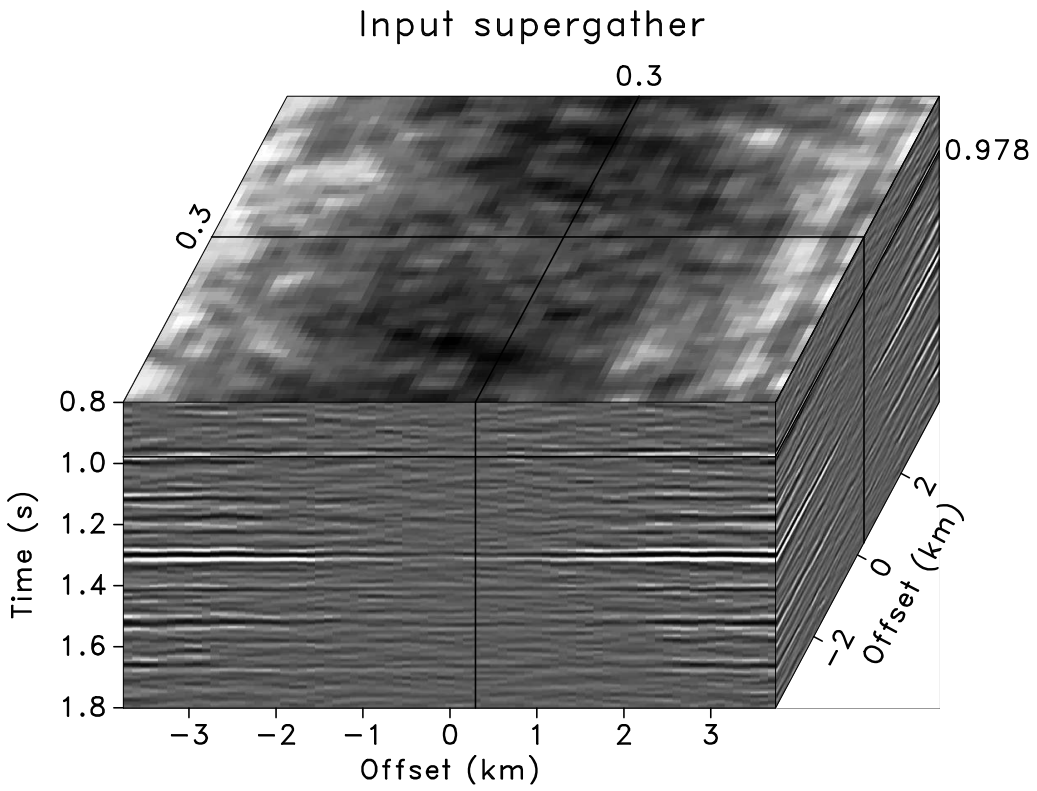

Figure 2.7: 3D view of a supergather from the McElroy data set, West Texas, US. Although the data have been isotropically NMO corrected, the time-slice view shows a subtle directional trend to the flatness of an event at 0.978 s. chapter-pnmo/../nmo3/mcelroy supercube

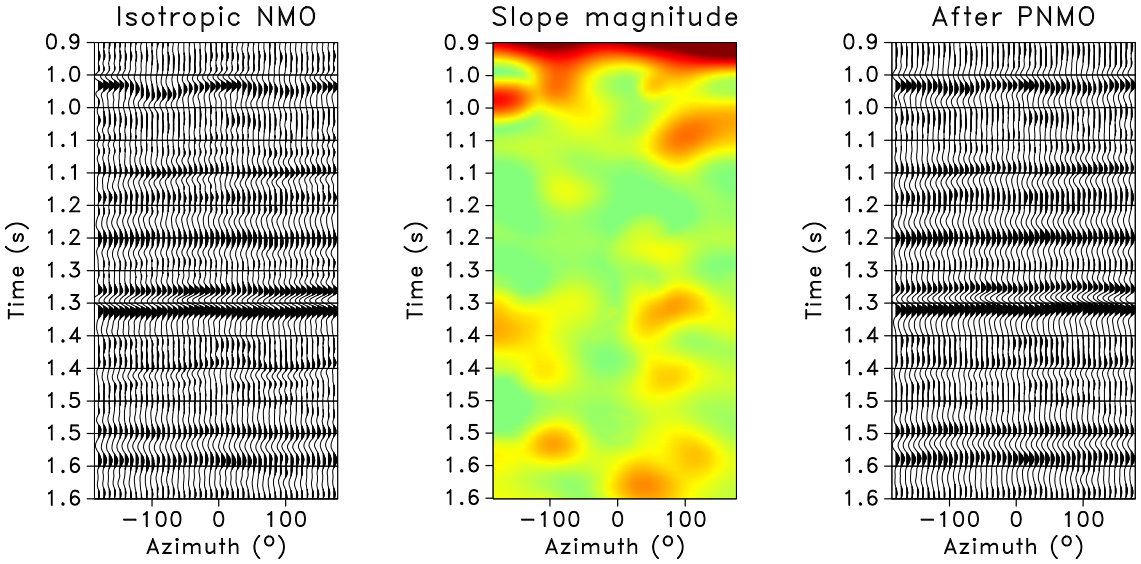

(a) (b) (c)

Figure 2.8: A time-versus-azimuth panel of traces for a range of offsets from 3.6-4.0 km from the McElroy data set. The central panel shows local slope magnitudes corresponding to the left input panel. The slope magnitude was computed as $\sqrt{p_1^2 + p_2^2}$. The same data after azimuthal velocity-independent NMO has been applied as a residual moveout correction are shown on the right. chapter-pnmo/../nmo3/mcelroy super21anisow,pmag3anisow,pnmooa2anisow

3D. Still, the ability to manually asses the quality of the results will always be important, so a similar procedure can be used for 3D velocity-independent NMO. In production applications, the automatically measured slope fields from a subset of CMP gathers should be inspected manually. Slopes are very intuitive to understand and easy to compare to the input data. An overlay or side-by-side display of the two, combined with the automatic NMO performance provides efficient and accurate quality control criteria.

Plane-wave destruction filters provide a truly automated approach to velocity analysis, as they can be used without any user-selected input parameters. Here, I have used finite-difference plane-wave destructors, which, as described by Fomel (2002), can be given a user-supplied initial estimate of the slope field. Providing an initial slope estimate helps improve the efficiency of the slope-detection and can help estimate conflicting slopes. In all of the examples above, no initial slope field was provided. The output slope fields are computed using smoothing regularization, which helps make the moveout correction more robust, and provides a way for the user to interact with the slope detection performance. If the seismic data are particularly noisy, a more aggressive smoothing can help make a more consistent automatic NMO correction, while for clean data, less smoothing yields a better resolved localized slope field.

Since the velocity model is estimated by NMO flattening, the results are effective stacking parameters. In realistic geologic cases containing a stack of layers, each layer may have a different orientation of azimuthal anisotropy. The azimuthally-dependent traveltime variations caused by wave propagation in the upper layers will be superimposed on the reflection events of underlying layers. While measuring the stacking parameters is shown to be straightforward through the velocity-independent approach, inverting for interval parameters would require these effects to be unraveled through the use of layer-stripping (Hake, 1986), a Dix-type inversion (Grechka et al., 1999; Grechka

and Tsvankin, 2002), or taking the derivative of the slope field with respect to time (Fomel, 2007b). If the effects from overlying layers distort later traveltime surfaces enough such that they are no longer elliptical-hyperbolic as suggested by equation 2.1, then the moveout correction will not be complete for the later events. However, as seen in the field data example, the velocity-independent moveout method can be used as a residual correction, with no changes to the procedure. The later events with incomplete moveout correction can therefore be corrected with iterated applications of the method. Another complication arises in the residual moveout case though, if one wants to extract velocity parameters such as the azimuth angle or moveout slownesses. The equations presented here for parameter extraction were derived for a single-pass NMO correction. Extending the parameter estimation method to the residual moveout case requires summing all applied traveltime shifts (initial and residual) before fitting with parameters. I could not recover velocity parameter estimates on the McElroy supergather, as the initial NMO correction and its corresponding velocity were unknown.

Conclusions

Measuring local slopes is a thorough and azimuthally flexible way to characterize traveltime surface geometry, which, in the 3D case, provides useful information about azimuthal variations in moveout velocity. I have demonstrated an application for this feature in performing an azimuthally anisotropic moveout correction in 3D. No velocities are picked in order to perform this moveout correction, and since I use plane-wave destruction filters to measure local slopes, the entire process is automated. Still, local moveout velocities can be estimated from this method in two ways. First, velocity parameters can be calculated directly as a function of the local slopes, and the azimuthal angle of anisotropy can be estimated locally if one measures the first mixed-derivative of the traveltime surfaces at each point. Second, by recording the traveltime shifts applied by the automatic NMO correction, I have formulated a highly overdetermined linear system to solve for moveout parameters

as a function of time. This inversion scheme was shown to be very accurate on a synthetic data example.

Even in multi-layer cases, where conflicting azimuthal anisotropies are present, the proposed moveout correction itself can be performed accurately and automatically without velocity or parameter estimation. Further, the effective moveout parameters can be estimated by fitting the shifts applied by the automatic correction. This shows the first example of the common strategy shared among methods in this dissertation: perform a velocity-independent imaging step first (here, slope-based NMO), then find the effective parameters which correspond to that correction (here, by least-squares fitting of NMO-corrected traveltime surfaces). Extensions of this method following an iterative scheme analogous to a layer-stripping or Dix-type inversion strategy may provide a powerful option to automatically recover interval parameters as well.

The computational cost is one of the main advantages of velocity-independent NMO over the semblance scan. In Chapter 1, I explained the multi-parameter semblance scan cost to be $\mathcal{O}(N_{\mathbf{x}} \times N_{t_0} \times N_v^{N_p})$. In the azimuthally anisotropic case, $N_p = 3$, and for a reasonable $N_v = 100$, the approximate cost can be written as $N_{\mathbf{x}} \times N_{t_0} \times 1,000,000$. For azimuthal velocity-independent NMO, the dominant cost by far, is slope estimation. Slope estimation also has a complexity proportional to the dataset, but then instead of scanning parameters, there is the cost of applying a nonlinear filter. This results in a complexity of $\mathcal{O}(N_{\mathbf{x}} \times N_{t_0} \times N_f \times N_i)$, where N_f is the number of filter coeficients and N_i is the number of iterations (both typically on the order of 10^1). So, for 3D azimuthally-anisotropic velocity-independent NMO, the approximate cost of $N_{\mathbf{x}} \times N_{t_0} \times 100$, which is about the same as a single-parameter isotropic semblance scan, and four orders of magnitude less expensive than a three-parameter scan.

In this chapter, I have applied an automatic, velocity-independent physical NMO correction

to seismic gathers and their recorded time-attribute volumes. The physical NMO correction still assumes hyperbolic moveout based on simple midpoint reflection geometry, which commonly fails at far offsets. In the next chapter, I generalize the linear parameter estimation approach developed here by employing a non-physical event flattening technique called "warping". This extends my approach to the problem of fitting an arbitrarily-shaped event surface in an arbitrary gather type.

Chapter 3

Moveout analysis by time-warping

Background

In the previous chapter, I assumed only azimuthal variations in the reflection hyperbolic moveout velocity. The ideal moveout model should account for azimuthal variations, but it should also account for nonhyperbolic behavior. Semblance-based methods are already inefficient in obtaining just the three-parameters needed to describe azimuthal variations. Measuring a more ideal elliptical-nonhyperbolic model may require five or more parameters (Vasconcelos and Tsvankin, 2006; Fomel and Stovas, 2010). In this chapter, I propose a traveltime inversion approach to moveout parameter estimation using automatic flattening of gathers. Like the velocity-independent NMO correction in Chapter 2, I directly measure local slopes to obtain event geometries which can then be used to extract velocity information. I again use plane-wave destruction filters to automatically measure local slopes throughout an input gather, but instead of directly relating the slopes to a hyperbolic moveout velocity, I use the slopes to predict the traveltime surfaces themselves. This leads to a method which permits azimuthal and/or nonhyperbolic variations.

Here, traveltime surfaces are first predicted, and then flattened by a nonphysical flattening method called warping (Lomask et al., 2006; Fomel, 2008). Warping is "nonphysical" in the sense that it is purely a signal processing correction—not based on traveltime geometries predicted by CMP reflection physics. By applying the same warping correction to a time attribute volume, the time shifts needed to flatten each event can be computed, similar to the fitting method described

in Chapter 2. From these shifts, best-fit physical parameters of *any* type of moveout curve—from circular-hyperbolic to elliptical-nonhyperbolic or beyond—can theoretically be found using a linear or non-linear least-squares fitting scheme.

While the need to characterize the effects associated with azimuthal anisotropy is increasingly common, it is also common to have the effects of vertical-transverse isotropic (VTI) media present in the seismic records. VTI type anisotropy is so common that it is often synonymous with the term, "seismic anisotropy" (Thomsen, 1986), as it is usually associated with thin (relative to the seismic wavelength) horizontal bedding—a geologically common case. VTI type anisotropy or heterogeneity may introduce nonhyperbolic moveout effects on the far offsets of CMP gathers, which can be superimposed on top of any effects of real or apparent azimuthal anisotropy. Sublette et al. (2008) show that azimuthal variations in moveout behavior can be masked by the effects of nonhyperbolic moveout. It can therefore be expected that the benefits of multiazimuth acquisition will not be fully realized until an efficient, multiazimuth, nonhyperbolic velocity analysis method becomes practical. The approach to velocity analysis in this chapter is well-suited for efficient and automatic estimation of dense, multiazimuth, nonhyperbolic, 3D velocity models. I provide 3D synthetic and field data examples using elliptical-hyperbolic moveout, and a 2D field data example of nonhyperbolic moveout.

Time-warping

The concept introduced here called *time-warping* evolved from the velocity-independent imaging strategies originating with Ottolini (1983b) discussed in Chapter 2. These velocity independent strategies rely on the connection between the slopes of traveltime surfaces and their corresponding moveout velocities. Local slope detection tools such as plane-wave destruction filters

(Fomel, 2002) are used to automatically measure these slopes, which can then be used to perform any time-domain imaging step (Fomel, 2007b). In the case of the NMO correction, the local slopes can be used to directly estimate hyperbolic moveout velocities or to automatically apply the moveout correction without knowledge of the velocity model. The result is a flattened CMP gather with an associated velocity model, in which stacking velocity information is stored as a volumetric attribute, $W_0(t_0, x_1, x_2)$, or multiple attributes, $\mathbf{W}(t_0, x_1, x_2)$, in the azimuthally anisotropic case. Conventional processing flows require a velocity profile rather than this attribute format, therefore I developed a simple method in equations 2.10-2.14 to solve for the best-fit elliptical-hyperbolic velocity profile for a given gather. In general though, the elliptical-hyperbolic NMO equation 2.1 is only one out of many options to use as "the NMO equation". Any other NMO equation can also be rearranged into a similar form to 2.11. Fixing t_0 gives the linear system in the same notation as equations 1.1 and 2.11,

$$\mathbf{\Delta} = \mathbf{X}\left[\mathbf{m}\right], \tag{3.1}$$

where $\mathbf{X}$ is now generally equivalent to $\mathbf{G}$ from equation 1.1, but is now viewed as any linear or nonlinear operator describing the assumed event geometry. If the case of NMO, $\mathbf{X}$ is more specifically of the same form a $\mathbf{F}_{NMO}$ from equation 1.5. The vector $\mathbf{m}$ is again a list of moveout model parameters such as stacking velocities and/or anisotropy coefficients.

This simple moveout parameter fitting scheme was only possible in Chapter 2 because I extracted the time shifts, $\mathbf{\Delta}$, *automatically* using a velocity-independent NMO correction. However, in order to apply a velocity-independent moveout correction, one must assume a physical moveout behavior beforehand (hyperbolic, non-hyperbolic, etc.). It is possible to bypass making any assump-

tion about the moveout behavior by flattening the data first using a nonphysical method (Bienati and Spagnolini, 1998; Lomask et al., 2006; Gulunay et al., 2007; Fomel, 2010). Here, I use predictive painting (Fomel, 2008), which combines a reference trace with volumetric local slope information to predict the geometry of traveltime surfaces throughout a CMP gather. These prediction surfaces are then warped until they are flat. The warping process can be viewed as the application of a nonstationary shifting filter, and I store this filter to help measure the traveltime shifts $\mathbf{\Delta}$ without any moveout assumptions.

Measuring $\mathbf{\Delta}$ can be visualized by viewing t and t_0 themselves as volumetric attributes. For an input CMP gather, the time axis represents t defined in equation 2.10. This axis is the same for each trace, and if t is stored as an attribute for each sample in the CMP, it will form a laterally-invariant vertical gradient, $t(t, \mathbf{x})$ (see Figure 3.1(b)). More interesting though, is what the volumetric attribute of $t_0(t, \mathbf{x})$ looks like for an input CMP, as seen in the 3D example of Figure 3.1(c). I estimate $t_0(t, \mathbf{x})$ by iteratively projecting the input time-axis, t, along the local slope fields measured by plane-wave destruction filters. This technique is called predictive painting (Fomel, 2008), and I assume that isosurfaces of the predictive painting result follow the arbitrary geometries of each event. In this case, the corresponding synthetic data in Figure 3.1(a) were modeled using inverse NMO, so the isosurfaces of $t_0(t, \mathbf{x})$ perfectly follow traveltime surfaces.

The next step is to apply warping to each of the volumes in Figures 3.1(a)-3.1(c). After the flattening correction is applied to either the input data or its time-attributes, the time axis corresponds to t_0. As an attribute of the output CMP coordinates, $t_0(t_0, \mathbf{x})$ now monotonically increases downward (Figure 3.2(c)), which of course looks identical to $t(t, \mathbf{x})$ (Figure 3.1(b)). The warping filter itself is actually designed by optimizing the mapping between the predictive painting result $t_0(t, \mathbf{x})$ and this ideal vertical-gradient output attribute. Once designed, the warping filter will

flatten the events seen in Figure 3.1(a) to the results in Figure 3.2(a). However, the most valuable time attribute volume, $t(t_0, \mathbf{x})$ is shown in Figure 3.2(b). This volume comes from applying the stored warping filter to shift $t(t, \mathbf{x})$ by the same amounts used to flatten the data; hence the name "time warping". Finally, the left-hand side of equation 3.1 is found by subtracting the squares of the two warped time-attribute volumes, $\Delta(t_0, \mathbf{x}) = t^2(t_0, \mathbf{x}) - t_0^2(t_0, \mathbf{x})$, and taking time-slices through constant values of t_0.

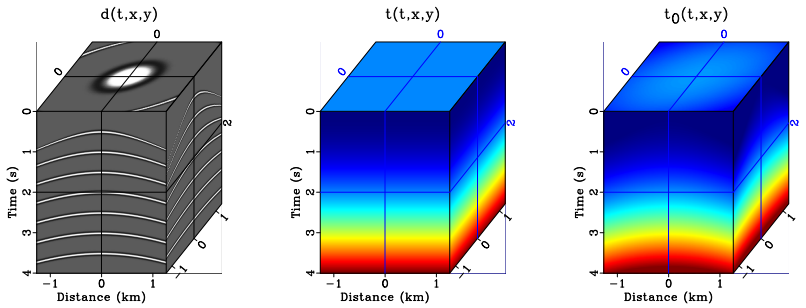

(a) (b) (c)

Figure 3.1: Uncorrected volumes of (a) synthetic data, (b) t-attribute, and (c) t_0-attribute. Note that these volumes are defined in input t-$\mathbf{x}$ coordinates. chapter-timewarp/../timewarp/elliptical cmpcube,timecube,t0oftcube

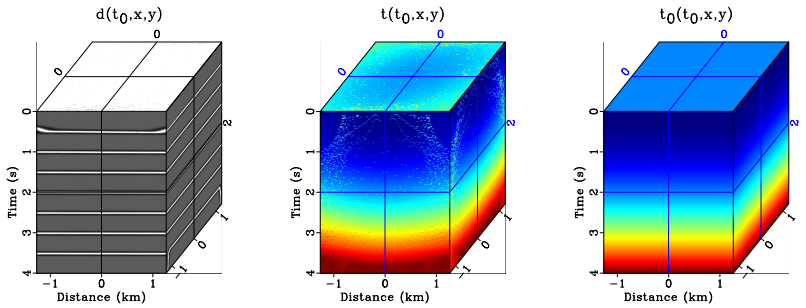

(a) (b) (c)

Figure 3.2: Warped volumes: (a) data, (b) t-attribute, and (c) t_0-attribute. Note that these volumes are defined in output t_0-$\mathbf{x}$ coordinates. chapter-timewarp/../timewarp/elliptical flat3cube,warpedtimecube,t0oft0cube

The method of time-warping can be summarized as a sequence of three techniques. First, predictive painting uses local slopes to delineate traveltime surfaces. Second, warping uses the predictive painting results to design a filter which optimally flattens the traveltime surfaces. The flattening predicted by the warping filter yields the time-shift information $\mathbf{\Delta}$. Third, the method of least-squares fits the time-shift information with a velocity model ($\mathbf{m}$) based on any desired moveout model ($\mathbf{X}$).

Time-warping allows the left-hand side of equation 3.1 to be estimated at each t_0, but, unlike the fitting approach developed for velocity-independent NMO, time-warping does not impose a hyperbolic assumption beforehand. This is the key advantage of time-warping which allows it to capture arbitrary surface geometries in any domain where flattening-based analysis or traveltime prediction is used. In other domains, $\mathbf{X}$ may be any of a broad range of imaging operators, not necessarily related to the conventional $\mathbf{F}_{NMO}$. Casasanta and Fomel (2010) have extended the time-warping approach to the τ-p domain where $\mathbf{X}$ is more closely an elliptical moveout operator than hyperbolic. Kazinnik and Burnett (2010) have applied time-warping to multifocusing and common reflection surface (CRS) imaging methods (Gelchinsky et al., 1999; Jager et al., 2001) where traveltime surfaces are parametrized across multiple CMP gathers. In the the following sections, I provide a brief "tour" of CMP-based time-warping applications, each of which is a special case of equation 3.1, where $\mathbf{X}$ remains related to $\mathbf{F}_{NMO}$.

Isotropic NMO

The simplest example of the time-warping method can be seen by re-writing the circular-hyperbolic NMO equation 1.4 as,

$$\Delta(t_0, \mathbf{x}) = W_0|\mathbf{x}|, \tag{3.2}$$

where $|\mathbf{x}|$ is the magnitude of the source-receiver offset. In the notation of 3.1, the k^{th} row of the isotropic NMO operator becomes,

$$\mathbf{X}_k = |\mathbf{x}|_k^2, \tag{3.3}$$

and the model parameter vector becomes the single-element,

$$\mathbf{m} = W_0. \tag{3.4}$$

The offset coordinates $\mathbf{x}$ of each trace are of course known, and for a fixed t_0, the left-hand side of equation (3.1) can be obtained from the first two steps of time-warping. Therefore, for each event in a gather of N-traces, we have a highly overdetermined system of N-equations with only one unknown (W_0). Solving this system for each t_0 gives the isotropic velocity profile $W_0(t_0)$.

Azimuthally Anisotropic NMO

For the many cases which give rise to apparent azimuthal anisotropy, I again re-write the elliptical-hyperbolic expression of Grechka and Tsvankin (1998) as:

$$\Delta(t_0, \mathbf{x}) = W_{11}x_1^2 + W_{22}x_2^2 + 2W_{12}x_1x_2. \tag{3.5}$$

Decomposing this expression into a vector multiplication reveals its appearance in terms of equation

3.1, where the function $\Delta(t_0, \mathbf{x})$ becomes a vector $\mathbf{\Delta}$ at each t_0. The linear hyperbolic offset-dependence dictates the moveout operator $\mathbf{X}$ applied to the k^{th}-trace,

$$\mathbf{X}_k = \left(\, x_{1i}^2 \quad x_{2j}^2 \quad 2x_{1i}x_{2j} \, \right)_k , \tag{3.6}$$

where indexes k, i, and j are related by the indexing scheme described in Chapter 2. W_{11}, W_{22}, and W_{12} comprise the now three-parameter model vector $\mathbf{m}$,

$$\mathbf{m} = \begin{pmatrix} W_{11} \\ W_{22} \\ W_{12} \end{pmatrix} . \tag{3.7}$$

This notation describes exactly the same linear system as equations 2.10-2.14, but the difference between time-warping and velocity-independent NMO lies in how $\mathbf{\Delta}$ is extracted. I have rewritten the system here in terms of time-warping notation to emphasize that the three-parameter elliptical-hyperbolic surface is just a special case of moveout model, chosen *after* $\mathbf{\Delta}$ is extracted.

The volume in Figure 3.1(a) is a synthetic 3D CMP gather in which seven events were modeled with elliptical-hyperbolic moveout. Each event has a different orientation of its principal moveout axes. I applied the time-warping procedure as described above, which yields an estimate of $\mathbf{\Delta}$. I then used a linear least-squares solver with equations 3.1, 3.6, and 3.7 to obtain the three elements of $\mathbf{W}(t_0)$. The results of this procedure are shown in Figures 3.3(a)-3.3(c). For the elliptical-hyperbolic model of azimuthal anisotropy, three parameters have easily been recovered from the overdetermined system.

Although challenging for semblance-based azimuthal analysis, the synthetic example in Figure 3.1(a) is trivial for time-warping. So I next apply time-warping with azimuthally anisotropic

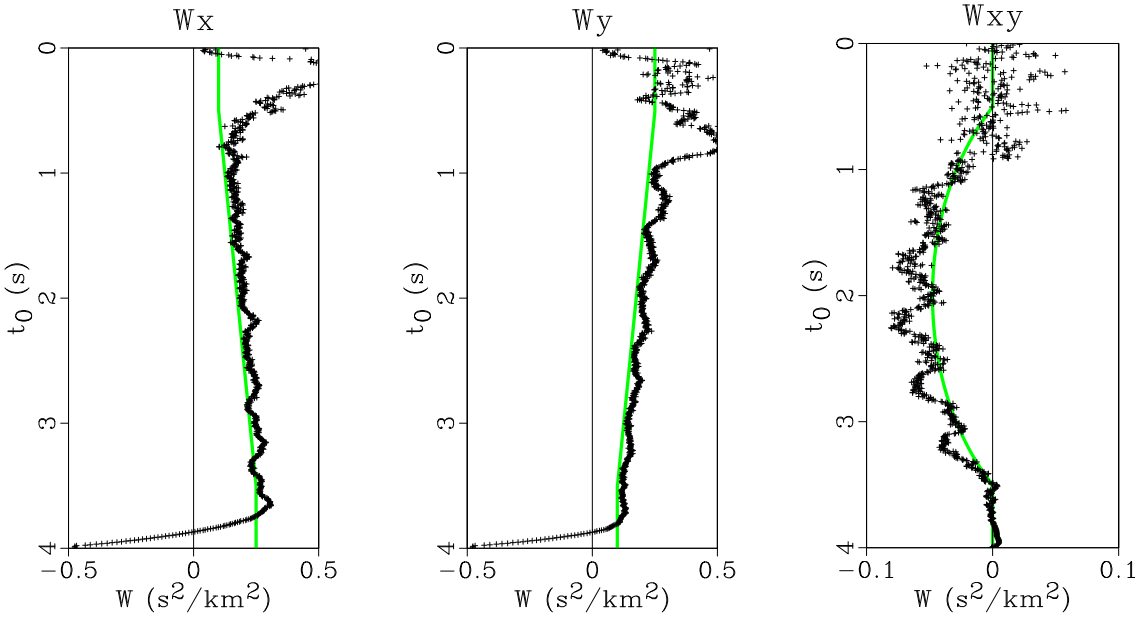

(a) (b) (c)

Figure 3.3: Least-squares fitting results for elliptically anisotropic moveout parameters. Solid line shows exact model parameters. These three values comprise the 2×2 slowness matrix, $\mathbf{W}(t_0)$, which can be used following Grechka and Tsvankin (1998) to directly determine principal moveout directions and moveout velocity as a function of azimuth. chapter-timewarp/../timewarp/elliptical Wxcompare,Wycompare,Wxycompare

parameter fitting to the Durham Ranch field data set from northwest Colorado, U.S.A.. This data set was provided by GXT/ION to help test the performance of the time-warping method. Details about geologic setting, and the acquisition and processing of this data set are provided by Schapper et al. (2009). I was given a single 2D line of 3D gathers—each of which is a pre-stack time migrated CMP gather where an azimuthally-variable NMO correction has been removed by GXT. This provided a clean, realistic data set, with a known amount of azimuthal anisotropy. My goal then, was to measure the velocity and anisotropy parameters of the removed NMO correction, and ultimately compare them with the GXT model.

The left side of Figure 3.4 shows a typical Durham Ranch CMP gather. Because this data set was migrated using offset-vector-tile binning (Cary, 1999; Vermeer, 1999; Schapper et al., 2009), it has the benefit of being regularly sampled in x_1-x_2—each gather in the data set is about 16×16 traces, which are evenly spaced in the inline and crossline directions. This allows straightforward application of time-warping, starting with 3D slope estimation, also shown for a typical gather Figure 3.4. The volumetric slopes are used in predictive painting, and the result is used to design a warping filter. The performance of the warping filter is judged by how well it flattens reflection events. A satisfactory result for most events is seen in the right side of Figure 3.4.

Like conventional velocity analysis methods, time-warping should be subjected to manual quality control (QC) steps. Time-warping offers several opportunities for QC. First, slope estimates should be inspected for their consistency with qualitative expectations. Slope estimation is not only the most computationally expensive part of time-warping, it is also the step which most influences predictive painting, and subsequently warping and parameter estimation. It is therefore worth spending time to get the PWD filter parameters right for one or more representative gathers, which is fortunately an intuitive procedure. In the Durham Ranch case, I first tested the entire

time-warping flow on a single representative gather. Once I was satisfied with the qualitative appearance of the slope estimates, I examined the predictive painting and warping performance. This second opportunity for QC can be taken by overlaying predictive painting contours on the input data, or by examining event flatness after warping. Both painting and warping are more influenced by the slope estimates than their own regularization parameters, so in practice, if their results are unsatisfactory, the PWD parameters should be adjusted first, before fine-tuning the painting and warping parameters. Once slope estimates, painting results, and event flatness are all satisfactory, I apply the warping filter to the input time-attribute volume and fit the output with velocity parameters. Finally, once a geophysically reasonable stacking velocity profile emerges from the test gather, I apply the flow to the entire data set, and adjust parameters on other CMP gathers locally if necessary.

The results of applying time-warping to the entire Durham Ranch data set are shown in Figures 3.5 through 3.9, including the least-squares error in the best-fit traveltime surfaces. The parameters displayed in these images are the percent anisotropy ϕ, the slow azimuth β, and the fast and slow velocities, which were converted from the best-fit effective slowness model, $\mathbf{W}$ following equations 1.8-1.11. It is important to remember when interpreting these results, that these are effective parameters, not interval parameters. The estimated stacking velocities associated with each reflector are time-weighted averages of the velocities in all layers in the overburden. If one assumes the estimated stacking velocities are close to the near-offset NMO velocities, then they are close to the RMS parameters, and therefore can be related to interval velocities via Dix differentiation (Dix, 1955; Dobrin and Savit, 1988). In the azimuthally anisotropic case, we can use the technique of generalized Dix inversion (Grechka et al., 1999) to first convert effective slowness matrices $\mathbf{W}(t_0)$ to interval slowness matrices $\mathbf{W}_{int(t_0)}$, and then subsequently convert the interval matrices to intuitive

parameters following equations 1.8-1.11.

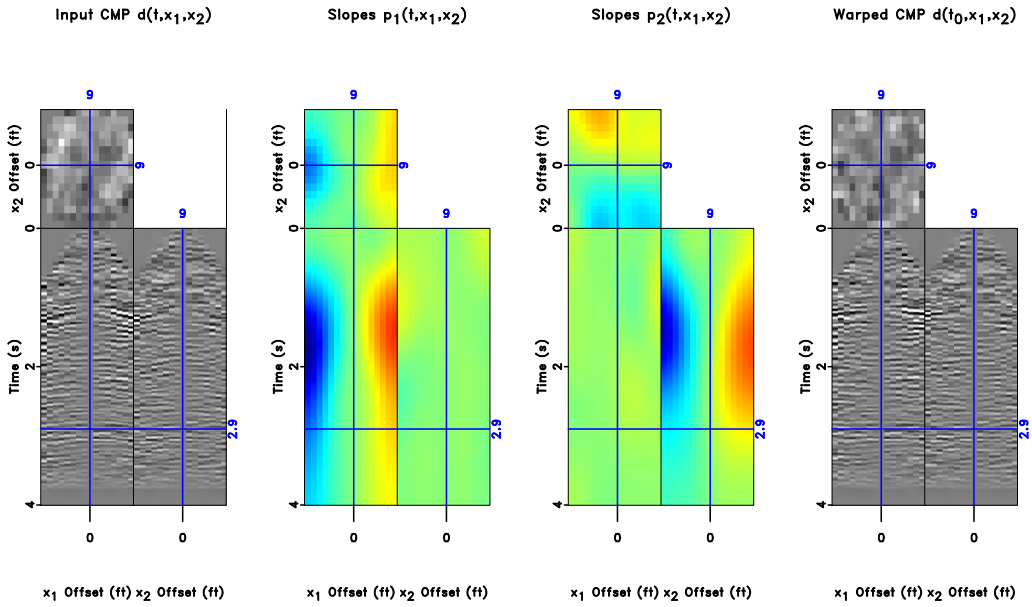

Figure 3.4: Typical CMP gather and slope fields from Durham Ranch data set. The right image shows the same gather after warping. chapter-timewarp/../durham/test warp3

The images in Figures 3.10 through 3.13 show the results of applying generalized Dix inversion to the effective sections. Generalized Dix inversion is a differentiation that is most stable when applied as a discrete difference operator over relatively large steps in time (Grechka et al., 1999). Since time-warping outputs velocity estimates which are relatively smooth due to the influence of regularized slope estimation, I found it was fairly stable to apply generalized Dix inversion on the Durham Ranch data set as a vertical sample-by-sample differentiation operator,

$$\mathbf{W}_{int,i}^{-1} = \frac{(t_0)_i \mathbf{W}_i^{-1} - (t_0)_{i-1} \mathbf{W}_{i-1}^{-1}}{(t_0)_i - (t_0)_{i-1}}, \tag{3.8}$$

where i indicates the current time sample index and $i-1$ is the previous time index. The results

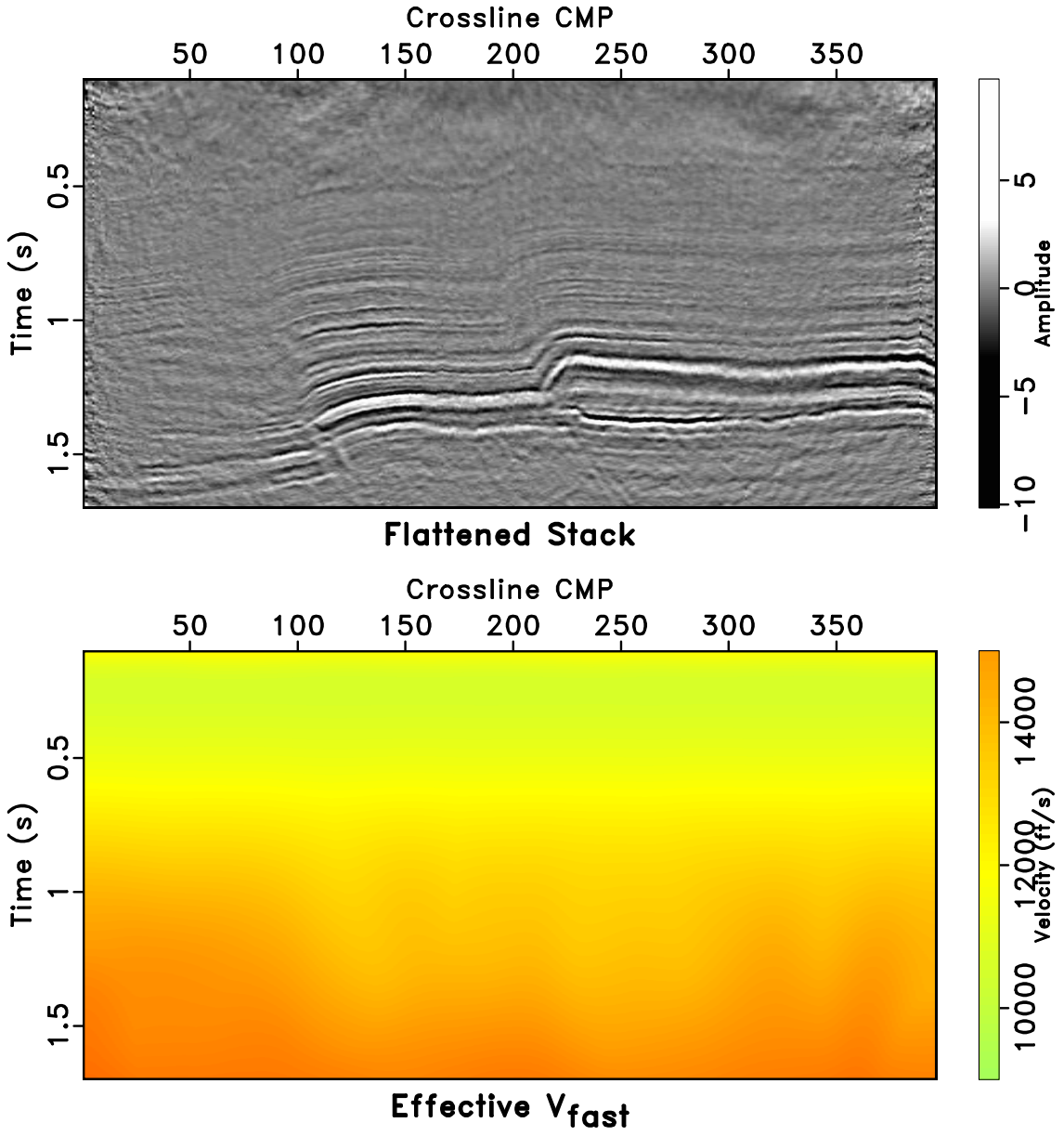

Figure 3.5: Effective fast velocity estimates from time-warping on Durham Ranch migrated CMP gathers. The top shows the stack image using warped gathers for reference. chapter-timewarp/../durham/fulltest V-fast

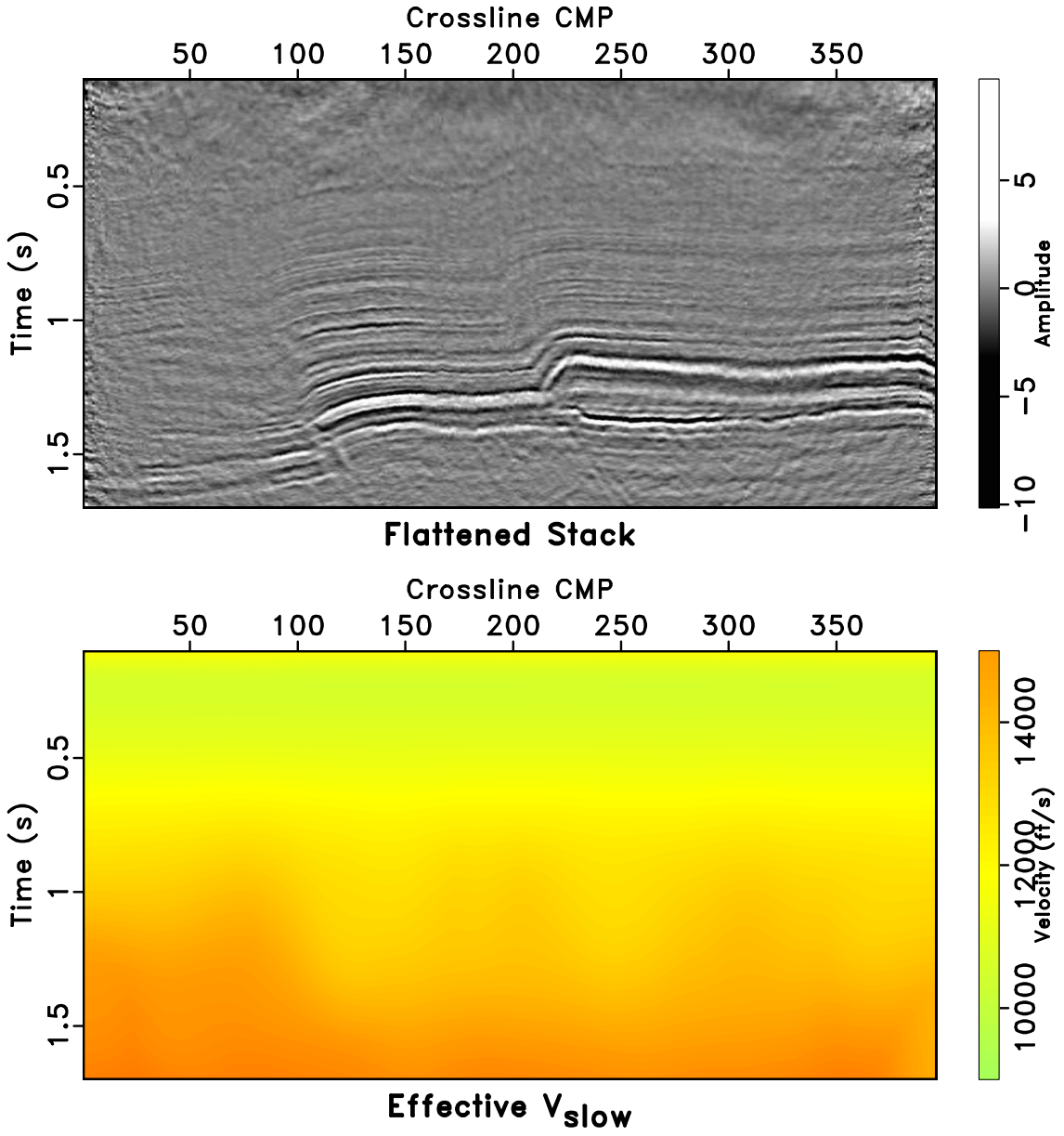

Figure 3.6: Effective slow velocity estimates from time-warping on Durham Ranch migrated CMP gathers. The top shows the stack image using warped gathers for reference. chapter-timewarp/../durham/fulltest V-slow

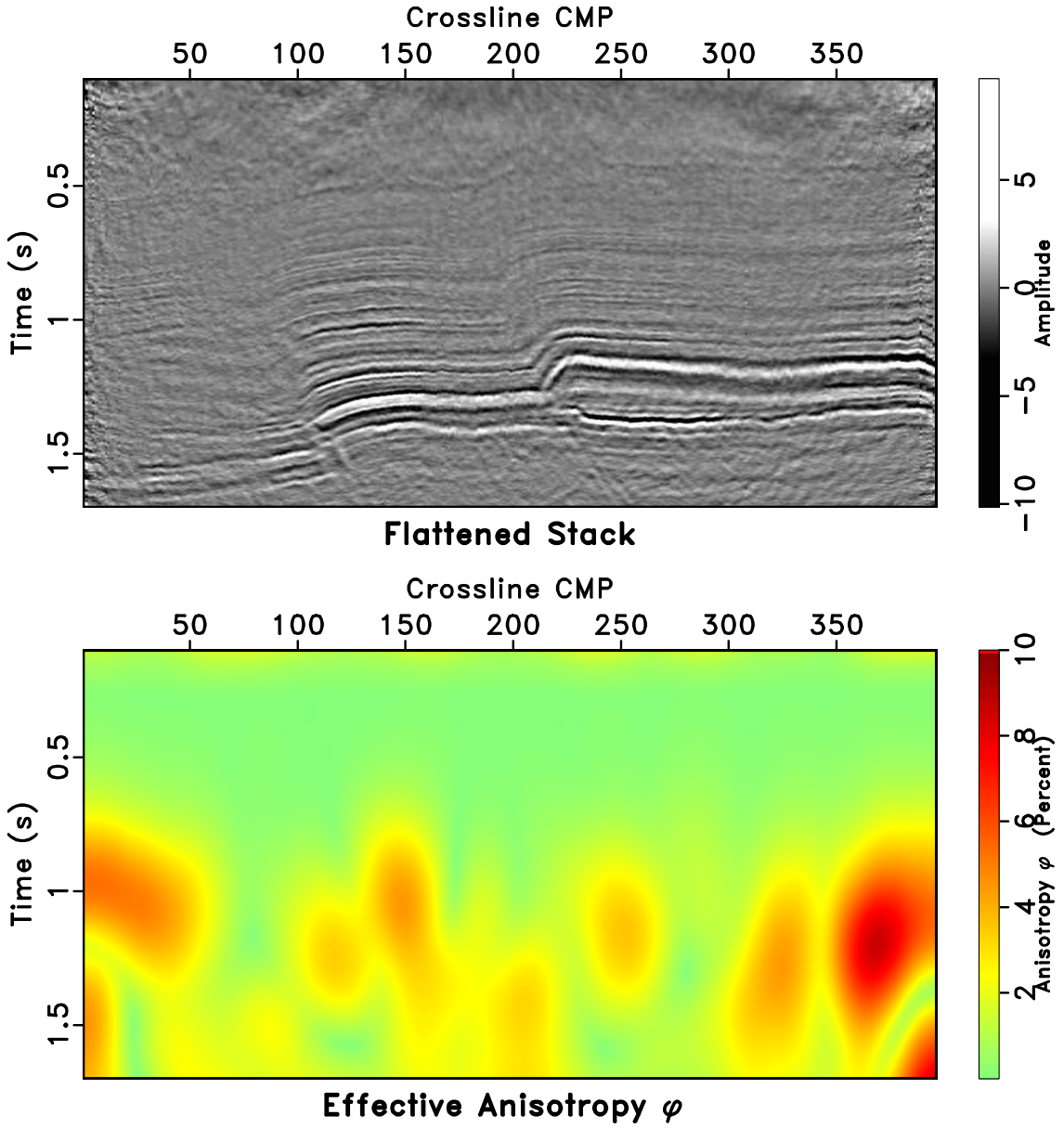

Figure 3.7: Effective anisotropy estimates from time-warping on Durham Ranch migrated CMP gathers. The top shows the stack image using warped gathers for reference. chapter-timewarp/../durham/fulltest aniso-effective

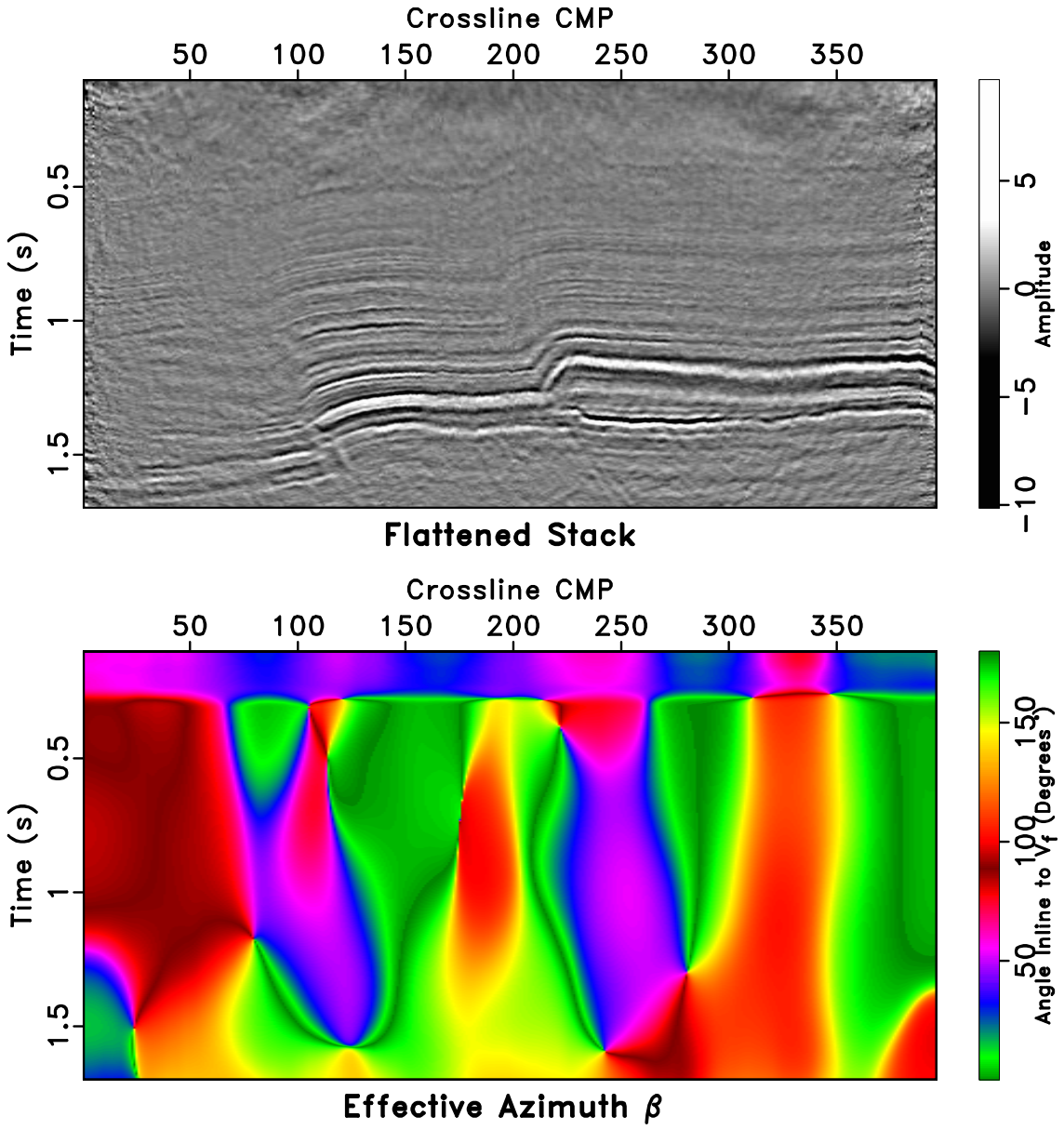

Figure 3.8: Effective β estimates from time-warping on Durham Ranch migrated CMP gathers. The top shows the stack image using warped gathers for reference. chapter-timewarp/../durham/fulltest beta-effective

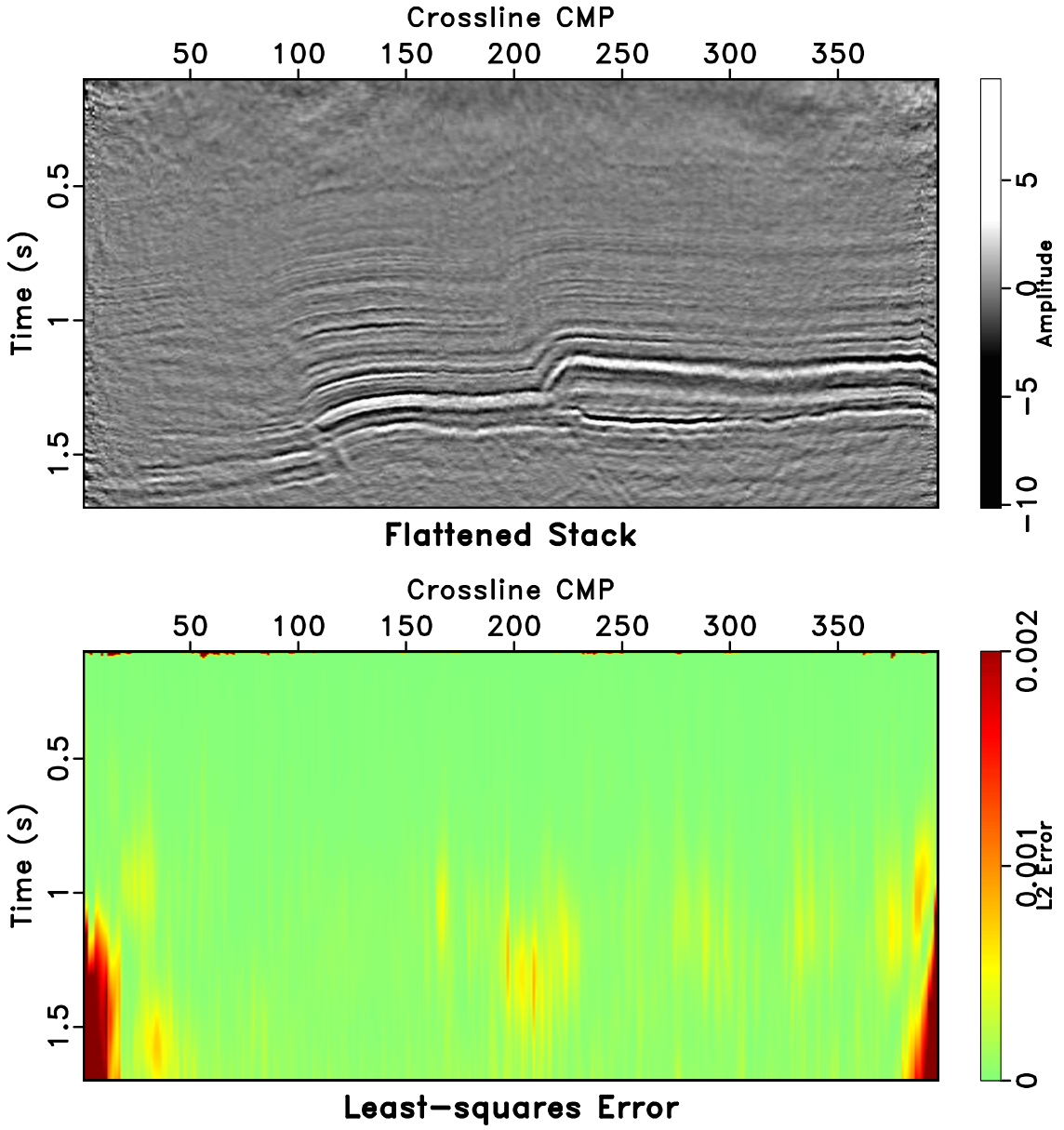

Figure 3.9: L2-norm fitting error ($|\mathbf{\Delta}_{fit} - \mathbf{\Delta}_{obs}|^2$ summed over offset) from time-warping on Durham Ranch migrated CMP gathers. The top shows the stack image using warped gathers for reference. chapter-timewarp/../durham/fulltest Error

in Figures 3.10 through 3.13 are the actual differentiation results with a small amount of post-inversion smoothing. The geologic interpretation of the results is still somewhat uncertain without comparison to borehole, core, or engineering data, but it is encouraging to see how changes in the interval parameter estimates tend to correlate with the imaged structures. There are several pronounced parameter contrasts at event boundaries, and the lateral distribution of the parameter estimates seems to be related to the fault block structures. One of the theoretical benefits of offset-vector-tile migration is that it allows azimuthal analysis post-migration, which helps mitigate the influence of structure (in terms of causing apparent anisotropy) on parameter estimates. The results I have obtained here clearly correlate with the subsurface structure, which can be explained either as residual apparent anisotropy not fully mitigated by migration, or by true anisotropy under geologic structural controls.

To conclude this example, I take the three-parameter velocity model $\mathbf{W}(t_0)$ estimated by time-warping at Durham Ranch, and use it to apply a physical NMO correction based on equation 1.6. The final azimuthally-anisotropic NMO-corrected stack is shown in Figure 3.14.

Spiral-sorting

The Durham Ranch data set is nearly ideal for multiazimuth parameter estimation, mainly because the gathers have been migrated using an offset-vector tile binning scheme which preserves azimuth and offset information. Post-migration gathers are generally cleaner, more regularized, and better sampled in a balance between azimuth and offset than their pre-migration counterparts. Further, since migration inherently adjusts the time-domain structural positioning of each event, the influence of heterogeneity is reduced, making any estimated parameters more likely related to true azimuthal anisotropy. However, post-migration analysis is not usually the case in practice unless

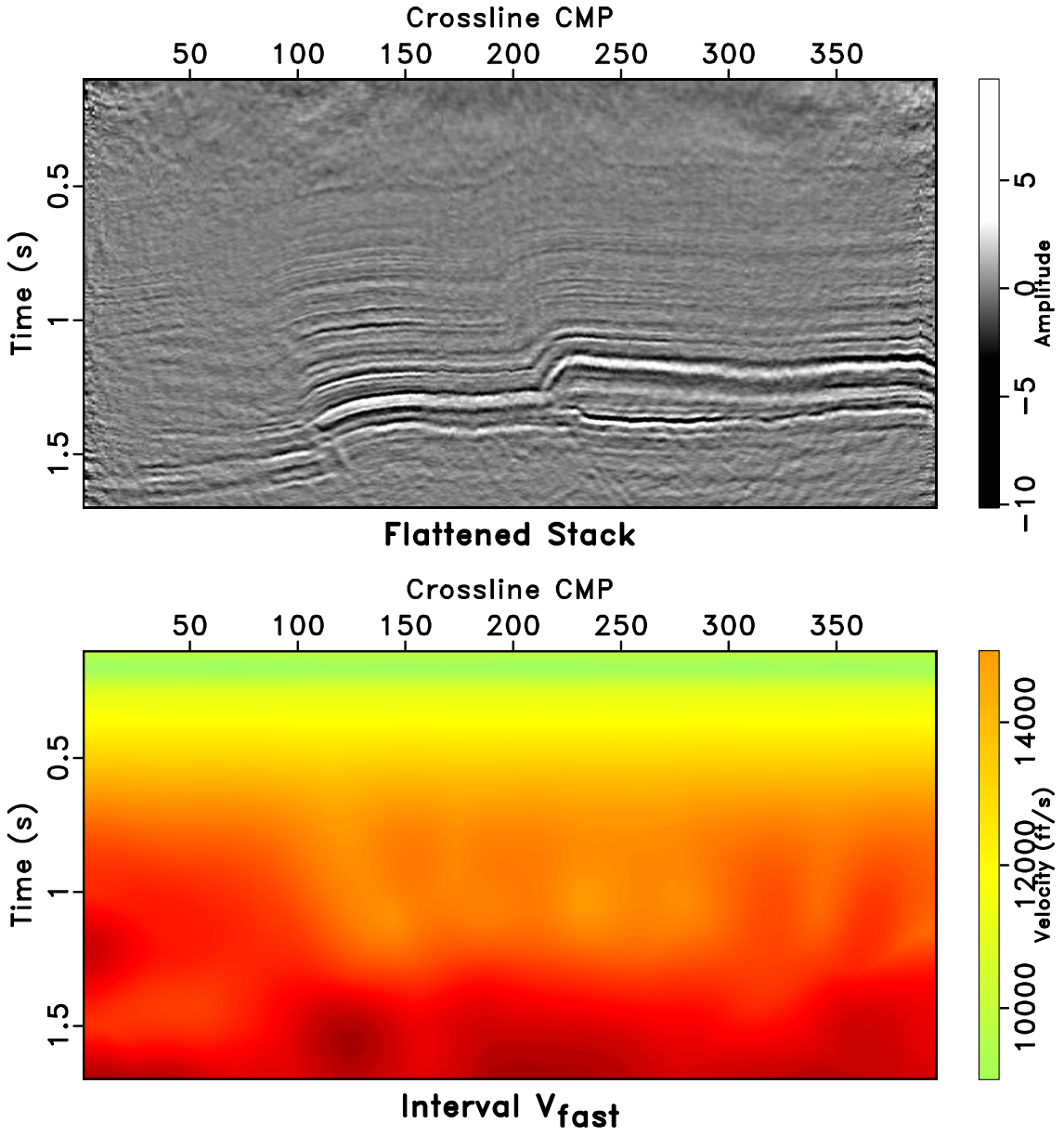

Figure 3.10: Interval fast velocity estimates from time-warping and generalized Dix inversion. The top shows the stack image using warped gathers for reference. chapter-timewarp/../durham/fulltest Vint-fast

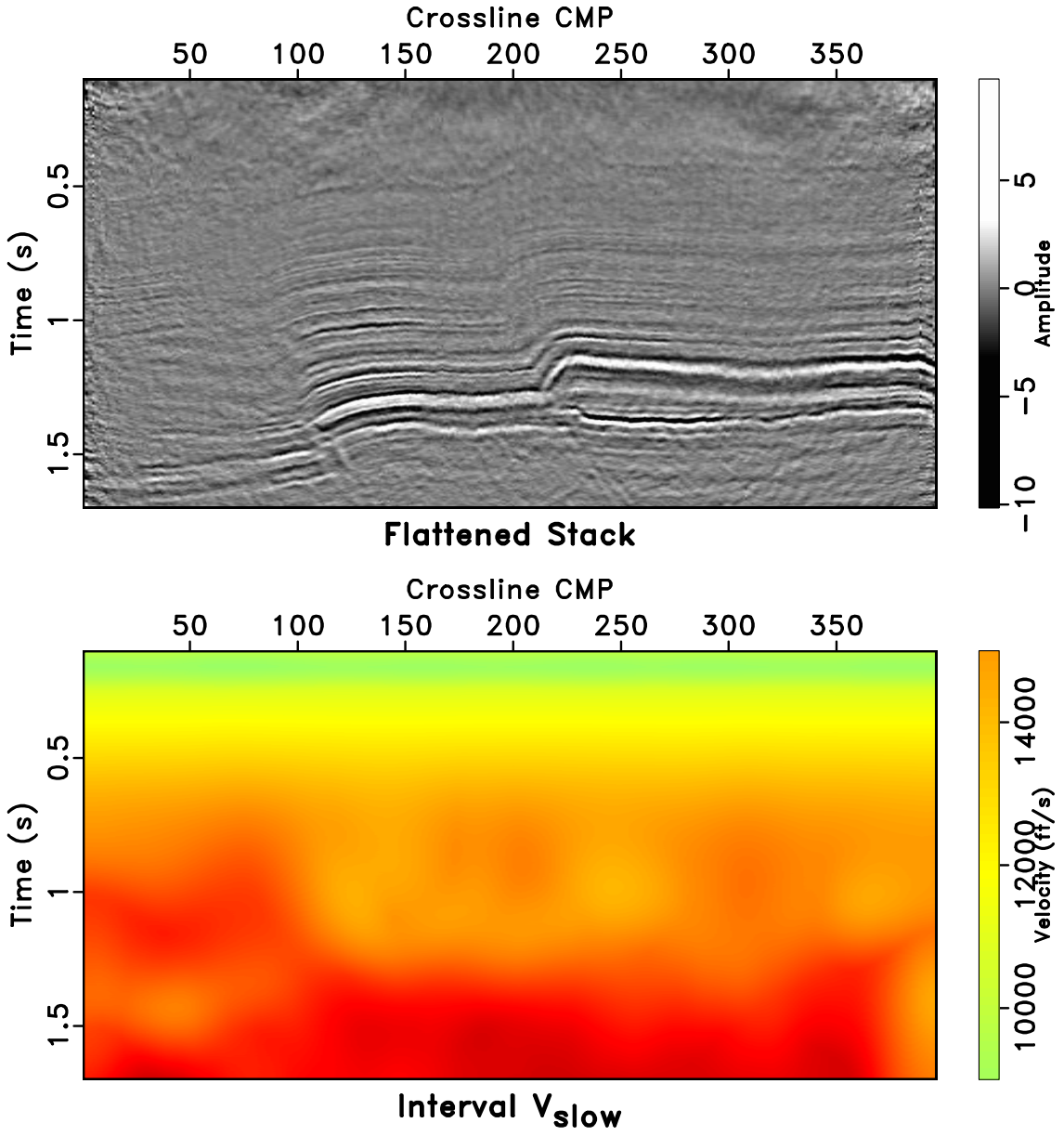

Figure 3.11: Interval slow velocity estimates from time-warping and generalized Dix inversion. The top shows the stack image using warped gathers for reference. chapter-timewarp/../durham/fulltest Vint-slow

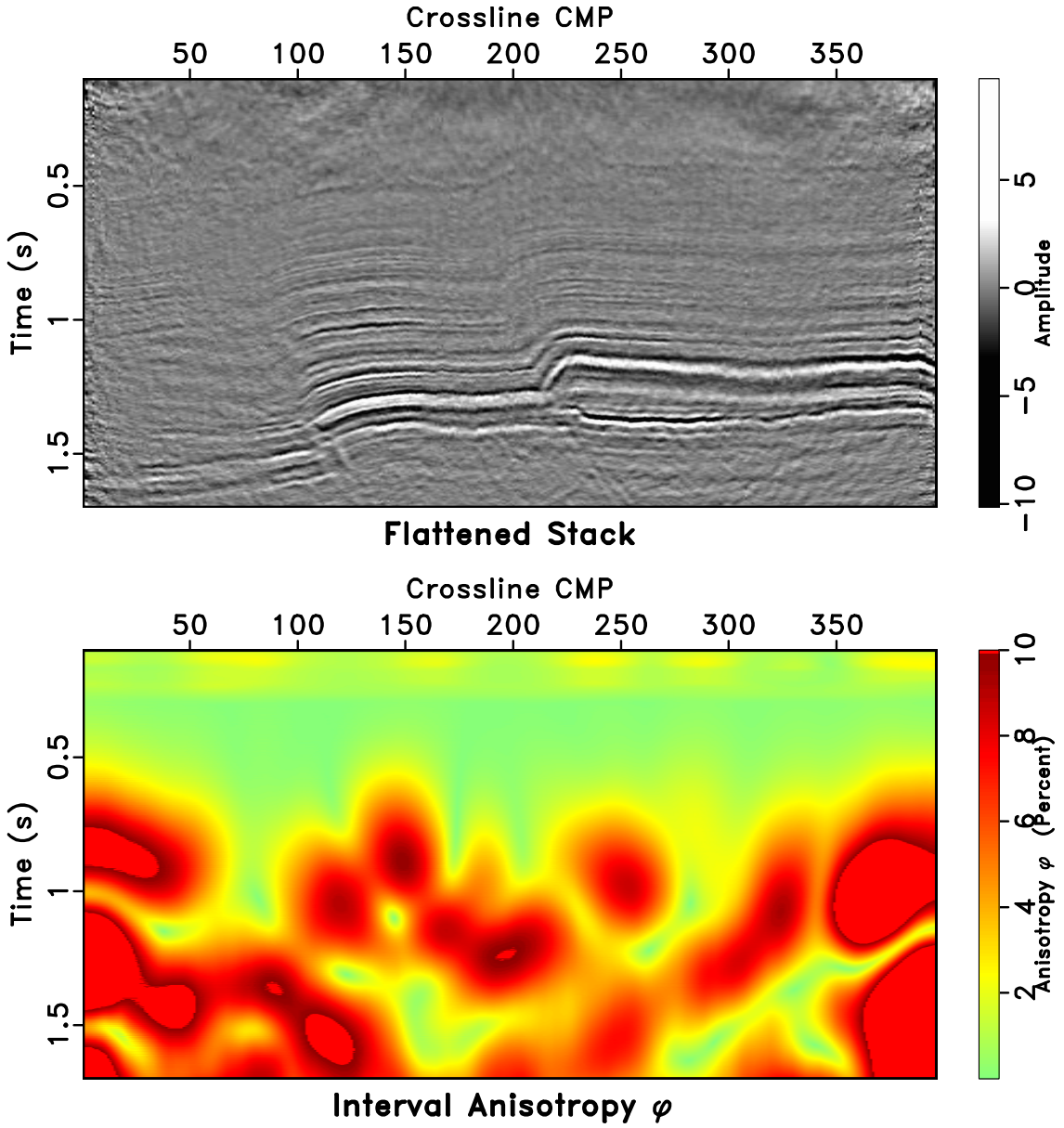

Figure 3.12: Interval anisotropy estimates from time-warping and generalized Dix inversion overlaid on wiggle-trace image. The top shows the stack image using warped gathers for reference. chapter-timewarp/../durham/fulltest anisotropyi

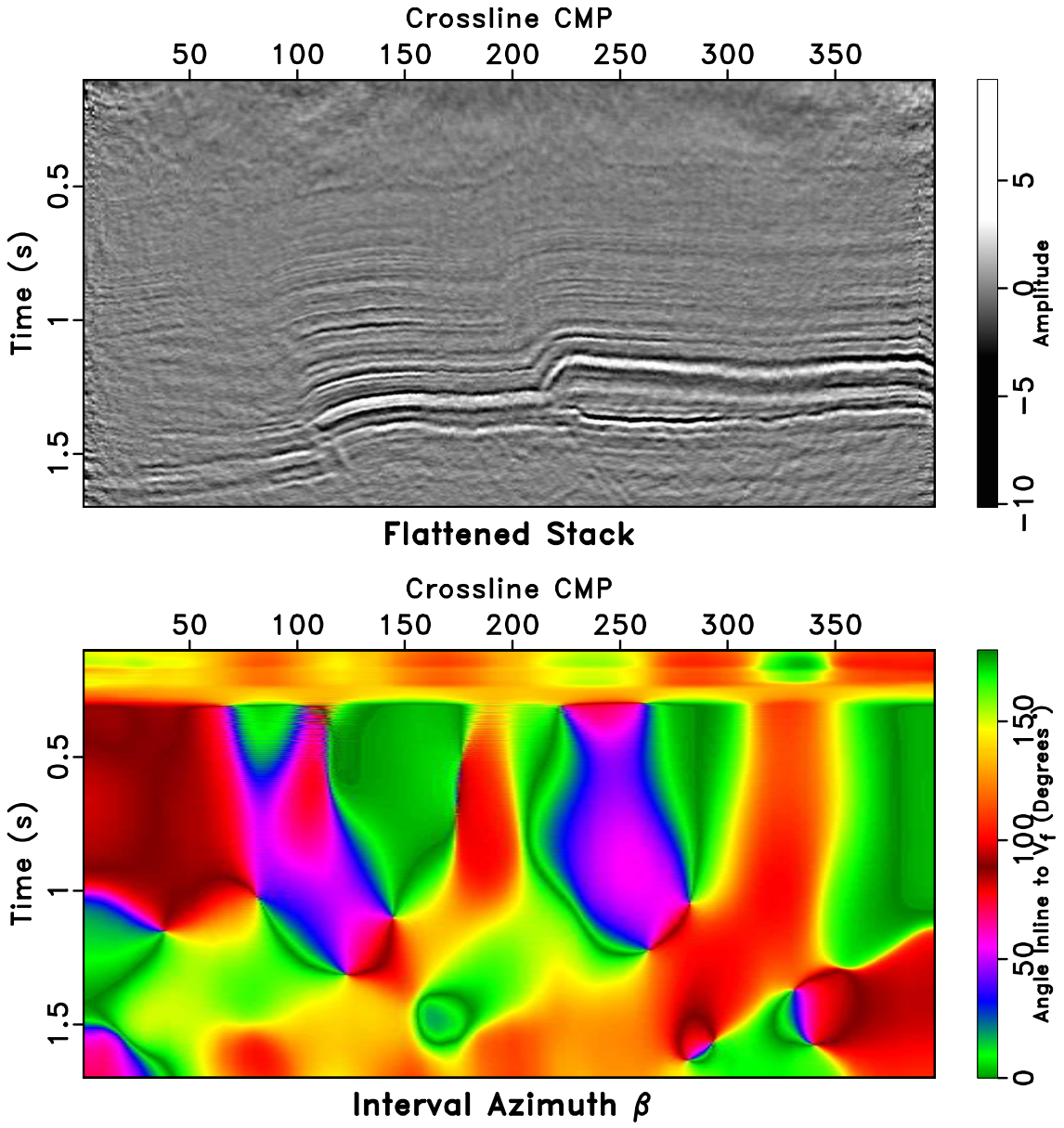

Figure 3.13: Interval β estimates from time-warping and generalized Dix inversion overlaid on wiggle-trace image. The top shows the stack image using warped gathers for reference. chapter-timewarp/../durham/fulltest betai

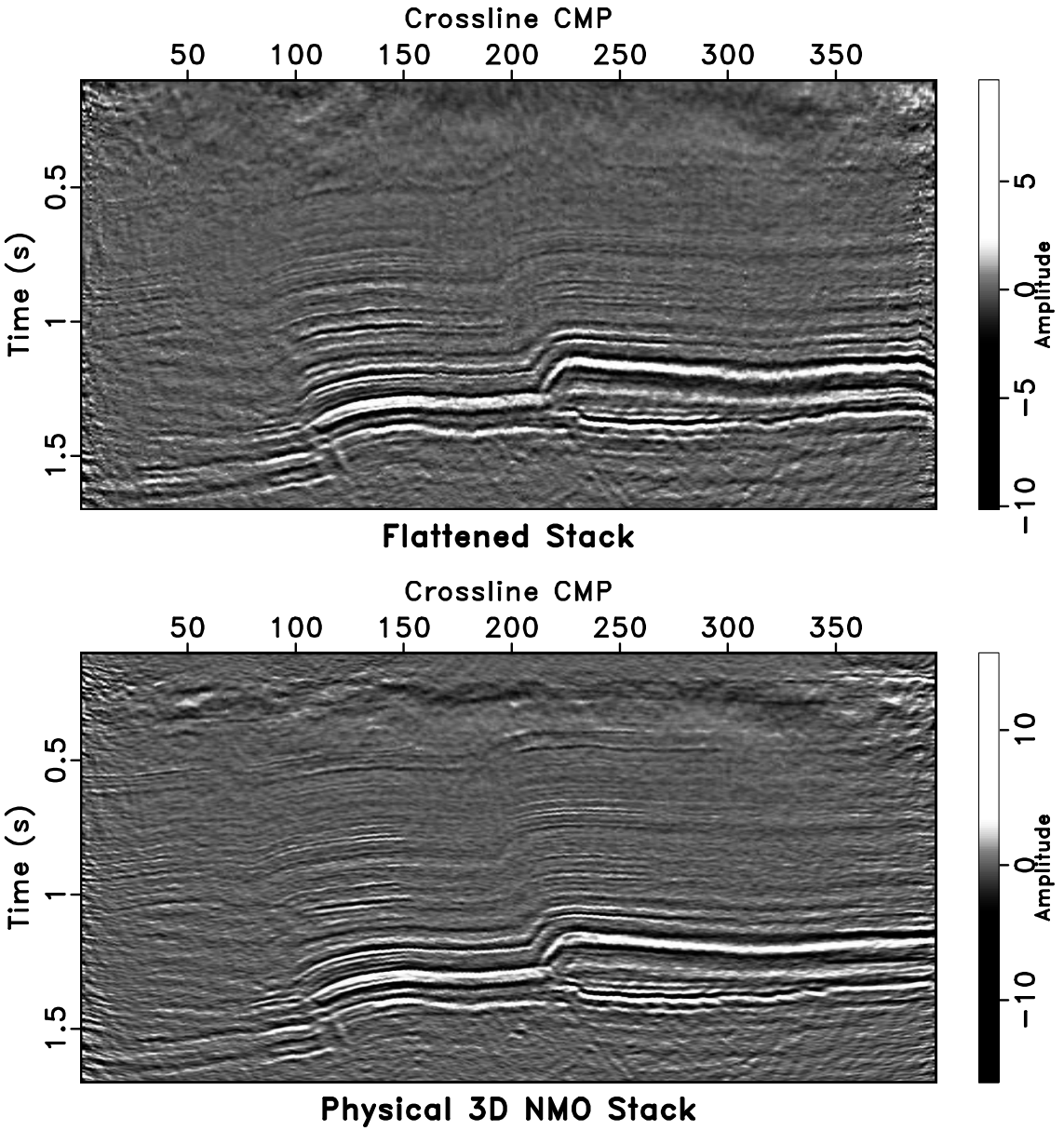

Figure 3.14: Durham Ranch post-migration stacks from time-warping. Top: Stack created by summing non-physically warped CMP gathers over offset. Bottom: Stack created by applying physical elliptical-hyperbolic NMO using the velocity model parameters found by time-warping. chapter-timewarp/../durham/fulltest physical-nmo

azimuthal analysis is a primary objective. Trials of the time-warping method on other field data sets (all pre-migration) revealed practical limitations related to the realities of seismic data acquisition. First, field gathers are usually not regularly spaced in both inline and crossline directions. Second, typical multiazimuth gathers do not have high fold in all azimuths—even in the 256-fold case of the Durham Ranch gathers (relatively high for modern land surveys), there are at most 16 traces in a given azimuth. For these reasons, it is not always reasonable to try and arrange traces within multiazimuth gathers into the 3D orthogonal x_1-x_2 offset geometry discussed in all cases above. If CMP traces are not arranged in this orthogonal grid, however, then local slope estimates cannot be directly related to hyperbolic velocity or moveout, as required by velocity-independent NMO from Chapter 2.

Unlike velocity-independent NMO, I have claimed that time-warping does not assume a moveout model before hand; it works based on aligning events between neighboring traces, regardless of the physical or spatial relations between them. Therefore, time-warping can be applied to the traces of a CMP gather, no matter how they are arranged, as long as predictive painting can follow the events from trace-to-trace. In this section, I explore a few options for reorganizing CMP traces into gather formats which have advantages over the orthogonal offset grid. These organizations are 2D, but I will still fit them with the 3D elliptical-hyperbolic model.

A reasonable first attempt to exploit the flexibility of time-warping is to completely bypass arranging a given CMP gather, and keep its traces ordered based solely on absolute value of offset. Offset-sorting is typically how traces are arranged when put through a semblance-scan because it clearly emphasizes the offset-dependence of reflection moveout. Figure 3.15a shows an offset-sorted Durham Ranch CMP gather. When compared to the same gather gridded in 3D orthogonal offset, seen in Figure 3.4, the events are clearly more visible from trace-to-trace, which suggests

that 2D predictive painting will likely work well on the offset-sorted version. This leads to another practical advantage of offset-sorting, in that by performing slope-estimation only along the offset direction, neighboring gathers can be computationally juxtaposed along the third axis of the input data volume, where they can be used to enforce shaping regularization during slope estimation (the first and second axes being time and offset, respectively). Event visibility itself is also useful for warping performance QC, so offset-sorted gathers are an attractive option for time-warping analysis. However, from trace-to-trace in the offset-sorted format, the events frequently have discontinuous moveout, making slope estimation still difficult. Many of these discontinuities are easily removed by first applying a smooth isotropic NMO correction to the gathers, and estimating slopes (and afterward performing time-warping) as an anisotropic residual process. The results of estimating slopes for the gather in Figure 3.15a (after an initial isotropic NMO correction) are shown in Figure 3.15b.

Figure 3.15c-d show the results of applying time-warping to the offset-sorted gather. The resulting fast and slow velocity profiles fit to the offset-sorted gather are very stable, but there is almost no difference between them. This means that azimuth β estimates are typically very unstable, which suggest that a weakness of offset-sorting is an inability to reliably detect azimuthal variations in moveout velocity. This is not surprising when we consider the most important step of time-warping: slope estimation. The PWD filter tool in Madagascar (the software package used in this research) allows shaping regularization to be applied along three axes. We gain the advantage of gather-to-gather regularization by sorting physically 3D gathers into a 2D organization such as offset sorting. However, regularization along the offset axis is still necessary to ensure robust slope estimates from trace-to-trace within each gather. The more smoothing enforced by regularization, the more robust the slope estimates, which is critical for application to field data. If no smoothing

is enforced, then slopes are independently estimated from sample to sample throughout the gather, which might be ideal for perfectly clean data, but is unstable for most field data. With this trade-off in mind, a small amount of regularization cannot be avoided, which means that subtle trace-to-trace shifts will be smoothed-through by the PWD filters.

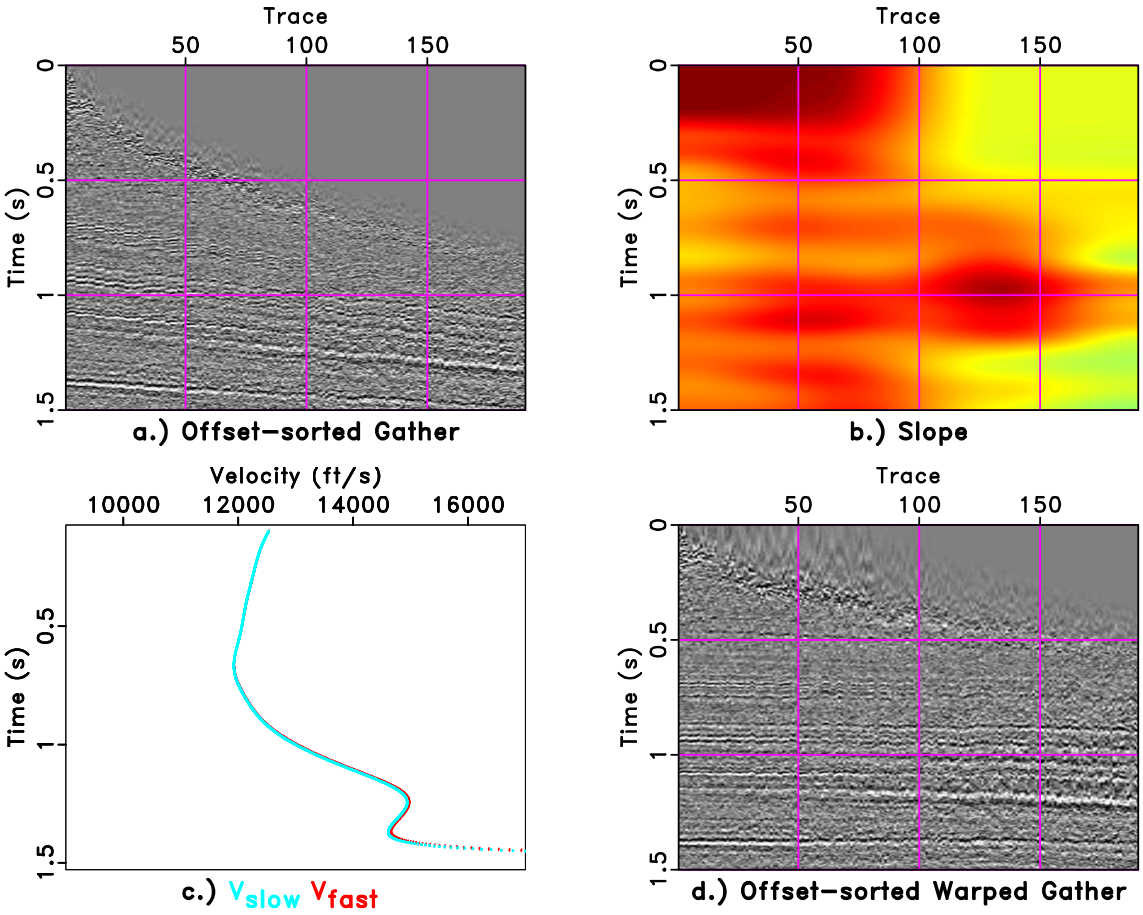

Figure 3.15: Offset-sorted gather example. a.) Same gather as seen in Figure 3.4, but traces are sorted by absolute value of offset. b.) Slope field measured on the offset-sorted gather after an initial isotropic NMO correction. c.) Fast and slow velocity estimates overlaid on the same plot. d.) Offset-sorted gather after warping. chapter-timewarp/../durham/offset offset-test

The overall event moveout is easily detected on an offset-sorted gather by smooth slope

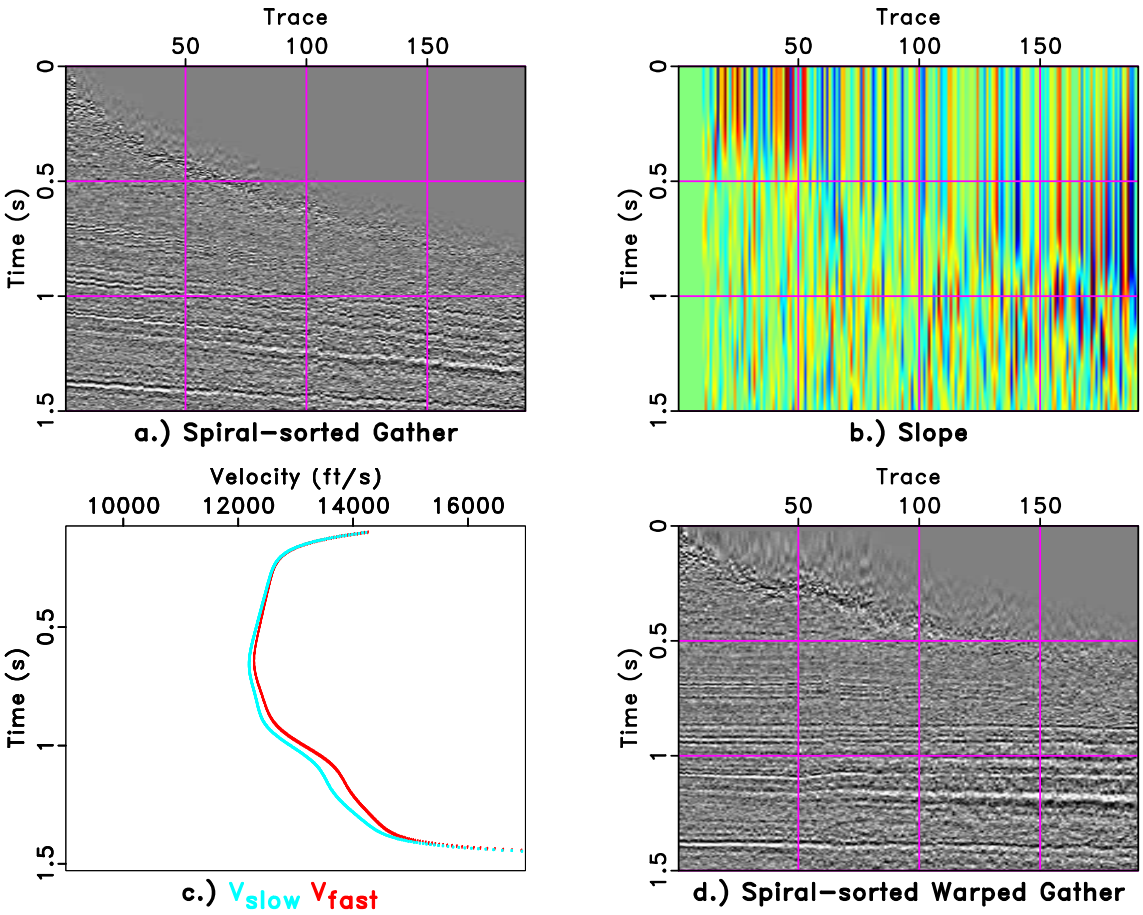

Figure 3.16: Spiral-sorted gather example. a.) Same gather as seen in Figures 3.4 and 3.15, but traces are now sorted by spiral indexing scheme. b.) Slope field measured on the offset-sorted gather. c.) Fast and slow velocity estimates overlaid on the same plot. d.) Spiral-sorted gather after warping. Notice the overall flattening performance is similar to the offset-sorting results in Figure 3.15, but the trace-to-trace continuity has improved. chapter-timewarp/../durham/spiral spiral-test

estimates, but neighboring traces in this format may be from completely random azimuths, even in most synthetic cases. To see this, I have drawn a diagram in Figure 3.17(a) showing a map-view of trace positions in an ideal 10×10 3D CMP gather. Each trace is placed in a bin on the orthogonal x_1-x_2 offset grid. I have numbered each trace location by its offset magnitude ($\sqrt{x_1^2 + x_2^2}$)—lower numbers corresponding to smaller offsets, and equal numbers corresponding to equal offsets. It is easy to see from this diagram that if the traces are perfectly-spaced (located at the exact center of each bin), then 2D sorting by absolute value of offset is non-unique. In most field gathers, there will be variations in azimuths among neighboring traces, which will on average, be random. For example, if we look at say, all traces labeled 9 on the diagram, and where they end up in a purely offset-based 2D sorting, they will be neighbors, but their azimuths will likely be sequenced randomly. This azimuthal effect is well-known, and often referred to as "trace jitter" (Jones, 2010). Since trace jitter is difficult to robustly capture with PWD filters, it explains why offset-sorted time-warping is reasonable for finding the average hyperbolic velocity, but at the same time cannot "see" azimuthal moveout variations.

We can summarize the problem of trace jitter as the result of traces being generally well-sorted, but because of their random azimuths, neighboring traces have no guarantee of spatial proximity. Although time-warping conceptually works on an arbitrary sorting, we see that the sorting of traces has practical importance in slope-estimation. We can then logically devise an alternative 2D sorting which has the QC benefits of offset-sorted gathers, yet accommodates the capture of azimuthal information. The ideal sort will vary smoothly in both offset and azimuth, while maintaining a minimum physical spacing between neighboring traces. By assuming that a given field 3D CMP gather is spatially gridded similar to Figure 3.17(a), we can reorganize it into a well-known path that meets our ideal criteria: the spiral. Re-indexing the grid in Figure 3.17(a)

as an integer spiral is shown in Figure 3.17(b)* Under this spiral-sorted order, each trace in a 3D CMP gather has an unique index determining its position in a 2D sort, that smoothly varies in both offset and azimuth.

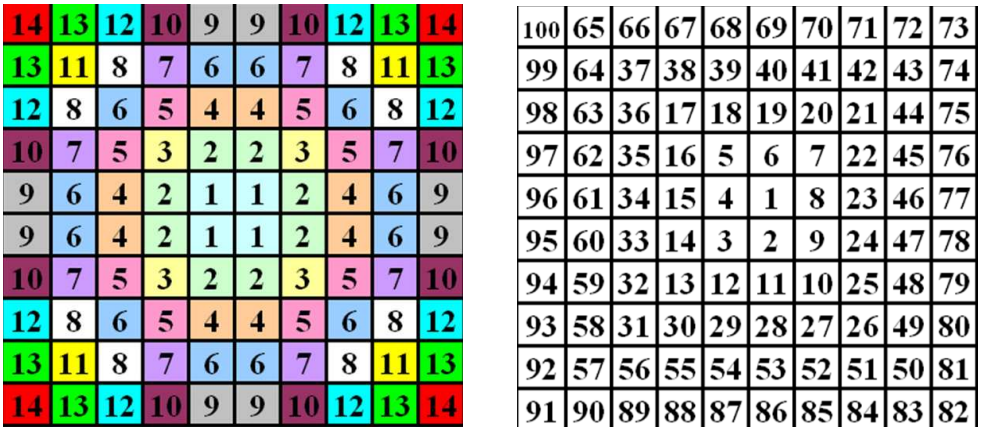

14	13	12	10	9	9	10	12	13	14
13	11	8	7	6	6	7	8	11	13
12	8	6	5	4	4	5	6	8	12
10	7	5	3	2	2	3	5	7	10
9	6	4	2	1	1	2	4	6	9
9	6	4	2	1	1	2	4	6	9
10	7	5	3	2	2	3	5	7	10
12	8	6	5	4	4	5	6	8	12
13	11	8	7	6	6	7	8	11	13
14	13	12	10	9	9	10	12	13	14

(a)

100	65	66	67	68	69	70	71	72	73
99	64	37	38	39	40	41	42	43	74
98	63	36	17	18	19	20	21	44	75
97	62	35	16	5	6	7	22	45	76
96	61	34	15	4	1	8	23	46	77
95	60	33	14	3	2	9	24	47	78
94	59	32	13	12	11	10	25	48	79
93	58	31	30	29	28	27	26	49	80
92	57	56	55	54	53	52	51	50	81
91	90	89	88	87	86	85	84	83	82

(b)

Figure 3.17: CMP trace sorting diagrams. These are plan-view diagrams where the midpoint is conceptually at the center of each, and bins represent the physical orthogonal offset-grid trace locations. The index in each bin dictates its order in a particular sort. Left: Offset-sorted. Sequentially or equally-numbered bins indicate traces which will be neighbors on an offset-sorted gather, despite their azimuthal variations. Right: Spiral-sorted. Now each trace has an unique index, and neighbors are similar in both offset and azimuth. chapter-timewarp/. offsort-grid,spiralsort-grid

Instead of literally sorting real gathers onto a perfect integer spiral, I wrote a simple sorting code in Madagascar which sorts 3D gathers into an approximate spiral arrangement (`sfspiral`). This is necessary, because unlike the migrated Durham Ranch gathers, typical field gathers do not fit perfectly into the orthogonal-grid sorting to begin with. My code is based on the equation of an Archimedean spiral (Weisstein, 2003),

*The numbered grid in Figure3.17(b) is coincidentally a well-known mathematical diagram known as Ulam's Spiral (Stein et al., 1964). While bored during a mathematics conference, Ulam sketched this integer spiral on a napkin and started shading-in prime numbers. He noticed that the locations of prime numbers on the spiral exhibited a strong "non-randomness"! If you feel compelled to deface my dissertation and shade in the primes, notice for example, the diagonal from 91-73.

$$R = r + c\theta, \tag{3.9}$$

where R is the radius of the spiral, r is an initial rotation (by default 0), and c is an adjustable parameter to set the spiral cycle-spacing in terms of offset. My spiral-sorting code simply groups all traces that share the nearest spiral cycle, and then sorts the grouped traces by azimuth. All same-cycle groups are then re-combined according to increasing offset, resulting in a spiral-sorted gather.

The same gather shown offset-sorted in Figure 3.15a is shown after spiral-sorting in Figure 3.16a. The trace jitter has been reduced, and the corresponding slope estimates in Figure 3.16c can be dramatically refined to capture the trace-to-trace moveout as well as the overall moveout. The results shown in Figures 3.16c-d are similar to the results from the offset-sorted results, but the azimuthal variations in velocity are again resolved. In this case, the Durham Ranch gathers are clean, regularized, and well-sampled, making the 3D orthogonal grid-sorted results still better compared the spiral-sorted results. I would again like to comment though, that on other field data cases without the benefits of being post-offset-vector tile migration, spiral-sorting may provide a helpful alternative to orthogonal grid-sorting. In any case, spiral-sorting clearly demonstrates the flexibility available with time-warping, which may lead to even more unusual but purposeful data organizations in future applications.

Nonhyperbolic Moveout

Taner et al. (2005, 2007) and Blias (2007) observe that nonhyperbolic moveout can be geometrically described as an increase in moveout velocity with offset. They use a second moveout parameter, $a(t_0)$, to account for effective "moveout acceleration". Their moveout expression,

$$t(t_0, \mathbf{x}) = \sqrt{t_0^2 + \frac{|\mathbf{x}|^2}{W_0^{-1}\left(1 + a|\mathbf{x}|^2\right)}}, \tag{3.10}$$

is also easy to arrange as a linear system similar to the form 3.1,

$$\frac{|\mathbf{x}|^2}{t^2 - t_0^2} = W_0^{-1} + b|\mathbf{x}|^2, \tag{3.11}$$

if we invert the usual time-shift vector $\mathbf{\Delta}$, and scale by offset-squared. In equations 3.10 and 3.11, W_0 describes short-spread hyperbolic moveout, and $b = aW_0^{-1}$ characterizes the increase in moveout velocity with offset. In terms of time-warping, the k-th element of the data vector becomes,

$$\mathbf{\Delta}_k = \frac{|\mathbf{x}|^2}{t^2 - t_0^2}, \tag{3.12}$$

the k-th row of the operator matrix becomes,

$$\mathbf{X}_k = \begin{pmatrix} 1 & |\mathbf{x}|_k^2 \end{pmatrix}, \tag{3.13}$$

and the model vector becomes,

$$\mathbf{m} = \begin{pmatrix} W_0^{-1} \\ b \end{pmatrix}. \tag{3.14}$$

I applied the time-warping method to a single field CMP gather from the Elf data set in Figures 3.18-3.20. After these parameters are obtained by the time-warping process, I use them to apply a physical NMO flattening based on equation 3.11.

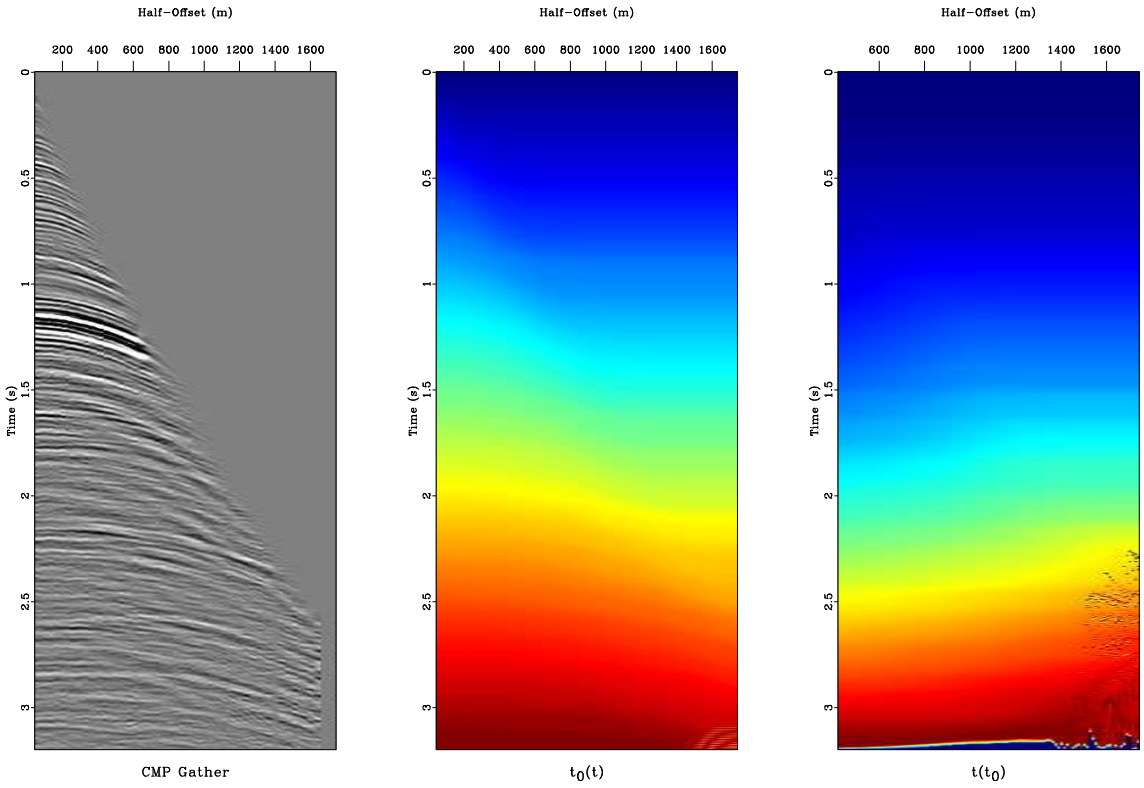

Figure 3.18: (a) Field CMP gather from Elf data set. Corresponding attribute sections (b) $t_0(t)$ and (c) $t(t_0)$. chapter-timewarp/../timewarp/elf t2

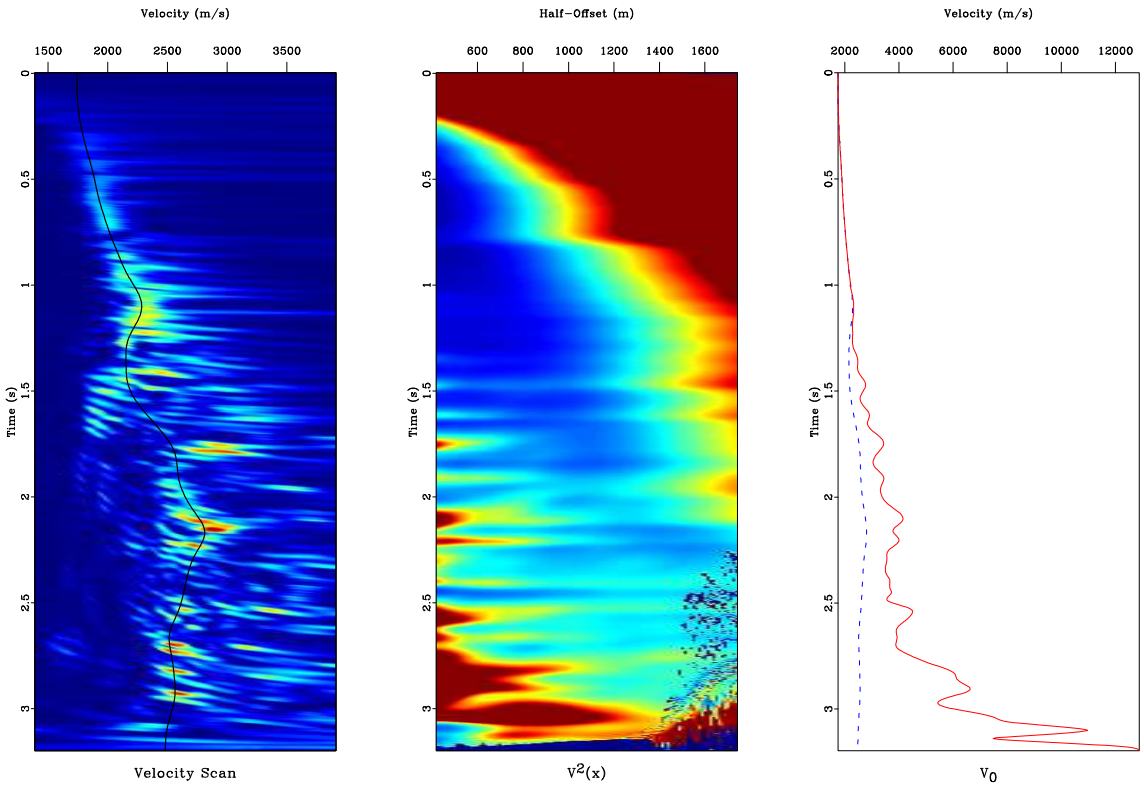

Figure 3.19: (a) Conventional velocity scan semblance panel with automatic picks. (b) $v^2(t_0, x)$ estimated from time-warping. (c) Dashed line indicates semblance scan picks next to best-fit v_0 parameter of equation (3.11). chapter-timewarp/../timewarp/elf v2

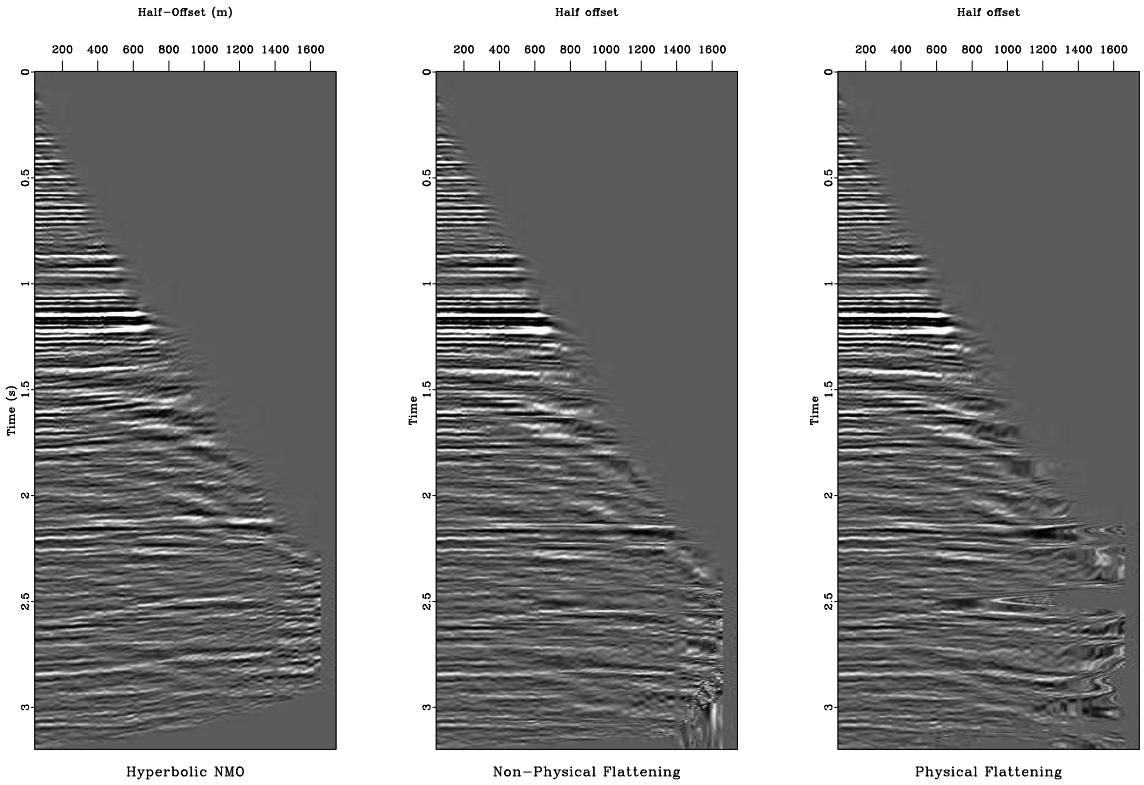

Figure 3.20: Field CMP gather flattened by (a) conventional NMO and (b) non-physical flattening. The moveout parameters v_0 and a were extracted and used in a physical NMO equation to obtain (c). chapter-timewarp/../timewarp/elf nmo3

Discussion

Predictive painting and warping can capture arbitrary surface geometries without prior moveout assumptions. The geometry information is then fit with an assumed moveout model, which can be multi-parameter at no extra computational cost. This sequence of three steps—painting, warping, and fitting—I refer to as time-warping, and propose as a powerful traveltime inversion velocity analysis approach. My method is also easily implemented in other analysis domains. I have demonstrated through several examples that time-warping is useful for characterizing moveout that varies with either azimuth or offset, corresponding to apparent azimuthal anisotropy or nonhyperbolic moveout, respectively. A straightforward extension is possible to describe azimuthally-variable or nonhyperbolic moveout using an effective orthorhombic moveout model. Events in the τ-p domain, in CRS gathers, and in common image gathers are also commonly flattened to obtain useful parameters. The method is identical in these other domains; rather than an NMO equation though, the right-hand side of 3.1 would represent the physical flattening equation for the appropriate gather type.

In the examples included above, I fit the difference in time-squared $\Delta = t^2 - t_0^2$, but t_0 can be just as easily treated as a parameter to be fit as well. This can be useful for data where near offset traces are unavailable or overwhelmed with noise such as ground-roll. The procedure would remain the same, but in the simple cases, $\mathbf{\Delta}$ would become just a list of t^2 values, and the matrix $\mathbf{X}$ would contain an extra column of ones (or another coefficient associated with t_0^2).

Time-warping provides the same computational cost improvements over the semblance scan as velocity-independent NMO does, but potentially more so as the number of parameters increases beyond three. However, flattening based analysis still requires significant post-imaging interpretation to distinguish between potential geologic causes. In the next chapter, I will examine diffraction

focusing as a velocity analysis criterion alternative to event-flattening. Although not as efficient as the event-flattening methods, diffraction focusing may help position imaging events and azimuthal velocity estimates more accurately, as it may help reduce the ambiguity between the various geologic causes.

Chapter 4

Azimuthally anisotropic 3D velocity continuation

Background*

As I have discussed in previous chapters, velocity analysis is commonly first performed on pre-stack CMP gathers, where the geologic cause of any observed azimuthal velocity variation is ambiguous. Without the help of additional diagnostic gathers such as hybrid or cross-spread gathers (Dunkin and Levin, 1971), or an interpretive comparison between picked root-mean-square (RMS) and interval velocities (Jenner, 2008), the cause of azimuthal variations in velocity can be identified only after migration.

Azimuthal seismic imaging commonly requires iterations between velocity analysis and imaging to help distinguish between the effects of anisotropy and heterogeneity, Residual azimuthal variations in traveltime after migration can be measured by using migration binning schemes which preserve both offset and azimuth information (Cary, 1999; Vermeer, 1999). This is the type of analysis I performed using time-warping on the Durham Ranch gathers in the previous chapter. After the first pass of (isotropic) migration, azimuthal variations in velocity are detected from residual moveout, which then provides the velocity model for anisotropic migration. Iterative processing flows that use these strategies are popular not only because they are fairly efficient and intuitive, but also because they can be implemented with minimal modification to existing software. However, iterative imaging flows cannot guarantee convergence to the correct or optimal velocity model

*Parts of this chapter are published in Burnett and Fomel (2011).

(Deregowski, 1990). The method I will discuss here is based on velocity continuation (Fomel, 1994, 2003b), which has the underlying strategy of performing velocity analysis and imaging simultaneously, and can thus be used to directly find an optimal velocity model without iteration (Yilmaz et al., 2001). Sicking et al. (2007a) have demonstrated the success of a similar strategy of using imaging as a velocity analysis tool for 3D multiazimuth reflection seismic data. Azimuthal velocity continuation can provide a theoretical framework for this approach. With these benefits as motivation, I extend diffraction imaging with time-domain velocity continuation to 3D, accounting for the case of azimuthally variable migration velocity.

In the previous chapters, the velocity analysis methods were based on traveltime event-flattening. In this chapter, I use a different criterion, image-focusing, to estimate the seismic velocity model. Image focusing as a tool for velocity analysis is not new. Harlan et al. (1984) introduce many of the key concepts in focusing analysis, including a quantitative focusing measure based on cross entropy or "non-Gaussianity" More recently, Sava et al. (2005), Fomel et al. (2007), and Biondi (2010) have demonstrated successful image-focusing techniques for seismic data.

Harlan et al. (1984) point out that the separation of diffractions from reflections could be useful in focusing based velocity analysis, as diffractions are more sensitive to migration velocity errors than reflections. More recent works have demonstrated diffraction velocity analysis in 2D and for ground penetrating radar (Novais et al., 2006; Fomel et al., 2007; Novais et al., 2008), as well as to the azimuthally anisotropic case (Al-Dajani and Fomel, 2010; Burnett and Fomel, 2010). Harlan et al. (1984) separate diffractions using a local slant stack technique, which distinguishes reflection events from diffraction events based on local slopes. But unlike the PWD filter method for local slope detection, their local slant stack technique is not subject to regularization, and therefore may have difficulty in estimating smooth slope fields robustly. Because of this, diffraction separation

has not necessarily been a standard step of image-focusing analysis methods. Fomel et al. (2007) demonstrate PWD filtering as a robust and efficient tool for diffraction separation on 2D field data. In this chapter, I extend their image-focusing method to 3D with diffraction separation as the first step. For the third time in this dissertation, I will use PWD filters to measure local slopes, but this time, I use the slopes for 3D diffraction separation, rather than a direct measure of traveltime geometry. In order to understand the benefits of diffraction separation, it is helpful to first briefly review how diffractions differ from reflections.

Diffractions are seismic energy scattered by subsurface discontinuities—geologic features such as faults, pinch-outs, channels, and so on. Specular reflections from flat layers are well-predicted by Snell's Law, which is the basis for CMP analysis and NMO. Even dipping layers can be treated by the same physical concept with a proper application of DMO. Snell's Law states that incident wave energy will reflect symmetrically about the normal direction of a surface, but it does not state what happens at say, a discontinuity, where the normal direction is undefined. At discontinuities, wave energy scatters in all directions that are away from the edge or point. We observe this scattered diffraction energy during seismic acquisition, but it is often neglected during processing, as conventional imaging flows are purposefully designed with reflections in mind.

The NMO and DMO corrections are imaging steps designed to effectively transform the recorded seismic data set into what it would look like if it were recorded with only coincident (zero-offset) source-receiver pairs at each CMP location. Once all data are transformed to zero-offset, offset itself becomes redundant, and therefore traces are summed over offset in the conventional imaging step of stacking. The stacked data set is usually the first approximated image of the subsurface recovered during a seismic imaging flow. Reflection geometries are approximately correct on stacked data, with some (often significant) positioning errors associated with dipping events and structures

(Yilmaz, 2001). Diffraction energy however, still remains scattered across midpoint locations on the stack image. This scattering across midpoints is geometrically similar to the moveout behavior associated with CMP reflections—that is, diffraction surfaces are approximately hyperbolic over midpoint on zero-offset data. However, unlike normal reflections on CMP gathers, one generally cannot assume to know the spatial location of a particular diffractor within the stack. Nonetheless, this diffraction moveout over midpoints provides another opportunity for traveltime velocity analysis.

Harlan et al. (1984) suggest an option for velocity analysis using separated diffractions. They show that when the correct migration velocity is used to image diffractions, they become well-focused, and thus their quantitative non-Gaussianity focusing measure becomes a proxy for velocity estimation. On large field data sets, especially modern 3D data sets, testing a range of velocity models could become computationally prohibitive. In addition to suggesting the use of PWD for diffraction separation, Fomel et al. (2007) also suggest velocity continuation as a means for efficiently testing a range of migration velocities.

Velocity continuation (Fomel, 1994, 2003b) provides a framework for describing how a seismic image changes given a change in the migration velocity model. Similar in concept to residual migration (Rothman et al., 1985) and cascaded migrations (Larner and Beasley, 1987), velocity continuation is a continuous formulation of the same process. Velocity continuation has found applications in migration velocity analysis (Fomel, 2003a; Schleicher et al., 2008a) and diffraction imaging (Novais et al., 2006; Fomel et al., 2007).

Fomel (1994) and Hubral et al. (1996) point out that velocity continuation is a wave propagation process. Instead of wavefronts propagating as a function of time, images propagate as a function of migration velocity. Recent work has extended the concept to heterogeneous and anisotropic velocity models (Alkhalifah and Fomel, 1997; Adler, 2002; Iversen, 2006; Schleicher and Alexio, 2007;

Schleicher et al., 2008b; Duchkov and de Hoop, 2009). To account for anisotropy, the seismic velocity model must become multi-parameter. Consequentially, velocity continuation generalizes to a process of implementing image transformations caused by changes in multiple parameters rather than the single isotropic velocity alone.

I begin below with a section on the theory of azimuthally anisotropic velocity continuation. I then discuss implementation of azimuthal velocity continuation using a spectral method. I provide synthetic examples to analyze the behavior of azimuthal velocity continuation and demonstrate focusing analysis by kurtosis. I then provide a field data example which shows diffraction separation and velocity estimation results. This field data example leads to the development of an alternative approach to focusing analysis using path-integral imaging, which I will discuss to conclude the chapter.

THEORY

The theory of velocity continuation formulates the connection between the seismic velocity model and the seismic image as a wavefield evolution process. In doing so, the process can be implemented in the same variety of ways as seismic migration. Seismic migration in its many forms is commonly derived starting from the wave equation, which is approximated by its time and amplitude components by the eikonal and transport equations, and if necessary, a system of ray tracing equations. Velocity continuation is derived in the opposite order (Fomel, 2003b). Starting with a geometrical description of the image, a corresponding kinematic equation for traveltime is derived to describe how the image moves according to changes in imaging parameters. Subsequently, the kinematic equation is used to derive a corresponding wave equation, which describes the dynamic behavior of the image as an evolution through imaging parameter coordinates. This section outlines the key steps of this

derivation, starting with a traveltime equation that permits azimuthal variations in velocity.

Grechka and Tsvankin (1998) truncate a two-dimensional Taylor series expansion for a generally inhomogeneous anisotropic media to derive the "NMO ellipse" moveout equation. Geometrically, the NMO ellipse model still assumes that events have hyperbolic moveout with offset, but it allows the velocity to change with azimuth. I start here by using the same truncated 2D Taylor series expansion to describe an azimuth-dependent traveltime equation for the diffraction traveltime or the summation surface of zero-offset time migration,

$$T^2(\mathbf{x}, \mathbf{y}, \mathbf{M}) = 4\left(\tau^2 + (\mathbf{x}-\mathbf{y})^{\mathrm{T}}\,\mathbf{M}\,(\mathbf{x}-\mathbf{y})\right), \tag{4.1}$$

where τ is the one-way vertical traveltime after migration, $\mathbf{x}$ is the (x_1, x_2) surface position of the zero-offset receiver in survey coordinates, $\mathbf{y}$ is the surface position of the point source image, and superscript $^{\mathrm{T}}$ denotes transpose. The three independent elements of the symmetric slowness matrix,

$$\mathbf{M} = \begin{pmatrix} M_{11} & M_{12} \\ M_{12} & M_{22} \end{pmatrix}, \tag{4.2}$$

have units of slowness-squared, and the eigenvalues and eigenvectors of $\mathbf{M}$ determine the symmetry axes of the effective anisotropic medium (Grechka and Tsvankin, 1998). The migration slowness matrix $\mathbf{M}$ has identical form and mathematical significance as the azimuthal reflection moveout slowness matrix $\mathbf{W}$, so though they are both denoted $\mathbf{W}$ when discussed separately in the literature. But $\mathbf{M}$ physically describes a different parameter, so I have changed the migration slowness symbol to $\mathbf{M}$ here, to maintain a self-consistent notation, as both parameters are discussed within this dissertation. Regardless of their differences in physical meaning, $\mathbf{W}$ and $\mathbf{M}$ both geometrically

parametrize an elliptical-hyperbolic surface. The formulas relating $\mathbf{W}$ to more intuitive parameters (equations 1.8-1.12) are all valid for $\mathbf{M}$ as well.

Conventionally, one assumes that equation 4.1 characterizes a particular event defined in image coordinates $(\mathbf{x}, \tau)$, but one can also describe how that event would transform given a change in the image parameters $\mathbf{M}$. Regardless of the velocity model, the observed traveltime T must remain unchanged between different images. From this observation, I arrive at the following set of conditions:

$$\nabla_{\mathbf{x}} T^2 = \begin{pmatrix} \frac{\partial T^2}{\partial x_1} \\ \frac{\partial T^2}{\partial x_2} \end{pmatrix} = 8\tau \nabla_{\mathbf{x}} \tau + 8\mathbf{M}(\mathbf{x} - \mathbf{y}) = 0, \tag{4.3}$$

and,

$$\nabla_{\mathbf{M}} T^2 = \begin{pmatrix} \frac{\partial T^2}{\partial M_{11}} & \frac{\partial T^2}{\partial M_{12}} \\ \frac{\partial T^2}{\partial M_{12}} & \frac{\partial T^2}{\partial M_{22}} \end{pmatrix} = 8\tau \nabla_{\mathbf{M}} \tau + 4(\mathbf{x} - \mathbf{y})(\mathbf{x} - \mathbf{y})^{\mathrm{T}} = 0. \tag{4.4}$$

Combining and reducing these conditions yields a system of equations that are defined only in the image parameter coordinates,

$$2\frac{\partial \tau}{\partial M_{11}} + \frac{\tau \left(M_{22} \frac{\partial \tau}{\partial x_1} - M_{12} \frac{\partial \tau}{\partial x_2} \right)^2}{\left(M_{12}^2 - M_{11} M_{22} \right)^2} = 0, \tag{4.5}$$

$$2\frac{\partial \tau}{\partial M_{22}} + \frac{\tau \left(M_{12} \frac{\partial \tau}{\partial x_1} - M_{11} \frac{\partial \tau}{\partial x_2} \right)^2}{\left(M_{12}^2 - M_{11} M_{22} \right)^2} = 0, \tag{4.6}$$

and,

$$2\frac{\partial\tau}{\partial M_{12}} - \frac{2\tau\left(M_{12}\frac{\partial\tau}{\partial x_1} - M_{11}\frac{\partial\tau}{\partial x_2}\right)\left(M_{22}\frac{\partial\tau}{\partial x_1} - M_{12}\frac{\partial\tau}{\partial x_2}\right)}{\left(M_{12}^2 - M_{11}M_{22}\right)^2} = 0. \tag{4.7}$$

The system of kinematic equations describing azimuthally anisotropic velocity continuation is then found by combining equations 4.5-4.7. In a vector notation, this becomes

$$\nabla_{\mathbf{M}}\tau + \frac{\tau}{2}\mathbf{M}^{-1}\nabla_{\mathbf{x}}\tau\left(\nabla_{\mathbf{x}}\tau\right)^{\mathrm{T}}\mathbf{M}^{-1} = 0, \tag{4.8}$$

where $\nabla_{\mathbf{x}}$ and $\nabla_{\mathbf{M}}$ are in the form given by equations 4.3 and 4.4.

The method of characteristics (Courant and Hilbert, 1989) provides a link between a kinematic equation (such as 4.8) and its corresponding wave-type equation. Fomel (2003b) demonstrates specifically how the method can be used to derive a velocity continuation wave equation from its kinematic counterpart. By first setting the characteristic surface condition,

$$\psi = t - \tau(\mathbf{x}, \mathbf{M}) = 0, \tag{4.9}$$

and replacing τ with ψ and t, I obtain an alternative form of equation 4.8,

$$\psi_t\nabla_{\mathbf{M}}\psi + \frac{t}{2}\mathbf{M}^{-1}\nabla_{\mathbf{x}}\psi\left(\nabla_{\mathbf{x}}\psi\right)^{\mathrm{T}}\mathbf{M}^{-1} = 0. \tag{4.10}$$

Equation 4.9 guarantees that the wavefronts of time-domain image wavefield P exist only where the arrival time τ is equal to the recorded time t at a given location. Now take both ξ_i and ξ_j to represent each of t, M_{11}, M_{12}, M_{22}, x_1, and x_2. According to the method of characteristics, if Λ_{ij} is the coefficient in front of $\frac{\partial\psi}{\partial\xi_i}\frac{\partial\psi}{\partial\xi_j}$ from kinematic equation 4.10, then the corresponding wave

equation will have the same coefficients Λ_{ij} in front of each $\frac{\partial^2 P}{\partial \xi_i \partial \xi_j}$ derivative. The time-derivative ψ_t is equal to 1 given equation 4.9, and is included in the first term of equation 4.10 to facilitate the use of the method of characteristics. Then, by introducing $\mathbf{P}_{xx}$ as the spatial Hessian matrix of the wavefield,

$$\mathbf{P}_{xx} = \begin{pmatrix} \frac{\partial^2 P}{\partial x_1^2} & \frac{\partial^2 P}{\partial x_1 \partial x_2} \\ \frac{\partial^2 P}{\partial x_2 \partial x_1} & \frac{\partial^2 P}{\partial x_2^2} \end{pmatrix}, \tag{4.11}$$

we arrive at the azimuthally anisotropic post-stack velocity continuation wave equation,

$$\nabla_{\mathbf{M}} P_t = -\frac{t}{2} \mathbf{M}^{-1} \mathbf{P}_{xx} \mathbf{M}^{-1}. \tag{4.12}$$

In the isotropic case, $\mathbf{M}$ is diagonal and $M_{11} = M_{22}$. Equation 4.12 then reduces to the isotropic velocity continuation equation first derived by Claerbout (1986).

Implementation

Since velocity continuation is described by a wave equation, it can be implemented in analogous ways to seismic migration. Here, I demonstrate a spectral implementation of equation 4.12. By first stretching the time coordinate of an input image from t to $\tilde{t} = t^2/2$, and then taking its 3D Fourier transform, equation 4.12 becomes the reduced partial differential equation,

$$i\Omega \nabla_{\mathbf{M}} \hat{P} = \frac{1}{2} \mathbf{M}^{-1} \mathbf{k} \mathbf{k}^{\mathrm{T}} \mathbf{M}^{-1} \hat{P}, \tag{4.13}$$

where Ω is the Fourier dual of $\tilde{t}$ and $\mathbf{k}$ is the wavenumber vector (Fourier dual of $\mathbf{x}$). Equation 4.13 has the analytical solution,

$$\hat{P}(\Omega, k_1, k_2, \mathbf{M}) = \hat{P}(\Omega, k_1, k_2, \mathbf{M}_0) e^{\frac{-i}{2\Omega}\mathbf{k}^{\mathrm{T}}(\mathbf{M}^{-1} - \mathbf{M}_0^{-1})\mathbf{k}}, \tag{4.14}$$

which shows that continuation of an image from an arbitrary $\mathbf{M}_0$ to $\mathbf{M}$ can be achieved by multiplication with a shifting exponential in the Fourier domain. One can also directly migrate an unmigrated image (stack) by using the 2×2 matrix $\mathbf{M}_0^{-1} = \mathbf{0}$ for the initial velocity. In practice, the coordinate stretch from t to $\tilde{t}$ should be carefully applied as data will be compressed along the time-axis for early samples.

With a range of slowness matrices $\mathbf{M}$, equation 4.14 can be used to quickly generate the corresponding range of anisotropically migrated images. When the correct velocity model is used, diffractions collapse to points, which we recognize as the image coming into focus. Although constant velocity models are used for each image, this type of spectral implementation can still be useful in the heterogeneous case, as different parts of the image will come into focus locally as the appropriate velocity is used (Harlan et al., 1984; Fowler, 1984). Once the range of images is generated, I search for the best-focused image at each output location. Image focusing may be measured in various ways, but I will start by using the image attribute of kurtosis. I will present an alternative or supplemental focusing measure using path-integral imaging in a later section. Kurtosis is defined as,

$$\Phi(\mathbf{M}) = \frac{\int\int P^4(\mathbf{x}, t, \mathbf{M})\, d\mathbf{x}\, dt}{\left[\int\int P^2(\mathbf{x}, t, \mathbf{M})\, d\mathbf{x}\, dt\right]^2}, \tag{4.15}$$

(Wiggins, 1978; Levy and Oldenburg, 1987; Fomel et al., 2007). Including integration limits specifies a window size for locally measuring kurtosis in the image. In application, the integration limits control either the size of a "sliding window", or when viewing kurtosis as a local attribute (Fomel, 2007a; van der Baan and Fomel, 2009), they can be used to control the smoothness enforced by

shaping regularization. In either case, the integration limits control a trade-off between the robustness of the focusing measurement and the resolution. From experience, typical limits for field data correspond to window sizes on the order of 10^1 samples in each dimension. It should be noted that the traveltime approximation of equation 4.1 loses accuracy in the presence of strong lateral heterogeneity (Grechka and Tsvankin, 1998), but is commonly used to estimate smooth effective parameter models. Following the maximum values through the resulting six-dimensional kurtosis hypercube, $\Phi(t, \mathbf{x}, \mathbf{M})$, and then slicing corresponding pieces from the output images volume, $P(t, \mathbf{x}, \mathbf{M})$, reveals a composite effective medium based heterogeneous velocity model and a well-focused composite image. This spectral implementation and slicing procedure is similar to searching through a set of constant-velocity f-k migrations, and can be completed without any prior knowledge of the velocity model (Fowler, 1984; Mikulich and Hale, 1992).

Synthetic Examples

Two simple synthetic examples are provided below to illustrate 3D velocity continuation over a range of velocity models. In the first example, I apply velocity continuation to a point diffractor. In the second example, I apply the method to a synthetic post-stack image of a set of faults. The second example illustrates fracture characterization through diffraction imaging as a potential application for 3D azimuthal velocity continuation. The data in both examples are modeled using equation 4.1, which geometrically approximates a diffraction surface as an elliptical-hyperbolic surface. Field data and more accurately modeled data will generally also exhibit nonhyperbolic moveout, for which equation 4.1 does not account. The physical validity and limitations of equation 4.1 are thoroughly discussed by Grechka and Tsvankin (1998), but I focus here on how well diffractions can be collapsed, and how well the velocity parameters can be measured, if the data are ideally described by equation 4.1.

Figure 4.1a shows a single diffraction event. The fastest direction of propagation is at α=105° counter-clockwise from the x_1 axis, with V_{fast}=3.50 km/s. The data in Figure 4.1a were modeled with ϕ=7% anisotropy, which may be quite high for most field cases, but it was chosen to allow the azimuthal variations in diffraction moveout to be visibly pronounced. As described above, we first stretch the time axis from t to $\tilde{t}$ and take the 3D Fourier transform of the data. Then I apply the phase-shift prescribed by equation 4.14 for a range of $\mathbf{M}$. I found it more intuitive to specify the parameter ranges in terms of V_{x_1}, α, and ϕ, and then convert them at each step into the three parameters of $\mathbf{M}$ for use in equation 4.14. The inverse of the in-line velocity squared $1/V_{x_1}^2$ is equivalent to M_{11}, which, along with a given fast azimuth α and percent anisotropy ϕ, can be used to calculate M_{12} and M_{22} using equations 1.8-1.11. Last, I apply the 3D inverse Fourier transform and unstretch from $\tilde{t}$ to t to obtain the 6D image volume. Examples from the image volume using incorrect parameters are shown in Figures 4.1b-4.1c. The correct parameters are used in Figure 4.1d, where the image is well-focused.

Since only a single diffraction is present in this example, we can measure kurtosis over a window spanning the entirety of each 3D image, reducing the kurtosis volume from 6D to 3D. Figure 4.2 is a 2D slice of the kurtosis volume at the correct $M_{11} = 1/V_{x_1}^2$ value of $0.0935 = 1/(3.27 \text{ km/s})^2$. The peak of the kurtosis map is near the correct values of ϕ=7 and α=105°. Once the peak of the kurtosis map is identified, one could refine the increments around the peak to yield more accurate estimates. The physical limitations of resolving azimuthal velocity parameters are discussed by Al-Dajani and Alkhalifah (2000).

In practice, a conventional in-line 2D velocity analysis directly yields M_{11} from $1/V_{x_1}^2$, so Figure 4.2 could illustrate a realistic scenario for using 3D velocity continuation to improve upon a previous isotropic velocity model. In such a case, one would use previous V_{x_1} picks to hold M_{11}

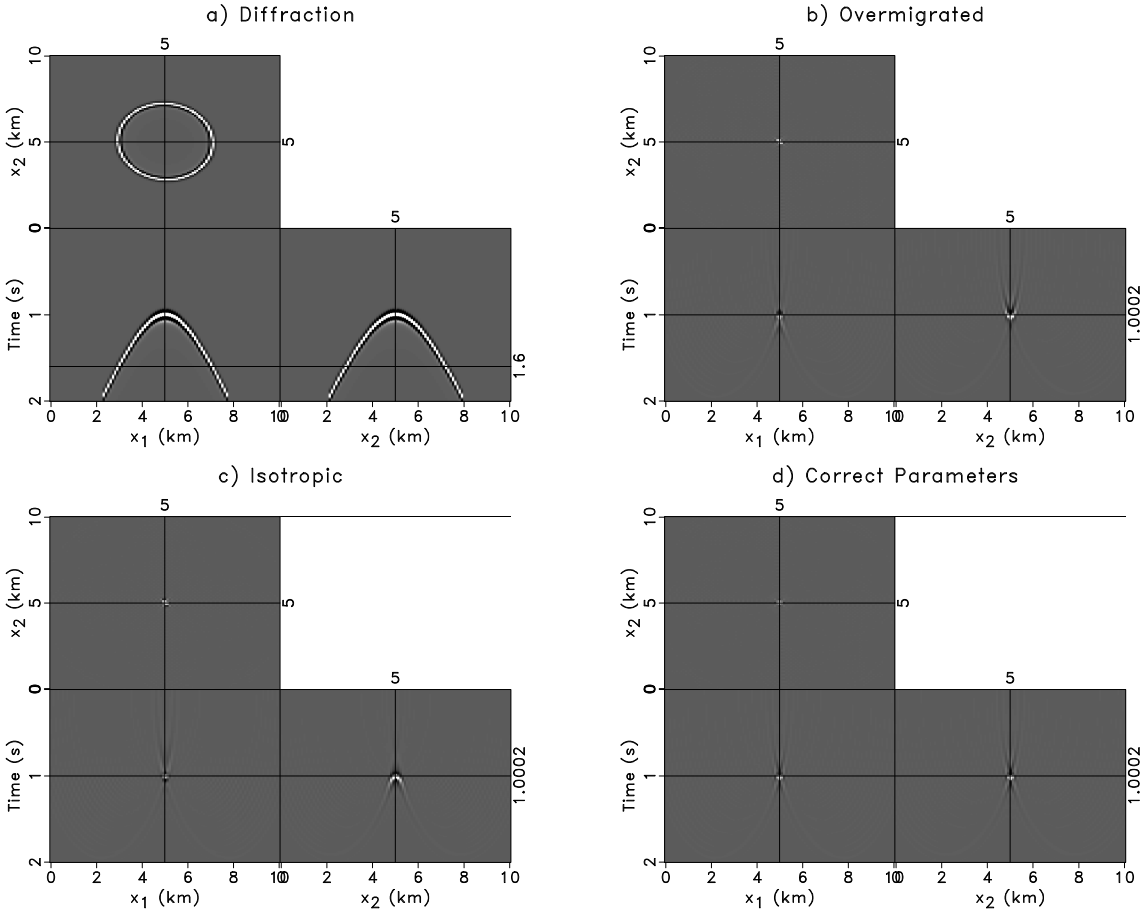

Figure 4.1: (a) A single azimuthally anisotropic diffraction. (b) The diffraction migrated by velocity continuation using correct parameters except ϕ=10, resulting in overmigration along x_2. (c) Migration using the correct M_{11}, but assuming isotropy. The result is now undermigrated along x_2. (d) Migration using correct parameters. The image is well focused in both directions. chapter-velcon/../seg10/threedim images

constant, and then effectively test a variety of M_{12} and M_{22} values. Since M_{11} and M_{22} are measured with respect to the survey coordinates, either (or both) can be measured independently via a single-azimuth semblance scan, along x_1 or x_2, respectively. The best isotropic velocity based on a fully multiazimuth 3D semblance scan will generally not represent either M_{11} or M_{22}, but it can help limit the range of test parameters. Note that this method does not require prior knowledge of the velocity model, but without prior knowledge, the kurtosis measure remains a 6D volume. Although more difficult to visualize, the 6D kurtosis volume is computationally just as easily scanned for optimal imaging parameters as the 2D map in Figure 4.2.

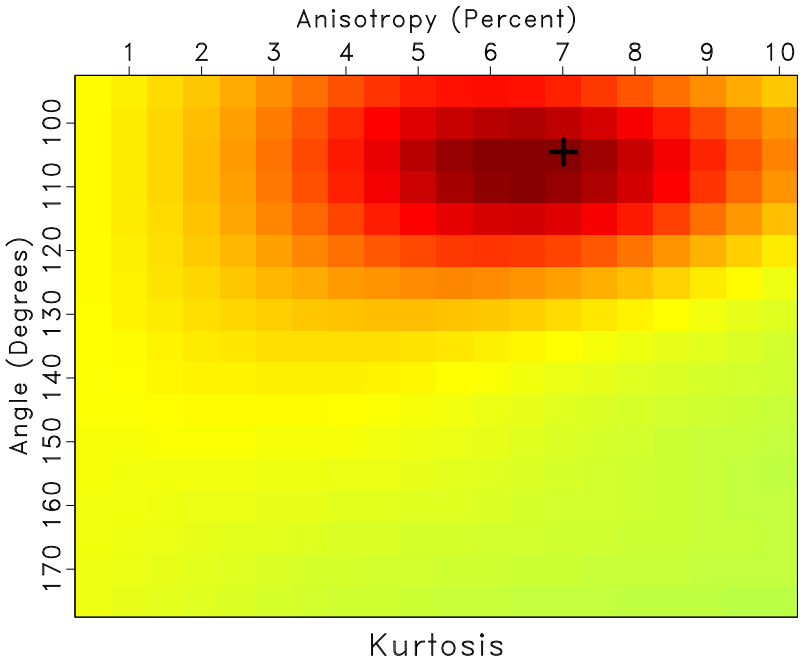

Figure 4.2: Kurtosis values for the velocity continuation of the diffraction in Figure 4.1a. The map covers a range of anisotropy and fast azimuth values with an increment in α of 5° and an increment in ϕ of 0.5%. The correct values at 105° and 7% anisotropy (indicated by crosshairs) coincide with the peak of the kurtosis map. chapter-velcon/../seg10/threedim focus

In the next example, I illustrate the concept of applying 3D anisotropic velocity continuation

to diffraction imaging and fracture characterization. Figure 4.3a shows a 3D synthetic post-stack diffraction data set, equivalent to the ideal separation of diffractions from specular reflections in post-stack data following Fomel et al. (2007). A fault map from Hargrove (2010) (shown in Figure 4.3a) was digitized and used to create a 3D fracture model. Each fault location was used to generate a point diffraction in a homogeneous anisotropic background via equation 4.1. A timeslice of the modeled diffraction data is shown in Figure 4.3b. The faults in the model typically have a strike of 112°, and in cases where faults and nearby fractures (which more likely influence the seismic velocity) are similarly aligned, the fast direction of seismic wave propagation tends to align with their strike. By assuming a typical tight sandstone velocity of V_{fast}=4.0 km/s with 3% anisotropy, I choose the modeling $\mathbf{M}$ to be comprised of M_{11}=0.0659, M_{22}=0.0631, and M_{12}=0.0014 (all in s^2/km^2). This results in a fast velocity direction along the strike of the faults. In Figure 4.3d, we see that 3D velocity continuation using the correct parameters (again found by maximum kurtosis) allows the faults to be clearly imaged. If an intermediate isotropic velocity model is used, as in Figure 4.3c, the diffractions are still imaged, but they are not as well-focused compared to the anisotropically migrated diffractions in Figure 4.3d. Conventionally, diffraction arrivals such as those in Figure 4.3a may be viewed as noise, but by separating them and treating them as signal, we can see here that imaging of steep and detailed features while simultaneously extracting anisotropy information may be possible.

Field Data Examples

Next, I apply velocity continuation to the Gibson Gulch data set from the Piceance Basin in Northwest Colorado, USA. This data set was provided by the Bill Barrett Corporation and Antero Resources as part of a research project sponsored by the Research Partnership for Securing Energy for America (RPSEA). One aspect of the RPSEA project is to develop and evaluate fracture detection

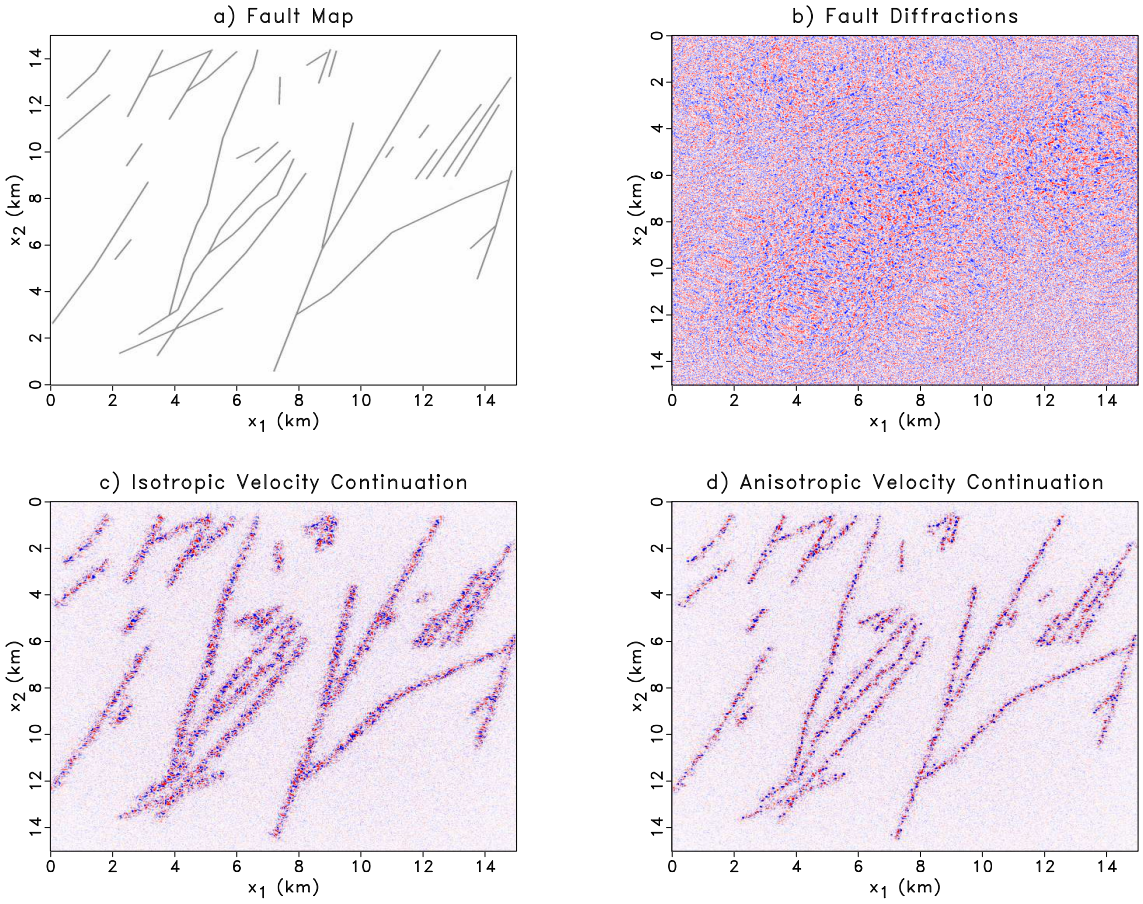

Figure 4.3: (a) Fault map from Northwest Scotland from Hargrove (2010) used to model diffraction data. (b) Synthetic post-stack diffraction data modeled using equation 4.1 and a 3D model based on the fault map in (a). (c) Diffractions from (b) migrated using an isotropic velocity model. (d) Diffractions from (b) migrated by anisotropic 3D velocity continuation. chapter-velcon/../seg10/fracs images-mig-all

tools using surface seismic data, so for this data set, I will also discuss the geologic implications of my analysis below.

I begin with the provided stacked volume and measure local slopes throughout the stack using plane-wave destruction (PWD) filters (Fomel, 2002). A timeslice from the stack volume is shown in Figure 4.4(a). Following Fomel et al. (2007), we assume reflection energy determines the dominant slope fields measured by PWD filters. I use the inline and crossline slope fields to design a structure enhancing filter to predict reflection energy (Liu et al., 2010). I then subtract the predicted reflections from the input stack to isolate diffraction energy. The same timeslice from the stack is shown for the separated reflection and diffraction energy after velocity continuation in Figures 4.4(b) and 4.4(c), respectively. Notice the fault in the bottom right of the diffraction image. By measuring kurtosis throughout images generated using a range of azimuthally anisotropic velocity models, I extract the azimuthal anisotropy parameters throughout the image (Figures 4.4(d)-4.4(f)).

The diffraction image in Figure 4.4(a) clearly shows a fault passing through the lower right, and seems to have a texture suggesting features of a dominant strike parallel to the crossline axis (left to right). However, the image is quite noisy, mainly because spectral imaging of diffractions suffers more from migration artifacts than reflection imaging does. The amplitudes of separated diffractions in field data are generally the same strength as their own spectral imaging artifacts, and they do not benefit from spatial amplitude tapering techniques that help with reflection imaging. One effective approach to producing a cleaner image is extensive zero-padding on the time-axis before taking the data to the Fourier domain, which is fortunately still relatively inexpensive in terms of computational cost.

The velocity estimates obtained using kurtosis have an unusual pattern for a velocity model, which may be a signature of detailed diffraction-generating features, or an unwanted side-effect of

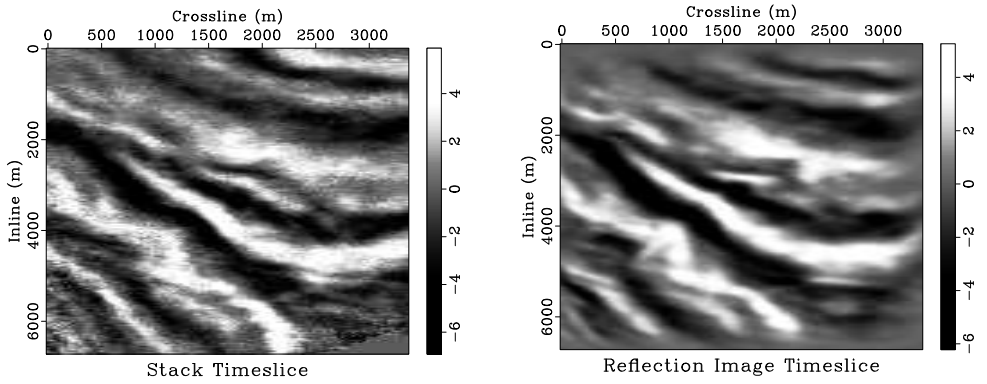

(a)

(b)

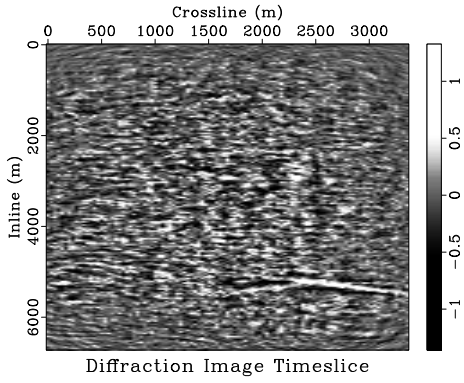

(c)

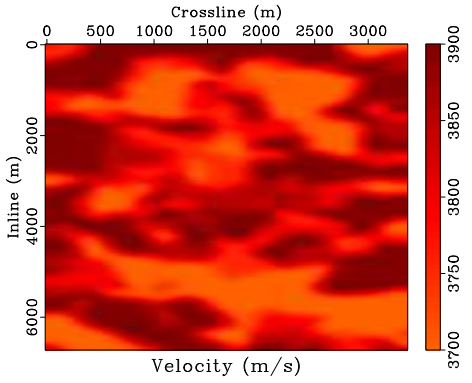

(d)

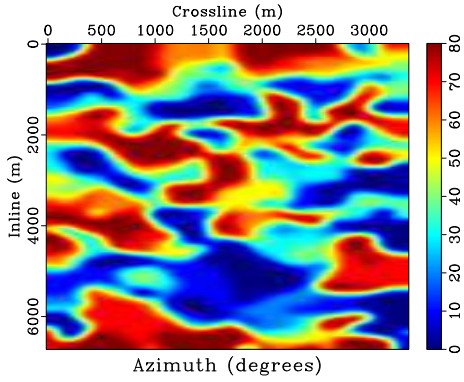

(e)

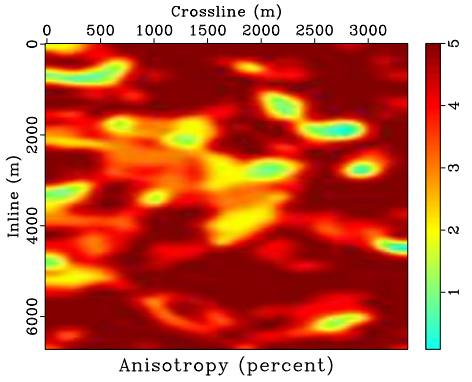

(f)

Figure 4.4: The same timeslice from image and attribute volumes found by velocity continuation. a.) Timeslice from stack. b.) Separated reflections imaged though velocity continuation. c.) Separated diffractions imaged through velocity continuation. d.) Background velocity estimated from kurtosis. e.) Slow azimuth estimated from kurtosis. f.) Percent anisotropy estimated from kurtosis.

chapter-velcon/../eage11/figures data,refdata,difdata,velocitymap,azimuthmap,anisotropymap

the analysis. Although not likely a problem here, diffractions are often sparsely located throughout an image after separation, and focusing analysis can give misleading velocity estimates in between diffraction events. Even for reflection images, in regions with few events (e.g., inside Gulf of Mexico salt bodies), the correct image can appear "de-focused" according to any quantitative focusing measure. Kurtosis, for example, is effectively a measure of how poorly data locally correlate with a constant (Levy and Oldenburg, 1987), so if the correct image is nearly a constant, then kurtosis may predict incorrect velocities attributed to noise or diffraction flanks in that region. Because of this possibility, kurtosis-based focusing analysis is probably best used as a residual imaging tool, for cases where a reasonable migration velocity estimate is known. This is of course almost always the case post-stack, as the reflection moveout velocities from NMO analysis are readily available. In the Gibson Gulch case however, the stack was prepared before it was given to our group at UT, and the velocity model was not readily available.

The issues of poor signal-to-noise and velocity uncertainty lead me to investigate a potentially more robust focusing measure which could be used as an alternative or as a supplement to kurtosis. I will describe this focusing measure next, which is based on the concept of path-integral imaging—a concept that will itself need a brief introduction, as I provide below.

Path-integral Diffraction Imaging

Using path-integrals in seismology was originally used for forward modeling of seismic data and wave propagation by various authors (Sen and Frazer, 1991; Schlottmann, 1999; Lomax, 1999; Botelho, 2010). Using a path-integral formulation for seismic imaging, however, was introduced by Keydar (2004) and Landa (2004), who show that an accurate version of the subsurface image can be found by summing a set of possible images with different velocity models. Landa et al.

(2006) generalize path-integral imaging further to pre-stack time and depth imaging by considering appropriate image-weighting functions.

Path-integral imaging works on the premise that the correct image remains stationary over various imaging parameter models. For zero-offset data, diffraction apexes remain stationary regardless of migration velocity, making zero-offset diffraction imaging a suitable application for path-integral imaging strategies. Velocity continuation provides an efficient means to generate the many image realizations required for path-integral imaging. Path-integral imaging is in theory a homeomorphic imaging strategy—truly independent of velocity model knowledge (Landa, 2009)—but the velocity model itself can provide valuable information concerning subsurface geology. The ability to extract velocity model parameters via path-integral imaging is therefore useful, and has been previously investigated by Schleicher and Costa (2009). Combining path-integral imaging with velocity continuation also provides an option for extracting velocity information.

Here, I view the output images from velocity continuation as "test" images, each of which is associated with its corresponding constant migration velocity. I first sum all test images to produce a path-integral image, and assume it to be an approximation of the optimal subsurface image. Path-integral diffraction imaging also helps attenuate spectral migration artifacts as they are attenuated by the image summation. Only the parts of each test image may be focused properly by their constant velocity, whereas the path-integral image approximates the result of using a fully heterogeneous velocity model. I then find regions within each test image that resemble the path-integral image using the nonstationary measure of local similarity (Fomel, 2007a). High similarity to the path-integral therefore provides an alternative to focusing for indicating the correct velocities throughout the image.

I begin by introducing the path-integral image $\check{P}$ as,

$$\check{P}(t,\mathbf{x}) = \int_{\mathbf{M}_a}^{\mathbf{M}_b} F(t,\mathbf{x},\mathbf{M}) P(t,\mathbf{x},\mathbf{M})\, d\mathbf{M}, \tag{4.16}$$

where $P(t,\mathbf{x},\mathbf{M})$ are test images found from the inverse Fourier transform of the result from equation 4.14, and the difference in the integration limits $\mathbf{M}_b - \mathbf{M}_a$ defines a "velocity aperture". Equation 4.16 represents a zero-offset imaging path-integral, as defined by Landa et al. (2006), where $F(t,\mathbf{x},\mathbf{M})$ is a user-specified weighting function to help constrain the summation to more likely velocities. Landa et al. (2006) discuss several weighting function options, including the limiting case of $F(t,\mathbf{x},\mathbf{M}) = \delta(t,\mathbf{x},\mathbf{M}-\mathbf{M}_p)$, which is equivalent to the classical imaging approach when $\mathbf{M}_p$ is equal to a picked velocity model. I will examine diffraction path-integral images below using either no weighting, ($F(t,\mathbf{x},\mathbf{M}) = 1$), or the real-valued Einstein-Smoluchovsky exponential weighting functions borrowed from particle physics,

$$F(t,\mathbf{x},\mathbf{M}) = e^{cL(t,\mathbf{x},\mathbf{M})}, \tag{4.17}$$

where c is an empirical user-selected parameter and $L(t,\mathbf{x},\mathbf{M})$ is some likelihood function such as a semblance output (Landa et al., 2006). In the examples where I use the Einstein-Smoluchovsky weighting function, I use kurtosis as the likelihood function. If the weighting function is set equal to 1 for all t-$\mathbf{x}$-$\mathbf{M}$ image locations, the integration described be equation 4.16 can alternatively be performed in the Fourier domain by substitution into equation 4.14.

In practice, the integral in equation 4.16 is replaced by a discrete summation, where a finite number of constant-velocity images generated by continuation are stacked. I store the constant velocity images as well, and then measure local similarity between the path-integral image and

each of the individual images. This results in a volumetric attribute $\gamma(t, \mathbf{x}, \mathbf{M})$ for each test image $P(t, \mathbf{x}, \mathbf{M})$,

$$\gamma(t, \mathbf{x}, \mathbf{M}) = \mathcal{S}\left[\check{P}(t, \mathbf{x}), P(t, \mathbf{x}, \mathbf{M})\right], \tag{4.18}$$

where $\mathcal{S}$ is the local-similarity operator as defined by Fomel (2007a). For each t-$\mathbf{x}$ location, the maximum similarity among all test-images can be used to indicate which image is best-focused, and its corresponding velocity can be assigned as the migration velocity at that location. Repeating for all locations conceptually defines a surface of maximum similarity in the t-$\mathbf{x}$-$\mathbf{M}$ space. This surface represents the heterogeneous effective migration velocity model, and can be used to "slice" along the best-focused points in the $P(t, \mathbf{x}, \mathbf{M})$ test image volume in the same way as kurtosis was used previously, thus creating a composite version of its corresponding migrated image.

The synthetic data set in Figure 4.5a was created by modeling a single zero-offset diffraction with a constant velocity of 4.0 km/s. The same data migrated using the correct velocity are shown in Figure 4.5b. I use the spectral implementation of velocity continuation from equation 4.14 to generate 201 images corresponding to range of velocities between 3.0-5.0 km/s. A sparse subset is summed and displayed in Figure 4.5c. When the full dense range of velocity-continued images is summed, the flanks of diffraction—whether over- or under-migrated—destructively interfere, and only the stationary apex remains. This full path-integral image (with no weighting) is displayed in Figure 4.5d, and compares favorably with the ideal result from Figure 4.5b.

The path-integral image has suppressed spectral imaging artifacts, as these are also not stationary with respect to velocity, and therefore cancel. From this perspective, the artifacts familiar to f-k or Stolt migration can be viewed as ringing due to sharp imaging discontinuities along the

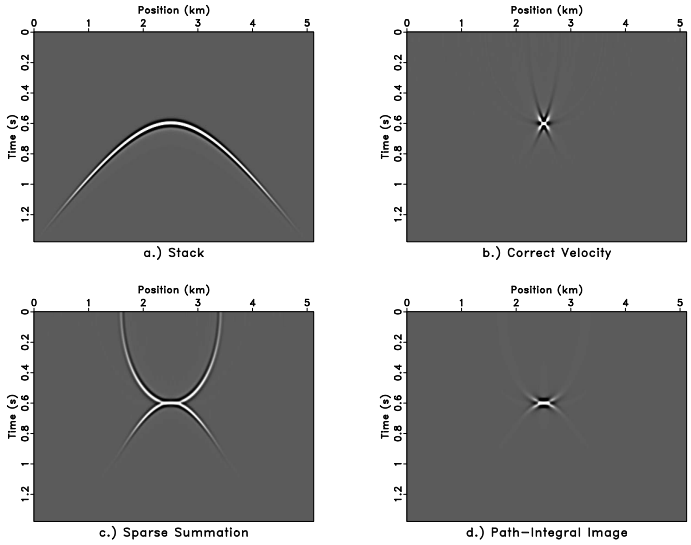

Figure 4.5: Single synthetic diffraction illustrating the path-integral method. a.) Input diffraction modeled at 4.0 km/s. b.) Input migrated using the correct velocity. c.) Path-integral image using only a sparse set of test images. Notice the diffraction apex remains in place, regardless of the velocity model. d.) Path-integral image using full dense range of test images. chapter-velcon/. figure-single

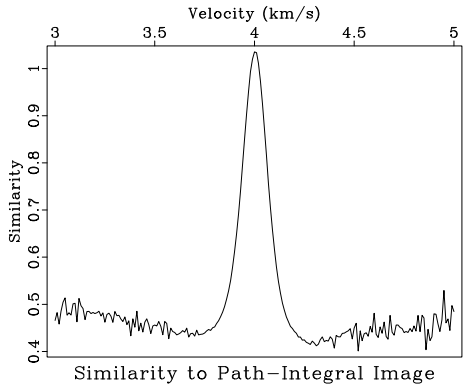

Figure 4.6: Local similarity to path-integral at the diffraction apex. Each test image corresponds to a homogeneous migration velocity on the horizontal axis. chapter-velcon/. simil-diff

velocity axis. However, careful comparison of the point diffractor images in Figures 4.5b and 4.5d shows that the path-integral image is not as spatially well-focused as the ideal result. The spatial focusing of the path-integral image is related to the frequency content of the diffraction, as well as velocity summation aperture.

I next use expression 4.18 to measure local similarity between each test image and the path-integral result. In Figure 4.6, we have plotted the local similarity at a fixed t-x location (in this case, at the center of the diffraction) for the entire range of test images. Each test image corresponds to a constant-velocity, shown on the horizontal axis of Figure 4.6. The images near the correct velocity of 4.0 km/s smoothly and significantly increase in similarity to the path-integral image, and the correct velocity corresponds to the maximum.

Fomel et al. (2007) provide a 2D field data example of diffraction focusing analysis, which they also made available as a reproducible experiment in Madagascar*. As a second path-integral imaging example, I reproduce their experiment, but substitute path-integral similarity for kurtosis as the focusing measure. Since the example is 2D, I will perform only isotropic velocity continuation, so the migration velocity M_0 takes the place of the velocity parameters $\mathbf{M}$ in the path-integral formulation. Figure 4.7(a) shows the diffractions separated following Fomel et al. (2007). These diffractions are the input to velocity continuation, and the results are summed to create the path integral images in Figure 4.8. The Einstein-Smoluchovsky path-integral image in the right of Figure 4.8 was created using kurtosis as the likelihood function. To help compensate for the slightly blurred result, I sharpened the path-integral image before comparing it to the test images by local similarity. Figures 4.7(b)-4.7(d) show the velocity estimates and images found by slicing velocity continuation

*Reproducible document available at `http://www.reproducibility.org/RSF/book/jsg/diffr/paper_html/`

test images along maximum values of similarity to the sharpened Einstein-Smoluchovsky path-integral. Individual picks throughout the data set are shown in Figure 4.9.

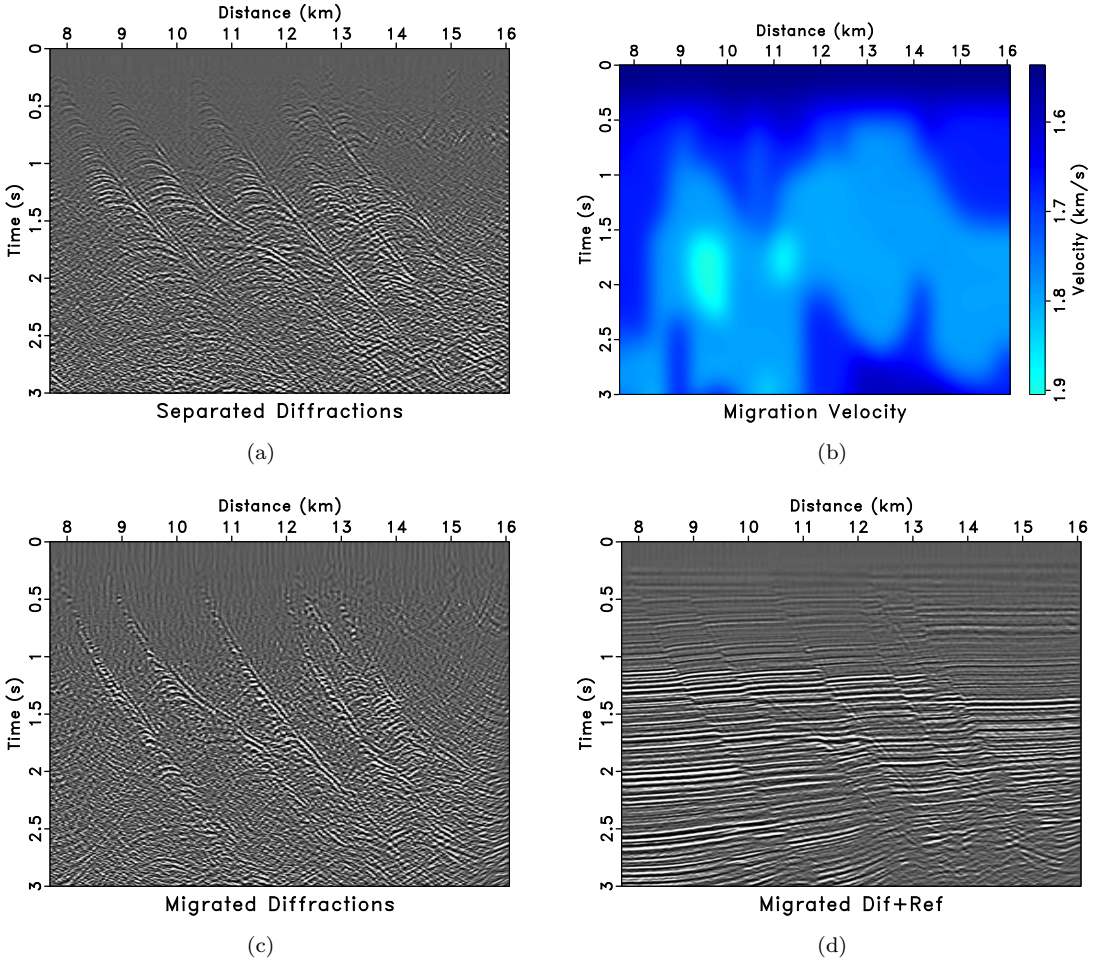

Figure 4.7: (a) Separated unmigrated diffractions. (b) Migration velocity esimated by path-integral similarity. (c) Composite diffraction image from path-integral similarity. (d) Composite migrated stack. chapter-velcon/bei bei-pwd,simpik,bei-simslice,bei-stack-simslice

For the field data example beginning with the stacked volume in Figure 4.10(a), the correct velocity model is unknown to the authors. This stacked volume was separated into its reflection and diffraction components using the method of Fomel et al. (2007) and structure-enhancing filters (Liu

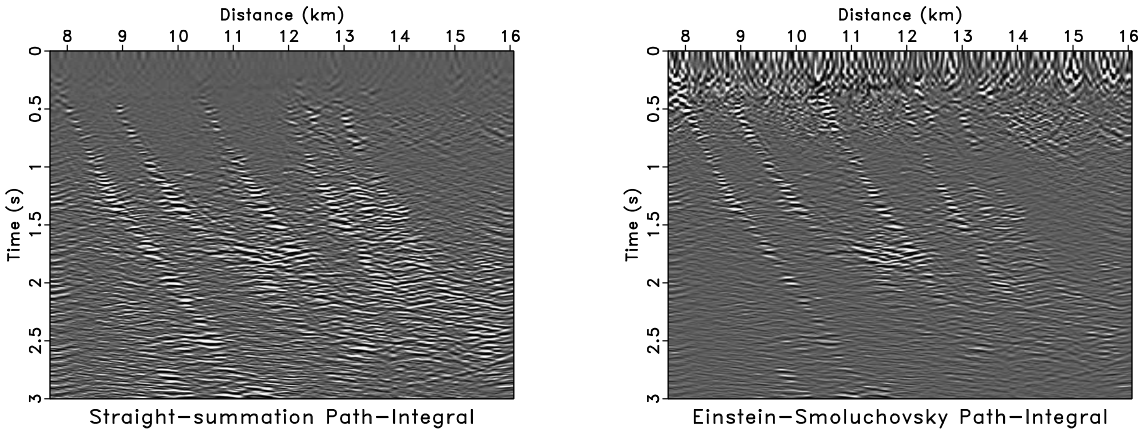

Figure 4.8: Path-integral images. Left: Path-integral using no weighting function ($F(t, \mathbf{x}, M_0) = 1$). Right: Einstein-Smoluchovsky path-integral using kurtosis as the likelihood function and $c = 0.7$ ($F(t, \mathbf{x}, M_0) = e^{0.7\Phi(t, \mathbf{x}, M_0)}$). chapter-velcon/bei paths

et al., 2010). The unmigrated separation results are shown in 4.10(b) and 4.10(c). Although the reflections are of course valuable, we discard them here and focus on the diffractions. The velocity continuation and summation procedure is applied over a broad range of velocities (3,000:50:5,000 m/s) to reveal the path-integral image shown in Figure 4.11(a). Each test image generated by velocity continuation is compared to the path-integral image using 3D local similarity. At each location, the velocity of the test image with maximum local similarity is assigned to the output velocity model. Local similarity is subject to shaping regularization to enforce a smooth output, resulting in the estimated effective heterogeneous migration velocity model for same diffraction volume, shown in 4.11(b). By also slicing through the test images along maximum similarity in the t-x-v space, I construct the corresponding composite diffraction image shown in 4.11(c).

The diffraction image in Figure 4.11(a) contains several interesting features which may be explained in the context of the geologic setting. Most of the image shows the upper Cretaceous

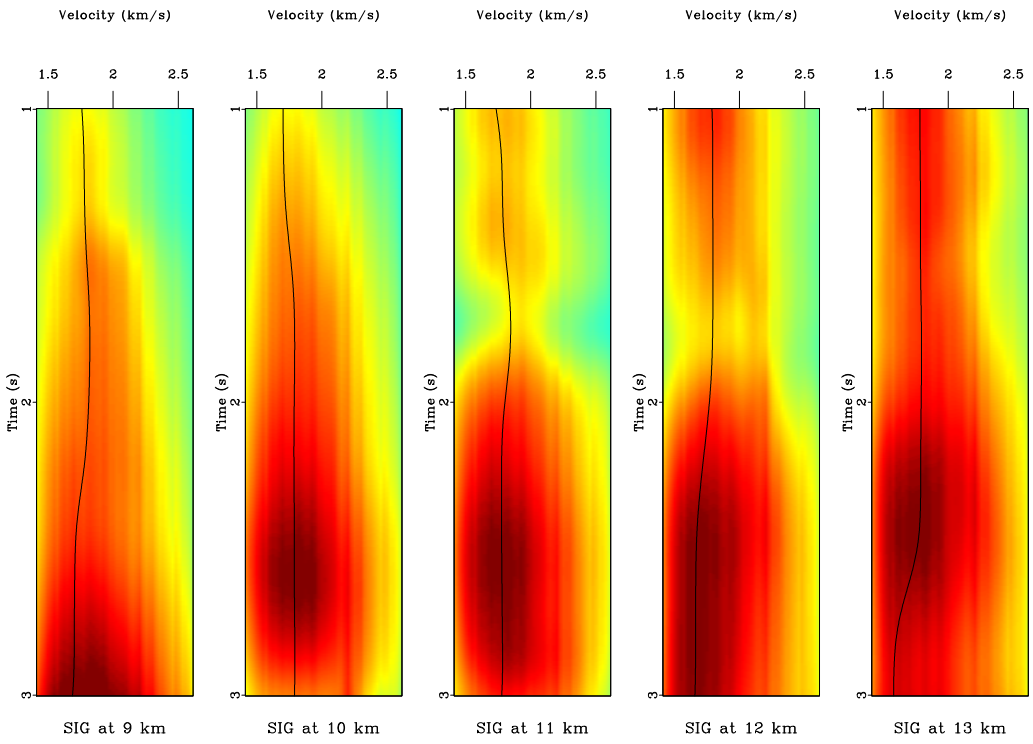

Figure 4.9: Path-integral similarity gathers (SIGs) at various locations in the data set. Background color indicates similarity for a given migration velocity, and the overlaid curves indicate auto-picking results from the similarity volume. chapter-velcon/bei simpanel

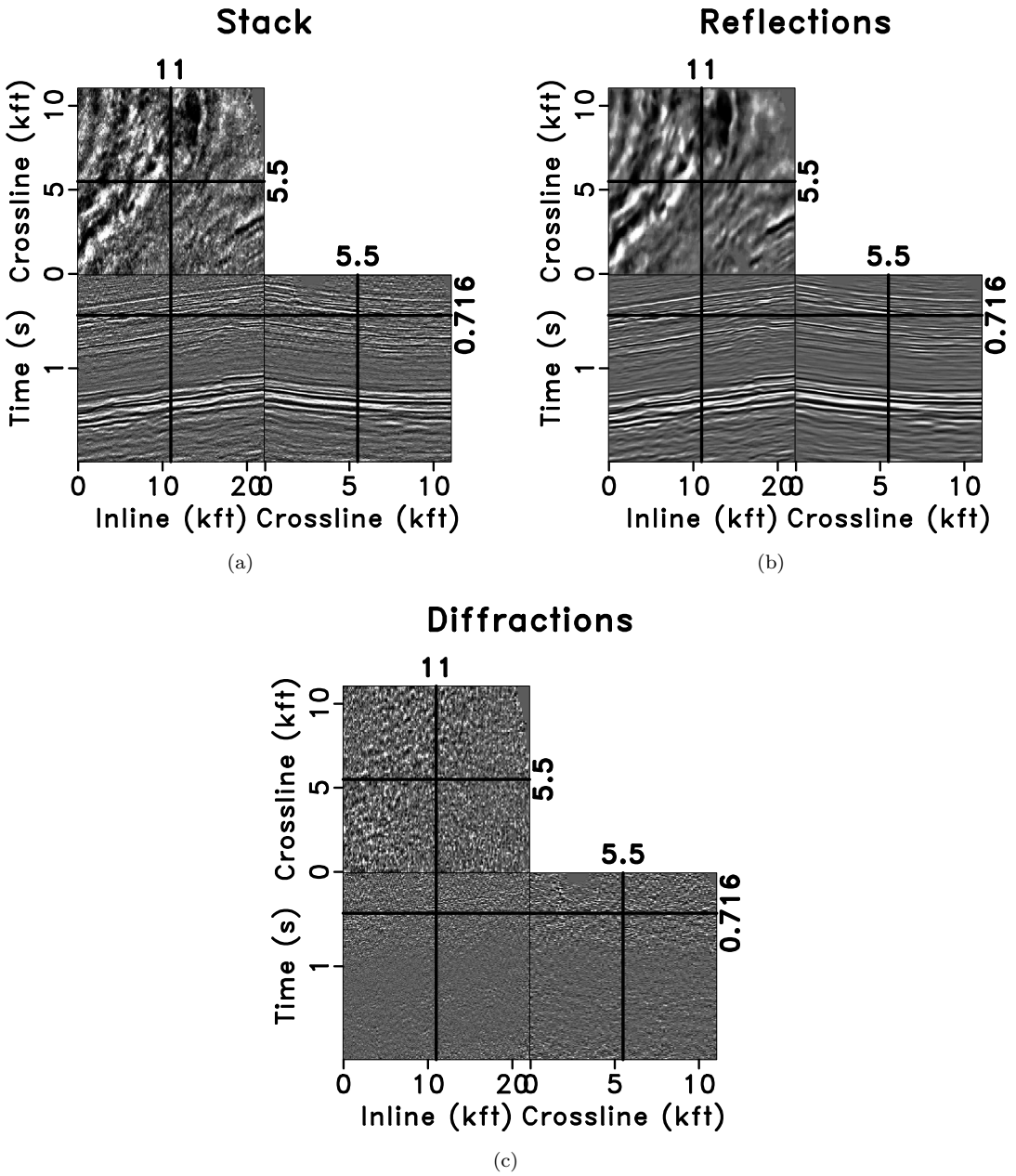

Figure 4.10: Diffraction separation. a.) Input stack containing both reflection and diffraction data. b.) Separated unmigrated reflections. c.) Separated unmigrated diffractions and other energy that does not follow the dominant slope fields. chapter-velcon/. stack4,filt,diff

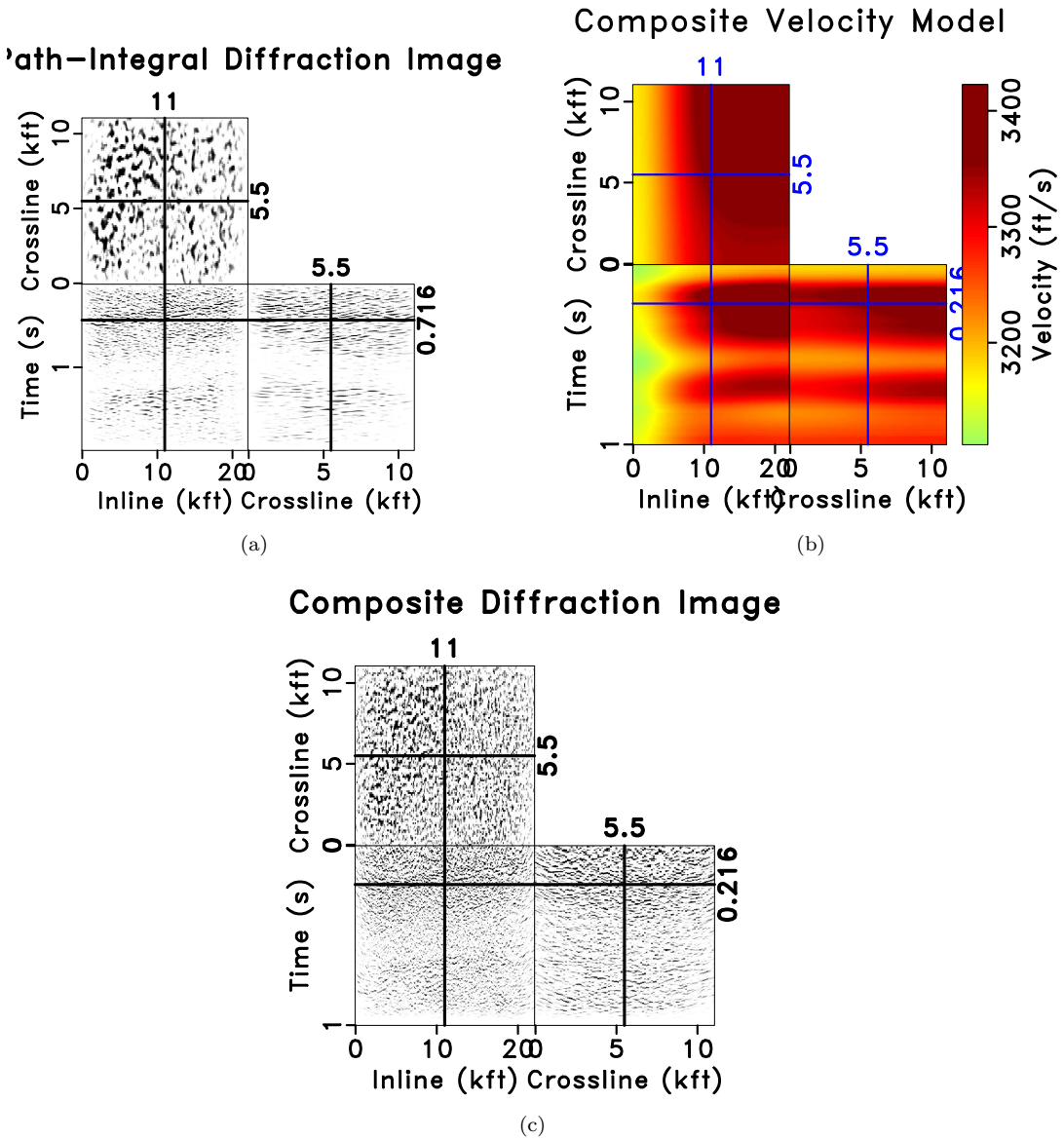

Figure 4.11: Path-integral image and results. a.) Diffraction path-integral image using full velocity range described in text. b.) Composite velocity model found by slicing test image coordinates along maximum similarity. c.) Composite diffraction image found by slicing test images along estimated maximum similarity. chapter-velcon/. dif-stat-vol,vel3D-composite,dif3D-composite

Williams Fork Formation of the Mesaverde Group, which is a known reservoir target in the Piceance Basin deposited in alluvial and coastal-plain settings (Pranter et al., 2007). Within these settings, braided channels were often deposited, as well as point-bar sand bodies on the convex banks of meandering streams and rivers. Point-bars are valuable reservoir targets in the Piceance Basin, but they are often isolated within less permeable mud and silt (Pranter et al., 2007), and therefore predicting their locations is itself valuable. Further, sands within the Mesaverde Group are commonly fractured along the regional stress direction of 110° (Heidbach et al., 2009; Lewallen et al., 2008), making point-bar deposits potential contributors to azimuthal anisotropy. The large-scale faulting features imaged in Figure 4.4(c) are aligned approximately perpendicular to the regional stress direction. In Figure 4.11(a), there is a region of intense scattering that sweeps down (increasing seismic arrival time, from about 0.3-0.8 seconds) from the east-southeast to the west-northwest. These diffractions could be generated from a migrating point-bar system moving towards the east-southeast over geologic time in the late Cretaceous. This movement could be part of a transgressive sequence on the western shore of the Western Interior Seaway (Pranter et al., 2007). If so, the diffraction imaging techniques presented here may provide direct imaging of potential drilling targets that cannot be reliably predicted from well information because of their laterally discontinuous nature.

Discussion

The zero-offset path-integral image can be recovered without any knowledge of the true heterogeneous migration velocity model, but the image is spatially blurred in the completely velocity-independent case. By constraining the velocity aperture, the stationary image becomes better focused, and as the aperture goes to zero around the correct velocity, the image becomes completely focused. This amounts to a trade-off between velocity-independence and spatial focusing.

The path-integral approach simplifies diffraction imaging when combined with velocity continuation by producing an estimate of the ideal image without the need to estimate velocity. The summation of zero-offset images in the velocity continuation space amplifies diffraction apex signals, while attenuating spectral migration artifacts. This is a key benefit of my method, as migration artifacts from diffractions are of comparable strength to the diffraction events themselves, and cannot be attenuated by tapering techniques designed for reflection imaging. I showed that for a reasonable range of velocities, the path-integral image is indeed blurred compared to the ideal result, but can serve as an estimate to compare each test image to, using local similarity. At each location in the path-integral image, the most similar test image yields a local velocity estimate, which combine with other local velocities to make a heterogeneous, effective-medium based, composite time migration velocity model. The final image can either be constructed as a composite image by slicing regions of the test images along the velocity model, or by using the estimated velocity model for a different variable-velocity migration algorithm.

By extending time-domain velocity continuation to the azimuthally anisotropic 3D case, I have combined the concepts of azimuthal imaging and diffraction imaging. I assume a three-parameter migration slowness model that allows velocity to vary elliptically with azimuth. I have provided simple examples to illustrate the potential application of this method to fracture characterization through diffraction imaging. By treating diffractions as signal, the method performs azimuthal analysis on post-stack data, without the requirement for common-offset-vector or offset-vector-tile binning schemes. This is possible because, unlike reflections, diffractions can preserve azimuthal information post-stack. Post-stack data volumes have obvious advantages over pre-stack data for analysis, including smaller memory size, and improved signal-to-noise ratio.

Allowing azimuthal variation in the migration velocity will result in improved imaging, which

is clearly a benefit of 3D velocity continuation. However, the potential for fracture characterization may be even more useful. The proposed method has many of the same ideas as the azimuthal imaging and fracture characterization flow proposed by Sicking et al. (2007a) for reflection data. Under the velocity continuation framework, I have extended the azimuthal imaging idea to 3D diffraction imaging. Since diffraction-generating fractures and faults are often nearly vertical and preferentially aligned, they can be associated with azimuthal anisotropy. Al-Dajani and Fomel (2010) have successfully demonstrated zero-offset diffraction image focusing as a fracture detection attribute on azimuth-sectored 3D field data. The method proposed here uses multiazimuth image focusing primarily as a velocity analysis criterion, but kurtosis itself could also be used as an image attribute. In cases where subsurface fractures cause azimuthal anisotropy, kurtosis as an attribute may be indicative of fracture intensity (Al-Dajani and Fomel, 2010). By applying velocity continuation to 3D diffraction imaging, one may be able to estimate both the orientation and the intensity of fractures from the resulting anisotropic velocity model and maximum kurtosis volumes, respectively. This information can be useful in reservoir development, as it can provide insight to subsurface fluid flow behavior.

Although the spectral implementation of azimuthal velocity continuation allows a range of possible images to be computed efficiently, it demands large amounts of memory to store a suite of images as well as the kurtosis volume. Modern computational hardware makes this approach feasible as-is, especially for target-oriented imaging and analysis strategies. Future studies may lead to better optimization-based approaches to finding local kurtosis maxima, in which case, this method could be practical for dense parameter estimation throughout full 3D volumes.

The underlying strategy of velocity continuation is to simultaneously estimate the velocity model as the data are imaged. This is beneficial in the case of azimuthal anisotropy, as the am-

biguity between structural heterogeneity and anisotropy is resolved without the need for iteration. Other multi-parameter seismic imaging problems, such as converted-wave imaging, which are also conventionally handled by iterative flows, could benefit from pre-stack versions of the 3D velocity continuation strategy.

Chapter 5

Conclusion

Summary

I have presented three novel data-driven approaches to time-domain azimuthally-anisotropic velocity analysis. I have chosen to investigate the case of azimuthal anisotropy because of its immediate importance in modern reservoir characterization, but in principle, the strategies used by my methods could be applied to other cases as well. Physically, all three methods estimate effective-medium approximations of the seismic wave group (ray) velocity. In the first two methods, the slowness ellipse, $\mathbf{W}$ is related to the NMO or stacking velocity, while for velocity continuation, the slowness ellipse, $\mathbf{M}$ is related to the migration velocity. The difference between stacking and migration velocities is discussed in Dobrin and Savit (1988). In cases with only $v(z)$ variations, both are related to the RMS velocity in the overburden. The RMS velocities in these cases can be related to interval parameters for different layers in the overburden using generalized Dix-type inversion, subject to stability requirements described by Grechka and Tsvankin (1998). Cameron et al. (2008) extend the Dix-type connection between the RMS velocities and interval velocities to cases with lateral variations as well. Aside from the image itself, subsurface interval parameters are the ideal information that seismic data analysis strives to provide. Rather than attempting to directly measure the interval parameters through physical modeling and inversion, I have taken a data-driven approach starting with velocity-independent imaging techniques. This has provided practical methods for extracting effective parameters which could then be converted to interval parameters using

a Dix-type inversion, or they could be used as an initial estimate for physics-driven velocity analysis and imaging.

It is worth commenting that each method can build upon a previously estimated velocity model by implementation as a residual analysis. Slopes can be measured on NMO-corrected gathers for time-warping and velocity-independent NMO, and the estimated residual traveltime shifts can be added to those applied by the initial correction. This residual analysis proved useful for both methods on field data, and even synthetic data, as slope detection becomes more stable for gently sloping events. In the velocity continuation case, focusing analysis is essentially a parameter scan—exactly the type I aimed to avoid in the first two methods. So, to gain its inherent benefits without making the computational cost unreasonable, one can limit the range of velocity continuation around an initially migrated image created with a representative velocity.

All three methods use local slopes estimated by PWD filters, but each for a different reason. In the first method, 3D azimuthally anisotropic velocity-independent NMO, local slopes are directly related to an assumed hyperbolic reflection moveout velocity. In the second method, time-warping, local slopes are used to predict reflection event surfaces, which are then fit with velocity parameters. In the third method, azimuthally anisotropic 3D velocity continuation, local slopes are used to predict dominant energy on a stacked section which is assumed to be reflection energy. Reflections are removed, leaving diffractions behind, which still contain velocity information post-stack.

Velocity-independent NMO is a physically-based method which makes it inherently the least complicated in application, as it is most closely related to conventional NMO. For the same reason, it is the most intuitive of the three methods presented in this dissertation. However, because it is physically-based, it must be applied in domains where the traveltime surfaces have an assumed geometry, and where the analytical description of that geometry has stable and meaningful first

derivatives. However, slopes are often physically meaningful throughout the seismic imaging flow, which allows velocity-independent NMO to fit into a larger framework of velocity-independent imaging (Fomel, 2007b). Further, local slopes are key information in imaging algorithms such as Gaussian beam migration (Hill, 1990), which has many variants, all of which assume some degree of localized imaging strategy. Velocity-independent NMO could also be performed in a similar localized sense, by using the local slope information in a gather to first decompose the gather into beamlets, and then to prescribe a mapping into the output domain. In this case, the output domain is just the NMO-corrected image, but subsequent steps could be included to perform azimuthally anisotropic migration in an approximate but efficient way.

Time-warping is non-physically based, which makes it more complicated in application, as it replaces assumptions with a sequence of domain-independent steps. It is probably the least elegant of the three methods I have presented, but I have had the most success applying it to field data. The feature of time-warping that makes it practical above velocity-independent NMO, is its flexibility. It is theoretically limitless in cases where event-flattening is a parameter estimation criterion. Time-warping has already been extended to nonhyperbolic moveout in the τ-p domain (Casasanta and Fomel, 2010), and to 3D (9-parameter) CRS/multifocusing methods (Kazinnik and Burnett, 2010), and there are still more gather types to try, such as image gathers. In just the t-$\mathbf{x}$ CMP space alone, I discussed isotropic, nonhyperbolic, and azimuthally-anisotropic moveout with 3D-, offset-, or spiral-sorting.

Velocity continuation uses event focusing as its velocity analysis criterion, which is best used on diffractions—not reflections as in the first two methods. I use the same three-parameter elliptical-hyperbolic surface as I did for CMP reflections, to describe diffraction geometry. The main strengths of azimuthally-anisotropic velocity continuation are that it reduces the total cost of

velocity analysis by operating on the stacked data rather than CMP gathers, and that it performs imaging and velocity analysis simultaneously. In this way, it simplifies the conventional approach to azimuthal imaging where velocity analysis and imaging are iterated to resolve intrinsic anisotropy effects from the similar effects and positioning errors caused by structural heterogeneity. Still, there are geologically common cases such as gas clouds and strong lateral heterogeneity, where the ambiguity will persist for both iterative imaging schemes or the velocity continuation approach.

Another strength of azimuthal velocity continuation arises specifically from using diffraction energy. Many of the same geologic conditions that are associated with azimuthal anisotropy are also commonly associated with diffraction-generating features such as faults, fractures, channel systems, and subsurface stress regimes. Path-integral imaging provided several surprises which led to further diffraction imaging insights. First, the diffraction path-integral image itself can be an interpretable image of diffraction-generating features which would be difficult to detect otherwise. Second, it was surprising to see the types of features which generated diffractions were not just large scale discontinuities, but also mid-scale features such as possible point-bar systems in the Gibson Gulch data set. However, the path-integral result is spatially blurred compared to the ideal result, so I have used it primarily as an intermediate image to which I compare all images generated by velocity continuation. This approach proved to be an effective velocity analysis tool with similar performance to kurtosis, and in my best example, I was able to use both in a complimentary technique, where kurtosis supplied the image likelihood function to use inside the velocity path-integral.

The review of results I have provided above can be reduced to the main novel conclusions and contributions of this dissertation. These main contributions and conclusions can be summarized as:

- Three novel data-driven approaches to time-domain azimuthally-anisotropic velocity analysis.
  - A method and formulation directly relating local slopes to azimuthally-variable reflection moveout velocities in 3D.
  - A reflection traveltime-fitting scheme using local slopes to pick traveltime surfaces.
  - A diffraction focusing method which accounts for azimuthally-variable velocity.
- Measuring inline and crossline local slope fields can be used as an alternative to semblance for capturing traveltime surface geometry and therefore azimuthally-variable velocity.
- The pre-stack reflection analysis methods I have developed are up to four orders of magnitude faster than the comparable full semblance scan in the azimuthally-anisotropic case.
- 3D diffraction focusing can be used to image discontinuities and map out regions of intense seismic energy scattering associated with juxtaposed lithologies.

The natural next step for any of these methods is to test their practical validity further using multi-disciplinary field data. I have provided three methods for efficiently measuring time-domain effective-medium-based parameters, which are geophysically useful for improving the seismic image, and theoretically useful for describing detailed subsurface information. It is my hope that having these efficient geophysical measurement techniques now readily available, will lead to more routine comparisons between azimuthal seismic information and other types of data such as outcrop or borehole measurements (core, well logs, and so on). Future multi-disciplinary studies should make it possible to determine to what degree azimuthal-seismic information is actually able to provide the types of geologic information predicted by theory.

Limitations and Best Practices

I have demonstrated most examples in this dissertation assuming CMP-gather reflection or stacked-diffraction surfaces are elliptical-hyperbolic, but the three methods could be applied using other geometric models. The limitations of the elliptical-hyperbolic approximation come from its inherent assumptions, such as mild vertical and lateral heterogeneity and the absence of nonhyperbolic moveout (Grechka and Tsvankin, 1998). Slope-estimation is a critically important step in each method, and I have found several practices useful to help avoid common pitfalls. First, steep events can appear aliased to plane-wave destruction filters, which are more accurate for gentle slopes. This has led me to the routine practice of applying an initial isotropic constant-velocity NMO correction to CMP gathers before I measure their slopes. Both time-warping and velocity-independent NMO can be applied in the residual moveout case, and for parameter estimation, the traveltime shifts associated with the isotropic NMO and the velocity-independent flattening are simply added. The only PWD parameter I frequently adjust between applications is the filter size, and I have consistently found success when the filter is about 30-50 time samples by 3-10 spatial samples. Again, increasing the size of the filter will increase the robustness of the slope estimation, but it will decrease the resolution.

Each of the methods also has its own limitations in practice, and some of these limitations are shared between methods. For example, velocity-independent NMO and velocity continuation require the traces to be on a regularized grid, whereas time-warping does not. If an unusual trace sorting is used during time-warping though, one must also sort any pertinent header information in the same way to perform parameter fitting. Velocity-independent NMO is limited in that it assumes a moveout model beforehand, and therefore it is best-suited for short-spread gathers where hyperbolic moveout is reliable. This also helps avoid another limitation of slope estimation at far

offsets, which is handling crossing events with conflicting slopes. Both velocity-independent NMO and time-warping are susceptible to the issue of conflicting slopes, which, if necessary, can be handled in two ways. First, if one event is preferred in terms of imaging and parametrization, plane-wave-destruction filters may be given an initial estimate of the slope field associated with the preferred event, and will tend to converge to the nearest dominant slope. Second, following the idea used in diffraction separation, an initial slope field may be used to remove the dominant events on a CMP gather, leaving the secondary conflicting events. Slope estimation could then be repeated on these residual events to characterize the conflicting slopes. Velocity-independent NMO and time-warping also share susceptibility to coherent noise (for example, multiples), where local slopes may correspond to unwanted events. Therefore, any multiple-attenuation steps should be done before slope detection whenever possible.

Velocity continuation on the other hand, is sensitive to random noise which will often be separated from reflections and imaged along with the diffractions. I have found that applying a simple low-pass filter to the diffraction data after separation can help attenuate random noise while preserving the lower-frequency diffraction events for velocity continuation. Velocity continuation also has the limitation of being applied to zero-offset data. Although stacking helps with reflection imaging, one must carefully apply NMO and DMO pre-stack with the goal of diffraction preservation in mind. Velocity continuation also has pitfalls such as imperfect diffraction separation and migration artifacts that are relatively powerful compared to diffraction signal. Again, careful pre-stack processing will influence the success of the diffraction separation, and a practical solution to attenuating migration artifacts is to zero-pad the data along the time axis before transforming it to the Fourier domain.

Extensions

I anticipate a variety of applications of time-warping simply because of its flexibility. One of the next most important steps would be to try fitting orthorhombic parameters to the painted surfaces. These estimated values will of course still be effective parameters, but it is not well-discussed how to use effective orthorhombic parameters, possibly because there is not yet a reliable way to measure them efficiently. Time-warping may open the door to this line of research.

In velocity continuation, the main limitation with the current method is the ability to store all generated images. This is a limitation for a single workstation, or a shared cluster (on which I performed these experiments), but for most practical cases, this is easily overcome with increasingly inexpensive disk space. Nonetheless, disk space is often still a concern, but the kurtosis map in Figure 4.2 is clearly well-behaved in the neighborhood of the correct velocity, which could lead to an optimization approach to finding focusing maxima.

Path-integral imaging is a theoretically homeomorphic imaging strategy, but has difficulty handling reflections and pre-stack data properly. Zero-offset diffractions, on the other hand, are ideally suited for path-integral imaging. When combined with velocity continuation, path-integral imaging may provide a fruitful research topic in diffraction imaging and velocity analysis, as there are still many questions to answer. Are there minimum velocity sampling requirements for creating a path-integral image? Can we deterministically account for (and remove?) the spatial blurring associated with the path-integral image? If so, diffraction imaging may be simplified dramatically, and velocity analysis could be further improved.

Finally, all of the field data examples I have shown in this dissertation were of course carefully processed by their respective owners, but none were processed with diffraction imaging in

mind. Further research and application of diffraction-friendly pre-stack processing and imaging may yet further improve the results presented here.

Velocity analysis by velocity-independent imaging

Many authors have used the "velocity-independent" term before, and I have done so here, hopefully in a general sense. The original motivation of velocity-independent strategies was to bypass velocity estimation altogether, as it is still one of the most time-consuming steps in the conventional flow. Historically, the velocity model may have been viewed as an inconvenience of necessity, but in modern reservoirs, the velocity model itself may contain critically valuable sub-seismic-wavelength geologic information. Therefore, even with an ideal velocity-independent imaging strategy, we will still often want to recover the velocity model.

All three of the proposed methods in this dissertation share the philosophy of velocity-independent imaging (Ottolini, 1983b; Fomel, 2007b; Fowler, 1984; Landa et al., 2006). In the first method, we see that we can avoid explicitly measuring velocity by instead measuring slopes. Of course, slopes contain complete geometry information, and therefore velocities as an attribute as well, but it is an elegant automated alternative. In the successful application of velocity-independent NMO, I abandoned the attribute-based approach in favor of using the velocity-independent NMO correction itself to shift the data and then fit the applied shifts with a velocity model. This was the first example of what I call velocity analysis by velocity-independent imaging.

The purpose of seismic imaging is to transform the recorded data into an image of the subsurface. In the context of the conventional seismic imaging flow, velocity is a prerequisite of imaging—velocity analysis comes first. In all of the approaches here, I perform the imaging step first, and then subsequently recover the velocity model that would have transformed the original data

into the velocity-independent result. In the first two methods, the imaging operation was reflection flattening (either physical or non-physical), and in the third method, the imaging operation was diffraction focusing. These imaging operations are possible to do first without knowledge of the velocity model using velocity-independent NMO, warping, or velocity continuation and path-integral imaging, respectively. In the first two cases, I was able to record to the traveltime shifts applied by each imaging step once I viewed time itself as an attribute. In the third case, I simply measured which image among all possible images was best-focused, or which one was most similar to the path-integral image estimate.

I have found that velocity analysis by velocity-independent imaging has inherent benefits over the semblance scan, mainly through computational efficiency and automation. These benefits are amplified in the context of multi-parameter velocity models, as I have shown here for the simple three-parameter case of azimuthal anisotropy. The characterization of lower symmetries of anisotropy could benefit from this approach, as well as other multi-parameter estimation problems such as CRS/multifold analysis or converted-wave analysis. As exploration and development targets increase in complexity, the demand for detailed information in the velocity model will come as well. There is still a tremendous gap between the reality of conventional velocity analysis and the ideally accurate velocity model estimates required by next-generation-geophysical methods such as full-waveform inversion. The strategies I have proposed here may help bridge this gap and reveal detailed subsurface insights along the way.

Bibliography

Adler, F., 2002, Kirchhoff image propagation: Geophysics, **67**, 126–134.

Aki, K., and P. G. Richards, 2009, Quantitative Seismology, Second Edition: University Science Books.

Al-Dajani, A., and T. Alkhalifah, 2000, Reflection moveout inversion for horizontal transverse isotropy: Accuracy, limitation, and acquisition: Geophysics, **65**, 222–231.

Al-Dajani, A., and S. Fomel, 2010, Fractures detection using multi-azimuth diffractions focusing measure: is it feasible?: Expanded Abstracts 80^{th} SEG International Convention, 287–291.

Alkhalifah, T., and S. Fomel, 1997, Residual migration in VTI media using anisotropy continuation, *in* SEP-94: Stanford Exploration Project, 327–337.

Alkhalifah, T. A., and I. Tsvankin, 1994, Velocity analysis for transversely isotropic media: 64th Ann. Internat. Mtg, Soc. of Expl. Geophys., 1000–1003.

Berkovitch, A., I. Belfer, and E. Landa, 2008, Multifocusing as a method of improving subsurface imaging: The Leading Edge, **27**, 250–256.

Bienati, N., and U. Spagnolini, 1998, Traveltime Picking in 3D Data Volumes: 60th Mtg., Eur. Assn. Geosci. Eng., Session:01–12.

Biondi, B., 2010, Velocity estimation by image-focusing analysis: Geophysics, **75**, U49–U60.

Blias, E., 2007, Long-spreadlength approximations to NMO function for a multi-layered subsurface: Recorder, **3**, 36–42.

Botelho, L. C. L., 2010, A Feynman path integral representation for elastic wave scattering by anisotropic weakly perturbations: International Journal of Theoretical Physics, **49**, 1396–1404.

Burnett, W., and S. Fomel, 2008a, 3-D velocity-independent elliptically anisotropic moveout correction: Expanded Abstracts 78^{th} SEG International Convention, 2952–2956.

———, 2008b, A gaussian beam analysis of the radon transform: Expanded Abstracts 78^{th} SEG International Convention, 2993–2997.

———, 2009, 3D velocity-independent elliptically anisotropic moveout correction: Geophysics, **74**, WB129–WB136.

———, 2010, Azimuthally anisotropic 3Dvelocity continuation: Expanded Abstracts 80^{th} SEG International Convention, 307–312.

———, 2011, Azimuthally anisotropic 3D velocity continuation: International Journal of Geophysics, Accepted for publication.

Cameron, M., S. Fomel, and J. Sethian, 2008, Time-to-depth conversion and seismic velocity estimation using time-migration velocity: Geophysics, **73**, VE205–VE210.

Cary, P. W., 1999, Common-offset-vector gathers: an alternative to cross-spreads for wide-azimuth 3-D surveys: Expanded Abstracts 69^{th} SEG International Convention, 1496–1499.

Casasanta, L., and S. Fomel, 2010, VTI interval velocities by predicitive painting in $\tau - p$ domain: Expanded Abstracts 80^{th} SEG International Convention, 232–237.

Castle, R. J., 1988, Shifted hyperbolas and normal moveout: 58th Ann. Internat. Mtg, Soc. of Expl. Geophys., Session:S9.3.

Christoffel, E. B., 1877, On the propagation of shock waves through elastic solids, *in* Classics of Elastic Wave Theory, 2007: Society of Exploration Geophysicists.

Claerbout, J., 1999, Everything depends on v(x,y,z), *in* SEP-100: Stanford Exploration Project, 1–10.

Claerbout, J. F., 1986, Velocity extrapolation by cascaded 15 degree migration, *in* SEP-48: Stanford

Exploration Project, 79–84.

———, 1992, Earth soundings analysis: Processing versus inversion: Blackwell Science.

Cooke, D., A. Bóna, and B. Hansen, 2009, Simultaneous time imaging, velocity estimation, and multiple suppresion using local event slopes: Geophysics, **74**, WCA65–WCA73.

Courant, R., and D. Hilbert, 1989, Methods of Mathematical Physics: John Wiley & Sons.

Crampin, S., 1984, Effective anisotropic elastic constants for wave propagation through cracked solids: Geophysical Journal of the Royal Astronomical Society, **76**, 135–145.

Deregowski, S. M., 1990, Common-offset migrations and velocity analysis: First Break, **08**, 224–234.

Dewangen, P., and I. Tsvankin, 2006, Velocity-independent layer stripping of PP and PS reflection traveltimes: Geophysics, **71**, 2120–2128.

Dix, C. H., 1955, Seismic velocities from surface measurements: Geophysics, **20**, 68–86.

Dobrin, M., and C. Savit, 1988, Introduction to Geophysical Prospecting: McGraw-Hill Inc.

Duchkov, A., and M. de Hoop, 2009, Velocity continuation in the downward continuation approach to seismic imaging: Geophysical Journal International, **176**, 909–924.

Dunkin, J. W., and F. K. Levin, 1971, Isochrons for a three-dimensional seismic system: Geophysics, **36**, 1099–1137. (Discussion in GEO-37-03-0545-0545 with reply by authors).

Etgen, J., and C. Regone, 1998, Strike shooting, dip shooting, widepatch shooting - Does prestack depth migration care? A model study.: 68th Ann. Internat. Mtg, Soc. of Expl. Geophys., 66–69.

Fomel, S., 1994, Method of velocity continuation in the problem of temporal seismic migration: Russian Geology and Geophysics, **35**, 100–111.

———, 2002, Applications of plane-wave destruction filters: Geophysics, **67**, 1946–1960.

———, 2003a, Time-migration velocity analysis by velocity continuation: Geophysics, **68**, 1662–1672.

———, 2003b, Velocity continuation and the anatomy of residual prestack time migration: Geo-

physics, **68**, 1650–1661.

———, 2007a, Local seismic attributes: Geophysics, **72**, A29–A33.

———, 2007b, Velocity-independent time-domain seismic imaging using local event slopes: Geophysics, **72**, S139–S147.

———, 2008, Predictive painting of 3-D seismic volumes: Expanded Abstracts 78^{th} SEG International Convention, 864–868.

———, 2009, Velocity analysis using AB semblance: Geophysical Prospecting, **57**, 311–321.

———, 2010, Predictive painting of 3-D seismic volumes: Geophysics, **75**, A25–A30.

Fomel, S., and V. Grechka, 1996, On nonhyperbolic reflection moveout in anisotropic media, *in* SEP-92: Stanford Exploration Project, 135–158.

Fomel, S., E. Landa, and T. Taner, 2007, Poststack velocity analysis by separation and imaging of seismic diffractions: Geophysics, **72**, U89–U94.

Fomel, S., and Y. Liu, 2010, Seislet transform and seislet frame: Geophysics, **75**, 25–38.

Fomel, S., and A. Stovas, 2010, Generalized nonhyperbolic moveout approximation: Geophysics.

Forel, D., and G. H. F. Gardner, 1988, A three-dimensional perspective on two-dimensional dip moveout: Geophysics, **53**, 604–610.

Fowler, P., 1984, Velocity independent imaging of seismic reflectors: 54th Ann. Internat. Mtg, Soc. of Expl. Geophys., Session:S1.8.

Fowler, P. J., 1997, A comparative overview of prestack time migration methods: 67th Ann. Internat. Mtg, Soc. of Expl. Geophys., 1571–1574.

Gelchinsky, B., 1988, The common reflecting element (CRE) method (non-uniform asymmetric multifold system): 6th Geophysical Conference, Austr. Soc. Expl. Geophys., 71–75.

Gelchinsky, B., A. Berkovitch, and S. Keydar, 1999, Multifocusing homeomorphic imaging–Part 1:

Journal of Applied Geophysics, **42**, 229–242.

Grechka, V., and I. Tsvankin, 1998, 3-D description of normal moveout in anisotropic inhomogeneous media: Geophysics, **63**, 1079–1092.

———, 2002, NMO-velocity surfaces and Dix-type formulas in anisotropic heterogeneous media: Geophysics, **67**, 939–951.

Grechka, V., I. Tsvankin, and J. K. Cohen, 1999, Generalized Dix equation and analytic treatment of normal-moveout velocity for anisotropic media: Geophysical Prospecting, **47**, 117–148.

Green, G., 1839, On the laws of reflexion and refraction of light at the common surface of two non-crystallized media, *in* Classics of Elastic Wave Theory, 2007: Society of Exploration Geophysicists.

Gulunay, N., M. Magesan, and H. Roende, 2007, Gather flattening: The Leading Edge, 1538–1543.

Hake, H., 1986, Slant stacking and its significance for anisotropy: Geophysical Prospecting, **34**, 595–608.

Hargrove, P., 2010, Fault-related Fracture Systems in the Cambrian Eriboll Formation, Northwest Scotland: A Field and Petrographic Study of a Tight Gas Sandstone Analog, M.S. Geo.Sci. Thesis: The University of Texas at Austin.

Harlan, W. S., J. F. Claerbout, and F. Rocca, 1984, Signal/noise separation and velocity estimation: Geophysics, **49**, 1869–1880.

Heidbach, O., M. Tingay, A. Barth, J. Reinecker, D. Kurfe, , and B. Müller, 2009, The World Stress Map based on the database release 2008. (`www.world-stress-map.org`).

Hermont, A. J., 1979, Letter to the Editor, re: Seismic controllable directional reception as practiced in the U.S.S.R.: Geophysics, **44**, 1601–1602.

Hill, N. R., 1990, Gaussian beam migration: Geophysics, **55**, 1416–1428.

Hooke, R., 1678, Potentia restitutiva, or spring, *in* Classics of Elastic Wave Theory, 2007: Oxford,

Society of Exploration Geophysicists.

Hubral, P., M. Tygel, and J. Schleicher, 1996, Seismic image waves: Geophysical Journal International, **125**, 431–442.

Iversen, E., 2006, Velocity rays for heterogeneous anisotropic media: Theory and implementation: Geophysics, **71**, T117–T127.

Jager, R., J. Mann, G. Hocht, and P. Hubral, 2001, Common-reflection-surface stack: Image and attributes: Geophysics, **66**, 97–109.

Jenner, E., 2008, Recognizing apparent P-wave azimuthal velocity anisotropy caused by lateral velocity variations: The 13^{th} Annual International Workshop on Seismic Anisotropy, 71–72.

Jones, I. F., 2010, An Introduction to: Velocity Model Building: EAGE Publications.

Kazinnik, R., and W. Burnett, 2010, Multifold parameters by predictive painting and without scanning: Expanded Abstracts 80^{th} SEG International Convention, 3639–3644.

Keydar, S., 2004, Homeomorphic imaging using path integrals: Expanded Abstracts 66^{th} EAGE International Conference, P078.

Landa, E., 2004, Imaging without a velocity model using path-summation approach: 74th Ann. Internat. Mtg., Soc. of Expl. Geophys., 1818–1821.

———, 2009, Beyond Conventional Seismic Imaging: EAGE.

Landa, E., S. Fomel, and T. J. Moser, 2006, Path-integral seismic imaging: Geophysical Prospecting, **54**, 491–503.

Larner, K., and C. Beasley, 1987, Cascaded migrations - Improving the accuracy of finite-difference migration: Geophysics, **52**, 618–643. (Errata in GEO-52-8-1165).

Levin, F. K., 1985, Apparent velocity from dipping interface reflections: Geophysics, **50**, 2026–2032.

Levy, S., and D. W. Oldenburg, 1987, Automatic phase correction of common-midpoint stacked

data: Geophysics, **52**, 51–59.

Lewallen, K. T., G. Chen, X. Wu, R. Zhou, and P. Todd, 2008, Seismic characterization of fractured tight gas reservoirs, Piceance Basin, Colorado: Expanded Abstracts 78^{th} SEG International Convention, 463–467.

Liu, F., 1999, Surface Multiple Attenuation Operators in the Plane Wave Domain: Theory and Applications: PhD thesis, The University of Texas at Austin.

Liu, Y., S. Fomel, and G. Liu, 2010, Nonlinear structure-enhancing filtering using plane-wave prediction: Geophysical Prospecting, **58**, 415–427.

Lomask, J., A. Guitton, S. Fomel, J. Claerbout, and A. Valenciano, 2006, Flattening without picking: Geophysics, **71**, P12–P20.

Lomax, A., 1999, Path-summation waveforms: Geophysical Journal International, **138**, 702–716.

Lynn, W., 2007, Uncertainty implications in azimuthal velocity analysis: Expanded Abstracts 77^{th} SEG International Convention, 84–88.

Manning, T., N. Shane, C. Page, B. Bartley, W. Rietveld, and J. Keggin, 2007, Quantifying and increasing the value of multi-azimuth seismic: The Leading Edge, **26**, 510–520.

Mikulich, W., and D. Hale, 1992, Steep-dip v(z) imaging from an ensemble of Stolt-like migrations: Geophysics, **57**, 51–59.

Muir, F., and J. Dellinger, 1985, A practical anisotropic system, *in* SEP-44: Stanford Exploration Project, 55–58.

Neidell, N. S., and M. T. Taner, 1971, Semblance and other coherency measures for multichannel data: Geophysics, **36**, 482–497.

Novais, A., J. Costa, and J. Schleicher, 2006, Velocity determination by image-wave remigration: Expanded Abstracts 68^{th} EAGE International Conference, P157–1–4.

———, 2008, GPR velocity determination by image-wave remigration: Journal of Applied Geophysics, **65**, 65–72.

Ottolini, R., 1983a, Signal/noise separation in dip space, *in* SEP-37: Stanford Exploration Project, 143–150.

———, 1983b, Velocity independent seismic imaging, *in* SEP-37: Stanford Exploration Project, 59–68.

Pranter, M. J., A. I. Ellison, R. D. Cole, and P. E. Patterson, 2007, Analysis and modeling of intermediate-scale reservoir heterogeneity based on a fluvial point-bar outcrop analog, Williams Fork Formation, Piceance Basin, Colorado: AAPG Bulletin, **91**, 1025–1051.

Riabinkin, L. A., 1957, Fundamentals of resolving power of controlled directional reception (CDR) of seismic waves, *in* L. Lu, Slant-stack processing, 1991: Society of Exploration Geophysicists, 36–60.

Rieber, F., 1936, A new reflection system with controlled directional sensitivity: Geophysics, **01**, 97–106.

Rothman, D. H., S. A. Levin, and F. Rocca, 1985, Residual migration - Applications and limitations: Geophysics, **50**, 110–126.

Sava, P. C., B. Biondi, and J. Etgen, 2005, Wave-equation migration velocity analysis by focusing diffractions and reflections: Geophysics, **70**, U19–U27.

Schapper, S., R. Jefferson, A. Calvert, and M. Williams, 2009, Anisotropic velocities and offset vector tile prestack-migration processing of the Durham Ranch 3D, Northwest Colorado: The Leading Edge, 1352–1361.

Schleicher, J., and R. Alexio, 2007, Time and depth remigration in elliptically anisotropic media using image-wave propagation: Geophysics, **72**, S1–S9.

Schleicher, J., J. Costa, and A. Novais, 2008a, Time-migration velocity analysis by image-wave propagation of common-image gathers: Geophysics, **73**, VE161–VE171.

Schleicher, J., and J. C. Costa, 2009, Migration velocity analysis by double path-integral migration: Geophysics, **74**, WCA225–WCA231.

Schleicher, J., A. Novais, and J. Costa, 2008b, Vertical image waves in elliptically inhomogeneous media: Studia Geophysica et Geodaetica, **52**, 101–122.

Schlottmann, R. B., 1999, A path integral formulation of acoustic wave propagation: Geophysical Journal International, **137**, 353–363.

Sen, M. K., and L. N. Frazer, 1991, Multifold phase space path integral synthetic seismograms: Geophysical Journal International, **104**, 479–487.

Sherwood, J. W. C., K. Sherwood, H. Tieman, and K. Schleicher, 2008, 3D beam prestack depth migration with examples from around the world: Expanded Abstracts 78^{th} SEG International Convention.

Sicking, C., S. Nelan, and W. McLain, 2007a, 3D azimuthal imaging: Expanded Abstracts 77^{th} SEG International Convention, 2364–2367.

Sicking, C., G. Treadgold, B. Weinman, A. Berroteran, G. Hoover, and C. Salazar, 2007b, Fracture prospecting with 3D azimuthal imaging: Expanded Abstracts 77^{th} SEG International Convention, 1447–1450.

Siliqi, R., D. L. Meur, F. Gamar, L. Smith, J. Toure, and P. Herrmann, 2003, High-density moveout parameter fields V and Eta, Part 1: Simultaneous automatic picking: 73rd Ann. Internat. Mtg., Soc. of Expl. Geophys., 2088–2091.

Slotnick, M. M., 1936, On seismic computations with applications I: Geophysics, **01**, 9–22.

Stein, M. L., S. M. Ulam, and M. B. Wells, 1964, A visual display of some properties of the distri-

bution of primes: The American Mathematical Monthly, **71**, 516–520.

Stein, S., and M. Wysession, 2003, An Introduction to Seismology, Earthquakes, and Earth Structure: Blackwell Publishing.

Stoffa, P. L., P. Buhl, J. B. Diebold, and F. Wenzel, 1981, Direct mapping of seismic data to the domain of intercept time and ray parameter - A plane-wave decomposition: Geophysics, **46**, 255–267.

Stokes, G. G., 1845, On the theories of the internal friction of fluids in motion, and of the equilibrium and motion of elastic solids, *in* Classics of Elastic Wave Theory, 2007: Society of Exploration Geophysicists.

Sublette, V., C. Sicking, and G. Treadgold, 2008, Estimating HTI in the presence of strong VTI: Expanded Abstracts 78^{th} SEG International Convention, 3033–3037.

Sun, Y., F. Qin, S. Checkles, and J. P. Leveille, 2000, A beam approach to Kirchhoff depth imaging: The Leading Edge, **19**, 1168–1173.

Sword, C. H., 1981, Controlled directional receptivity – A Russian method of pre-stack migration, *in* SEP-26: Stanford Exploration Project, 289–296.

Taner, M. T., and F. Koehler, 1969, Velocity spectra - Digital computer derivation and applications of velocity functions: Geophysics, **34**, 859–881. (Errata in GEO-36-4-0787).

Taner, T., S. Treitel, and M. Al-Chalabi, 2005, A new travel time estimation method for horizontal strata: Expanded Abstracts 75^{th} SEG International Convention, 2273–2277.

Taner, T., S. Treitel, M. Al-Chalabi, and S. Fomel, 2007, An offset dependent NMO velocity model: Expanded Abstracts 78^{th} EAGE International Conference, P036.

Thomsen, L., 1986, Weak elastic anisotropy: Geophysics, **51**, 1954–1966. (Discussion in GEO-53-04-0558-0560 with reply by author).

Tsvankin, I., 1997, Reflection moveout and parameter estimation for horizontal transverse isotropy: Geophysics, **62**, 614–629.

———, 2005, Seismic Signatures and Analysis of Reflection Data in Anisotropic Media: Elsevier.

Tsvankin, I., and A. Al-Dajani, 1998, Nonhyperbolic reflection moveout for horizontal transverse isotropy: Geophysics, **63**, 1738–1753.

van der Baan, M., and S. Fomel, 2009, Nonstationary phase estimation using regularized local kurtosis maximization: Geophysics, **74**, A75–A80.

Vasconcelos, I., and I. Tsvankin, 2006, Non-hyperbolic moveout inversion of wide-azimuth P-wave data for orthorhombic media: Geophysical Prospecting, **54**, 535–552.

Červený, V., 2001, Seismic Ray Theory: Cambridge University Press.

Vermeer, G. J. O., 1999, Fundamentals of 3-D Seismic Survey Design: PhD thesis, Delft University of Technology.

Wang, X., and I. Tsvankin, 2008, Interval anisotropic parameter estimation using velocity-independent layer stripping: Presented at the 13^{th} International Workshop on Seismic Anisotropy Abstracts.

Weisstein, E. W., 2003, CRC Concise Encyclopedia of Mathematics 2^{nd} Edition: Chapman & Hall/CRC.

———, 2009, "Quadratic Curve" from MathWorld–A Wolfram Web Resource. (http://mathworld.wolfram.com/QuadraticCurve.html).

Wiggins, R., 1978, Minimum entropy deconvolution: Geoexploration, **16**, 21–25.

Williams, M., and E. Jenner, 2002, Interpreting seismic data in the presence of azimuthal anisotropy; or azimuthal anisotropy in the presence of the seismic interpretation: The Leading Edge, **21**, 771–774.

Wolf, K., D. A. Rosales, A. Guitton, and J. Claerbout, 2004, Robust moveout without velocity picking: 74th Ann. Internat. Mtg., Soc. of Expl. Geophys., 2423–2426.

Yilmaz, O., 2001, Seismic Data Analysis: Society of Exploration Geophysics.

Yilmaz, O., and M. T. Taner, 1994, Discrete plane-wave decomposition by least-mean-square-error method: Geophysics, **59**, 973–982.

Yilmaz, O., I. Tanir, and C. Gregory, 2001, A unified 3-D seismic workflow: Geophysics, **66**, 1699–1713.

Vita

William Burnett was born in Denver, Colorado. He graduated from Douglas County High School in Castle Rock, Colorado in 2001, and went on to complete the degree of Bachelor of Science in Geophysical Engineering from the Colorado School of Mines in 2005. He started graduate studies in 2005 at The University of Texas at Austin, where he completed the degree of Master of Geological Sciences in Geophysics in 2007. Later in the same year, he continued at UT Austin to pursue the degree of Doctor of Philosophy in Geophysics.

Permanent email address: burnettw@mail.utexas.edu

This dissertation was typeset with LaTeX† by the author.

†LaTeX is a document preparation system developed by Leslie Lamport as a special version of Donald Knuth's TeX Program.